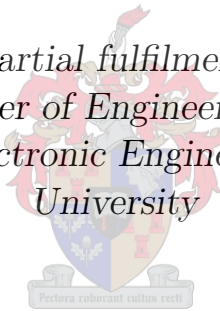


# Design of an Ironless Double-Rotor Radial Flux Permanent Magnet Machine

by

Gert Immelman Oosthuizen

*Thesis presented in partial fulfilment of the requirements  
for the degree of Master of Engineering in the Department  
of Electrical and Electronic Engineering at Stellenbosch  
University*



Department of Electrical and Electronic Engineering, University of Stellenbosch, Private  
Bag X1, Matieland, 7602.

Supervisor: Dr. Peter Jan Randewijk

March 2016





# Declaration

By submitting this thesis electronically, I declare that the entirety of the work contained therein is my own, original work, that I am the sole author thereof (save to the extent explicitly otherwise stated), that reproduction and publication thereof by Stellenbosch University will not infringe any third party rights and that I have not previously in its entirety or in part submitted it for obtaining any qualification.

Date: ..... March 2016 .....

# Abstract

## Design of an Ironless Double-Rotor Radial Flux Permanent Magnet Machine

G.I. Oosthuizen

*Department of Electrical and Electronic Engineering, University of Stellenbosch,  
Private Bag X1, Matieland, 7602.*

Thesis:

November 2015

This thesis presents research on the Ironless Double-rotor Radial Flux Permanent Magnet (IDRFPM) machine. The machine is characterised by a rotor topology consisting of magnets with no iron yoke, which aims to reduce weight and improve overall torque density. Tangentially magnetized inter-pole magnets complete the flux path as would normally be done by the steel yoke. The design also features air-cored concentrated windings which eliminate core losses and cogging torque while reducing copper losses.

The research was preceded by initial work which produced a crude but functional aluminium prototype. A primary focus is to improve the topology used in the first prototype and construct a new prototype with improved torque density. The new prototype will serve as a propulsion motor for a Shell Eco Marathon (SEM) vehicle, since the lightweight characteristic suits a small vehicle application. However, the IDRFPM design is derived from steel-yoke machines used in wind power generation applications. As such, this research aims to gain insights to later be applied to wind technology, particularly for applications in vertical axis wind turbines (VAWTs).

Electromagnetic, structural and thermal analysis was performed as part of a multi-physics design approach. The electromagnetic design concluded that best performance is achieved with an in-line segmented quasi-Halbach magnet array with pole and inter-pole magnets of equal width. To maximize torque density, advanced carbon fibre reinforced plastic (CFRP) was selected to comprise the frame components. Detailed mechanical design was completed and ANSYS Mechanical<sup>®</sup> software was used to assess structural integrity. Thermal analysis was performed to verify the maximum safe operating point. A basic theoretical model was created by approximating the machine as an intricate thermal resistance network. A prototype fit to function as a SEM vehicle propulsion motor was successfully manufactured and tested. While efficiency was slightly lower than anticipated, the machine achieved good torque density. The prototype contains a low percentage structural mass while providing a frame on which a 20" bicycle tire can be directly mounted.

# Uittreksel

## Ontwerp van 'n Ysterlose Dubbel-Rotor Radiale Vloed Permanente Magneet Masjien

*(“Design of an Ironless Double-Rotor Radial Flux Permanent Magnet Machine”)*

G.I. Oosthuizen

*Department of Electrical and Electronic Engineering, University of Stellenbosch,  
Private Bag X1, Matieland, 7602.*

Tesis:

November 2015

Hierdie tesis bevat navorsing oor die Ysterlose Dubbel-rotor Radiale Vloed Permanente Magneet (YDRVPM) masjien. Die masjien word uitgedink deur 'n rotor topologie wat slegs magnete bevat en sonder 'n yster juk, met die doel om gewig te verminder en algemene wringkragdigtheid te verbeter. Tangent gemagnetiseerde tussenpoolmagnete sluit die vloedpad wat normaalweg deur die yster juk gedoen sou word. Die ontwerp bevat ook lugkern gekonsentreerde windings wat kernverliese en rat elimineer en terselfdetyd koperverliese verminder.

Die navorsing is voorafgegaan deur aanvanklike werk wat 'n rof maar funksionele aluminium prototipe ogelewer het. 'n Primêre fokus is om te verbeter op hierdie aanvanklike topologie en om 'n nuwe prototipe te bou met verbeterde wringkragdigtheid. Die nuwe prototipe sal dien as 'n dryfmotor vir 'n Shell Eco Marathon (SEM) voertuig, aangesien die lae gewig eienskappe van die masjien ideaal geskik is vir 'n ligte voertuig toepassing. Die YDRVPM ontwerp is egter 'n verwerking van yster-juk masjiene wat gebruik is in windkragopwekking toepassings. As sulks mik hierdie navorsing om insig te verkry wat later op wind tegnologie toegepas kan word, naamlik toepassings van vertikale as wind turbines (VAWTs).

Elektromagnetiese, struktuur en termiese analise is voltooi as deel van 'n multi-fisika ontwerpbenadering. Die elektromagnetiese ontwerp het aangedui dat 'n inlyn gesegmenteerde kwasi-Halbach magneet opstelling met pool en tussenpool magnete van ekwivalente wydte die meeste wringkrag lewer. Koolvesel versterkte plastiek is gebruik vir strukturele komponente om wringkragdigtheid te verbeter. Gedetailleerde meganiese ontwerp is voltooi en strukturele integriteit is nagesien met gebruik van ANSYS Mechanical<sup>®</sup> sagteware. Die maksimum veilige werkpunt is evalueer deur termiese analise. 'n Basiese termiese model van die masjien is verkry deur die masjien as 'n ingewikkelde netwerk van termiese weerstande te beskou. Vervaardiging van 'n prototipe

geskik om te dien as dryfmotor vir 'n SEM voertuig was suksesvol sowel as toetse op die masjien. Terwyl benuttingsgraad effens laer as berekende waardes was het die masjien goeie wrinkragdigtheid behaal. Die prototipe bevat 'n lae persentasie strukturele massa maar bied tog die nodige raam waarop 'n 20" fietsband direk geplaas kan word.

# Author Publications

Research from this thesis can be viewed, in part, in the following publications by the author:

## International Conference Papers

G.I. Oosthuizen and P.J. Randewijk. Double-rotor ironless radial flux permanent magnet machine. *International Conference on Electrical Machines - ICEM 2014*, pages 496-501, September 2014.

G.I. Oosthuizen and P.J. Randewijk. Design of an Ironless Double-rotor Radial Flux Permanent Magnet Machine. *International Electric Machines and Drives Conference - IEMDC 2015*, May 2015.

## Patent Application

PCT International Patent Application No. PCT/IB2015/053489

G.I. Oosthuizen and P.J. Randewijk Radial Flux Permanent Magnet Machine.

# Acknowledgements

**Father God** - My Creator who gave his son Jesus Christ to show the world what love is.

**Dr. Peter Jan Randewijk** - For giving me the freedom to build and for sharing my enthusiasm.

**P.H. Petzer, A. Swart, H. Koopman & M.H. Jumat** - The electrical workshop staff for sharing their valuable knowledge and helping to make the prototype a success.

**Robert Dobson** - For his kind and patient assistance of a former student.

**Johnathan Smit** - From Launchlab, for his support of our project and many insightful conversations about big ideas.

**Deon & Thea Oosthuizen** - My parents, whose unconditional love and unwavering support carried me through the toughest days.

# Contents

<b>Declaration</b>	<b>i</b>
<b>Abstract</b>	<b>ii</b>
<b>Uittreksel</b>	<b>iii</b>
<b>Contents</b>	<b>vii</b>
<b>List of Figures</b>	<b>x</b>
<b>List of Tables</b>	<b>xii</b>
<b>Nomenclature</b>	<b>xiii</b>
Abbreviations . . . . .	xiii
Constants . . . . .	xiii
Miscellaneous Variables . . . . .	xiii
Electrical Variables . . . . .	xiv
Thermal Variables . . . . .	xv
<b>1 Introduction</b>	<b>2</b>
1.1 Research Background . . . . .	2
1.2 Applications . . . . .	5
1.2.1 Vertical Axis Wind Turbines . . . . .	5
1.2.2 The Shell Eco Marathon . . . . .	7
1.3 Research Objectives . . . . .	9
1.4 Thesis Overview . . . . .	10
<b>2 Key Characteristics</b>	<b>12</b>
2.1 Stator Windings . . . . .	12
2.2 Ironless Rotor Topology . . . . .	13
2.3 Radial vs. Axial Flux . . . . .	14
<b>3 Electromagnetic Design</b>	<b>16</b>
3.1 Baseline Specification . . . . .	16
3.2 Operating Point . . . . .	19

3.3	Design Methodology . . . . .	21
3.3.1	ANSYS Maxwell® Script . . . . .	21
3.3.2	Simulation Approach . . . . .	22
3.4	Magnet Topology . . . . .	22
3.4.1	Segmented quasi-Halbach Array . . . . .	23
3.4.2	Magnet Pitch . . . . .	24
3.4.3	Air Gap . . . . .	26
3.4.4	Number of Poles . . . . .	27
3.5	Topology Comparison . . . . .	28
3.6	Coil Design . . . . .	30
3.6.1	Back-EMF Limit . . . . .	31
3.6.2	Basic Variable Relations . . . . .	32
3.6.3	Coil Losses . . . . .	32
3.7	Final Design Specification . . . . .	35
3.8	Efficiency . . . . .	36
3.9	FEM Benchmark . . . . .	38
<b>4</b>	<b>Structural Design &amp; Manufacturing</b>	<b>40</b>
4.1	Material Selection . . . . .	40
4.1.1	Composites . . . . .	40
4.1.2	Other Alternatives . . . . .	41
4.1.3	CFRP Load Behaviour . . . . .	42
4.2	General Layout . . . . .	42
4.3	Manufacturing Difficulties . . . . .	46
4.4	Revision & Final Prototype . . . . .	49
4.5	Structural Integrity . . . . .	51
4.5.1	Rotor Components . . . . .	51
4.5.2	Stability . . . . .	54
4.5.3	Stator Components . . . . .	55
4.6	Coil Structure . . . . .	56
4.7	Rotor Hub . . . . .	58
4.8	Structure Mass . . . . .	59
<b>5</b>	<b>Thermal Analysis</b>	<b>62</b>
5.1	Heat Dissipation and Cooling Mechanism . . . . .	62
5.2	Thermal Analysis Approach . . . . .	64
5.2.1	Flat Geometry and Symmetry . . . . .	66
5.2.2	Uniform Bodies and Contact Resistance . . . . .	68
5.2.3	Coils . . . . .	69
5.2.4	Internal Forced Convection . . . . .	70
5.2.5	Radiation . . . . .	72
5.3	Analysis and Results . . . . .	73
5.3.1	Static Air Condition . . . . .	73
5.3.2	Forced Convection Condition . . . . .	73



5.4	Torque Density . . . . .	75
<b>6</b>	<b>Testing and Results</b>	<b>78</b>
6.1	Operational Performance . . . . .	78
6.1.1	Test Setup . . . . .	78
6.1.2	OC Test . . . . .	79
6.1.3	Load Test . . . . .	82
6.2	Thermal Performance . . . . .	86
6.2.1	Static Air: No Fan . . . . .	87
6.2.2	Forced Convection: Fan . . . . .	87
6.2.3	Forced Convection: Pressurized Air Supply . . . . .	88
6.2.4	Full Load . . . . .	88
6.3	Structural Performance . . . . .	89
6.3.1	Stator . . . . .	89
6.3.2	Rotor . . . . .	91
6.4	Tested Performance Summary . . . . .	92
<b>7</b>	<b>Conclusions &amp; Recommendations</b>	<b>93</b>
7.1	Electromagnetic Design . . . . .	93
7.1.1	Pole Count . . . . .	94
7.1.2	Coil Turns & Fill Factor . . . . .	94
7.1.3	Coil & Magnet Thickness . . . . .	94
7.1.4	Magnet Grade . . . . .	94
7.2	Design for Manufacture . . . . .	94
7.2.1	Materials and Machining Operations . . . . .	95
7.2.2	Magnet Assembly . . . . .	95
7.3	Thermal Design and Analysis . . . . .	97
7.3.1	Revision of Analysis . . . . .	97
7.3.2	Cooling Strategy . . . . .	97
7.4	Wind Application . . . . .	98
<b>A</b>	<b>Calculation of Inductance</b>	<b>99</b>
<b>B</b>	<b>Lateral Cornering Force</b>	<b>101</b>
<b>C</b>	<b>Thermal Calculations</b>	<b>104</b>
C.1	Initial Calculations . . . . .	104
C.2	Revised Calculations . . . . .	111
<b>D</b>	<b>Assembly Drawing</b>	<b>115</b>

# List of Figures

1.1	A 3-D view of a 16 pole RFAPM machine with non-overlapping windings, Stegmann [24]. . . . .	3
1.2	The first IDRFPM prototype with aluminium rotor. . . . .	3
1.3	Aluminium prototype test measurements. . . . .	4
1.4	Basic types of vertical axis wind turbines[11]. . . . .	6
1.5	Angle of attack and twisting of VAWT blades. . . . .	6
1.6	Shell Eco-marathon Asia 2015. . . . .	7
1.7	The first members of the Stellenbosch University Shell Eco Marathon team. . . . .	8
2.1	Winding configurations[19]. . . . .	12
2.2	RFAPM steel yoke rotor topology. . . . .	13
2.3	IDRFPM ironless rotor topology. . . . .	14
2.4	AFPM machine for a light vehicle application [28]. . . . .	15
3.1	Pac-Car II. . . . .	17
3.2	CAD model of Stellenbosch SEM vehicle. . . . .	17
3.3	AC synchronous machine equivalent circuit. . . . .	19
3.4	Phasor diagram for non-salient PM synchronous machine in constant torque and constant power region ( <i>stator resistance omitted</i> ). . . . .	20
3.5	Torque-speed curve for conventional and IDRFPM machines. . . . .	21
3.6	Topology development. . . . .	23
3.7	Radial flux density vs. normalized radial offset of the tangential magnets. . . . .	24
3.8	Radial flux density and %THD vs. pitch ratio. . . . .	25
3.9	Schematic of coil height ratio $k_c$ . . . . .	26
3.10	%THD vs. coil height ratio. . . . .	27
3.11	Radial flux distribution relative to coil configuration. . . . .	28
3.12	(A)Steel-yoke , (B)Ironless quasi-Halbach and (C)Hybrid topologies. . . . .	29
3.13	Yoke optimization script. . . . .	30
3.14	Phasor diagram of IDRFPM machine. . . . .	31
3.15	Eddy current reduction through laminations [27]. . . . .	34
3.16	Power flow during motor operation. . . . .	36
3.17	Efficiency contour. . . . .	37

3.18	Benchmark of FEM software. . . . .	38
4.1	Exploded views. . . . .	43
4.2	Section views. . . . .	44
4.3	CFRP molds and parts. . . . .	45
4.4	Rim configurations: Spokes (left) vs. full rim (right). . . . .	45
4.5	First completed CFRP parts. . . . .	46
4.6	Forces on magnets in segmented quasi-Halbach array. . . . .	47
4.7	Magnet constraining frames. . . . .	48
4.8	Inner rim magnets with CFRP layer. . . . .	48
4.9	CF deformation during magnet mounting. . . . .	49
4.10	Initial (left) and revised (right) layout. . . . .	50
4.11	Total deformation. . . . .	52
4.12	Deformation in Y direction. . . . .	52
4.13	Stress concentration analysis. . . . .	53
4.14	Ring on rotor mount to relieve stress concentration. . . . .	54
4.15	Rotor shear stress. . . . .	54
4.16	Stator load and deformation. . . . .	56
4.17	Stator stress. . . . .	56
4.18	Mold design for coils. . . . .	57
4.19	Coil mold process. . . . .	57
4.20	Aluminium mounting studs for coils. . . . .	58
4.21	Universal mounting holes on hub. . . . .	59
5.1	Liquid cooling mechanisms. . . . .	63
5.2	Impeller fan concept and prototypes. . . . .	64
5.3	Revised fan concept and prototypes. . . . .	65
5.4	Schematic of heat dissipation in the IDRFPM prototype. . . . .	67
5.5	Simplified thermal diagram. . . . .	68
5.6	Thermal contact resistance [5]. . . . .	69
6.1	Equipment setup for testing. . . . .	79
6.2	Induced voltage measured in OC test. . . . .	80
6.3	Harmonic distortion of induced voltage. . . . .	80
6.4	Results from open circuit test. . . . .	81
6.5	The 1.6 mm coils used to test eddy effects. . . . .	82
6.6	Eddy loss measurements. . . . .	82
6.7	Current(rms) vs. torque measurements. . . . .	83
6.8	Measured efficiency from load test. . . . .	83
6.9	Theoretical efficiency corresponding with measured points. . . . .	84
6.10	Error of measured efficiency: percentage difference. . . . .	85
6.11	Error of measured efficiency: loss power difference. . . . .	85
6.12	Timing belt for the drive motor. . . . .	86
6.13	Relationships of loss to speed and torque. . . . .	86

6.14	Thermal imaging measurement: steady state at $\hat{I}_a=11$ A. . . . .	87
6.15	Fan fixed to prototype. . . . .	88
6.16	Pressurized air supply setup. . . . .	89
6.17	Reinforced stator shaft interface. . . . .	90
6.18	Testing deflection of the stator. . . . .	90
6.19	Testing deflection of the rotor under lateral load. . . . .	91
7.1	Magnets fixed with screws. . . . .	96
B.1	Centripetal force due to cornering. . . . .	101
B.2	Schematic of moment balance for tipping force. . . . .	102

## List of Tables

1.1	Project activities and outcomes. . . . .	10
3.1	Machine design specifications. . . . .	18
3.2	Results of benchmark. . . . .	29
3.3	Eddy losses. . . . .	34
3.4	Final design specifications. . . . .	35
4.1	Mass of various components. . . . .	59
5.1	Calculation results for forced convection case. . . . .	75
5.2	Summary of torque density information. . . . .	76
6.1	Summary of torque density information. . . . .	92

# Nomenclature

## Abbreviations

1-D	One Dimensional
AFPM	Axial Flux Permanent Magnet
CFRP	Carbon Fibre Reinforced Plastic
EMF	Electromotive force
FEM	Finite element method
HAWT	Horizontal Axis Wind Turbine
IDRFPM	Ironless Rouble-rotor Radial Flux Permanent Magnet
OC	Open Circuit (test)
PM	Permanent Magnet
PVUR	Phase Voltage Unbalance Rate
RFPM	Radial Flux Permanent Magnet
RFAPM	Radial Flux Air-cored Permanent Magnet
SEM	Shell Eco-Marathon
THD	Total Harmonic Distortion
VAWT	Vertical Axis Wind Turbine

## Constants

$\pi$	Pi . . . . .	[3.141592654]
$\rho_0$	Resistivity of copper at 20 °C . . . . .	[1.678 × 10 <sup>-8</sup> Ωm]
$\sigma$	Stefann-Boltzman constant . . . . .	[5.67 × 10 <sup>-8</sup> W/m <sup>2</sup> K <sup>4</sup> ]

## Miscellaneous Variables

### Roman Symbols

$A_f$	Frontal area of vehicle . . . . .	[m <sup>2</sup> ]
$C_D$	Drag coefficient . . . . .	[ ]
$C_{rr}$	Rolling resistance coefficient . . . . .	[ ]
$F_D$	Aerodynamic drag force . . . . .	[N]

$F_N$	Normal force . . . . .	[N]
$F_R$	Rolling resistance force . . . . .	[N]
$v$	Linear vehicle velocity . . . . .	[m/s]

**Greek Symbols**

$\rho_{atm}$	Density of atmospheric air . . . . .	[kg/m <sup>3</sup> ]
$\tau$	Torque . . . . .	[Nm]

**Electrical Variables****Roman Symbols**

$\hat{B}_{r1}$	Peak fundamental radial flux density . . . . .	[T]
$E_a$	Peak induced phase voltage (back-EMF) . . . . .	[V]
$h_c$	Coil height . . . . .	[m]
$\hat{I}_a$	Peak phase current . . . . .	[A]
$I_\phi$	RMS phase current . . . . .	[A]
$I_d$	D-axis current . . . . .	[A]
$I_q$	Q-axis current . . . . .	[A]
$k_c$	Coil height ratio . . . . .	[ ]
$k_E$	Machine voltage constant . . . . .	[ ]
$k_m$	Pole pitch ratio . . . . .	[ ]
$k_T$	Machine torque constant . . . . .	[ ]
$k_w$	Winding factor . . . . .	[ ]
$l$	Active/stack length . . . . .	[m]
$L$	Thickness of thermal conductor . . . . .	[m]
$L_s$	Phase inductance . . . . .	[H]
$n$	Shaft/rotor mechanical speed . . . . .	[rpm]
$N$	Turns per coil . . . . .	[ ]
$p$	Number of poles . . . . .	[ ]
$P_{eddy}$	Eddy losses . . . . .	[W]
$P_{cu}$	Copper losses . . . . .	[W]
$P_{loss}$	Total losses . . . . .	[W]
$q$	No. of coils per phase . . . . .	[ ]
$Q$	Total no. of coils . . . . .	[ ]
$V_\phi$	RMS phase voltage . . . . .	[V]
$\hat{V}_a$	Peak terminal phase voltage . . . . .	[V]

$V_{LL}$	RMS line voltage . . . . .	[V]
$r_n$	Nominal radius . . . . .	[m]
$R_a$	Phase resistance . . . . .	[ $\Omega$ ]
$w_m$	Magnet width . . . . .	[m]
$X_s$	Synchronous reactance . . . . .	[ $\Omega$ ]

**Greek Symbols**

$\alpha_{cu}$	Resistive thermal coeff. of copper . . . . .	[ $\Omega/K$ ]
$\gamma_{cu}$	Conductivity of copper . . . . .	[ ]
$\delta_s$	Current penetration from skin effect . . . . .	[ ]
$\eta$	Machine efficiency . . . . .	[ ]
$\mu_r$	Recoil permeability . . . . .	[ ]
$\mu_{cu}$	Permeability of copper . . . . .	[ ]
$\rho_{cu}$	Resistivity of copper . . . . .	[ $\Omega m$ ]
$\tau_m$	Mechanical torque . . . . .	[Nm]
$\omega_e$	Electrical angular velocity . . . . .	[rad/s]
$\omega_m$	Mechanical angular velocity . . . . .	[rad/s]

**Thermal Variables****Roman Symbols**

$A_s$	Exposed thermal surface area . . . . .	[m <sup>2</sup> ]
$Bi$	Biot number . . . . .	[ ]
$c_p$	Specific heat . . . . .	[J/kgK]
$D_h$	Hydraulic diameter . . . . .	[m]
$h$	Heat transfer coefficient . . . . .	[W/mK]
$k$	Thermal conductivity . . . . .	[W/mK]
$L_c$	Characteristic length . . . . .	[m]
$\dot{m}$	Mass flowrate . . . . .	[kg/s]
$Nu$	Nusselt number . . . . .	[ ]
$\dot{Q}$	Heat transfer rate . . . . .	[W]
$R_{cyl}$	Thermal resistance . . . . .	[K/W]
$Re$	Reynolds number . . . . .	[ ]
$T_{air}$	Air temperature . . . . .	[K]
$T_s$	Surface temperature . . . . .	[K]
$V$	Volume of thermal body . . . . .	[m <sup>3</sup> ]

$V_f$  Velocity of fluid . . . . . [m/s]

**Greek Symbols**

$\varepsilon$  Emissivity . . . . . [ ]

$\rho_{air}$  Density of air gap air . . . . . [kg/m<sup>3</sup>]

$\mu_{air}$  Dynamic viscosity of air . . . . . [kg/m<sup>2</sup>s]





# Chapter 1

## Introduction

Industry and academia alike are driven towards the exploration of better ways to use and produce energy. Even the political spectrum is being infiltrated by conversations about a looming energy crisis and the gradual migration away from fossil fuels. An important link in the energy chain is that which links electrical and mechanical power. Electric machines were first developed in the early 19th century, very close to the birth of internal combustion engines. The fundamental principles have not seen much change since, but research continues to find creative solutions to maximize overall utility and effectiveness of these machines. What has drastically changed since the advent of electric machines is the improvement of manufacturing processes and materials available to designers. Most importantly, permanent magnets have become very powerful and relatively affordable, giving rise to widespread use of permanent magnet (PM) machines. This thesis presents research on a fully ironless electric machine, henceforth referred to as the Ironless Double-rotor Radial Flux Permanent Magnet (IDRFPM) machine, which aims to reduce the weight generally associated with electric machinery by doing away with active components made of heavy steel.

### 1.1 Research Background

The IDRFPM design is derived from existing double rotor Radial Flux Air-Cored Permanent Magnet (RFAPM) machine designs for which a reliable analytical model had been developed [18] as a design tool. The design shown in Figure 1.1 is an example of a RFAPM which was built for a small horizontal axis wind generator application by A. Stegmann [24].

An idea was proposed to replace steel yoke components in the RFAPM design with magnets completing the flux path in order to reduce rotor mass. Design of a crude prototype was performed as a final year project by the author and served as a starting point from which this project could continue. This

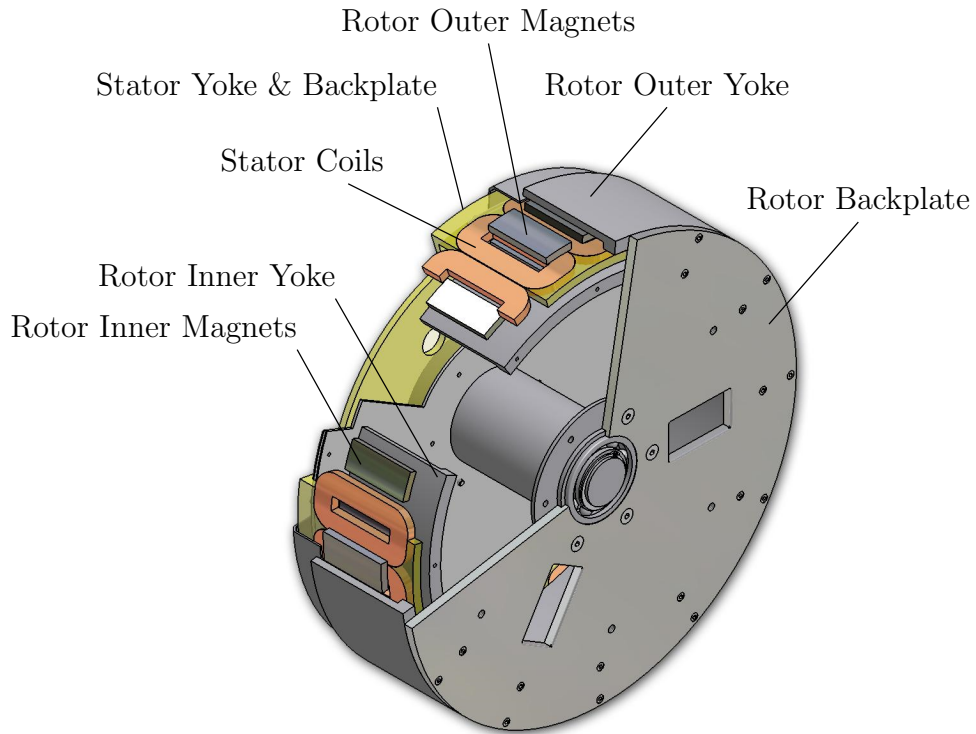


Figure 1.1: A 3-D view of a 16 pole RFAPM machine with non-overlapping windings, Stegmann [24].

prototype, pictured in Figure 1.2, featured aluminium discs stacked to form a cylindrical structure. Each disc featured slots for the to accommodate the offset magnet configuration, cut via waterjet. While the prototype was unable to achieve a net increase in torque density, it served as a proof of concept.

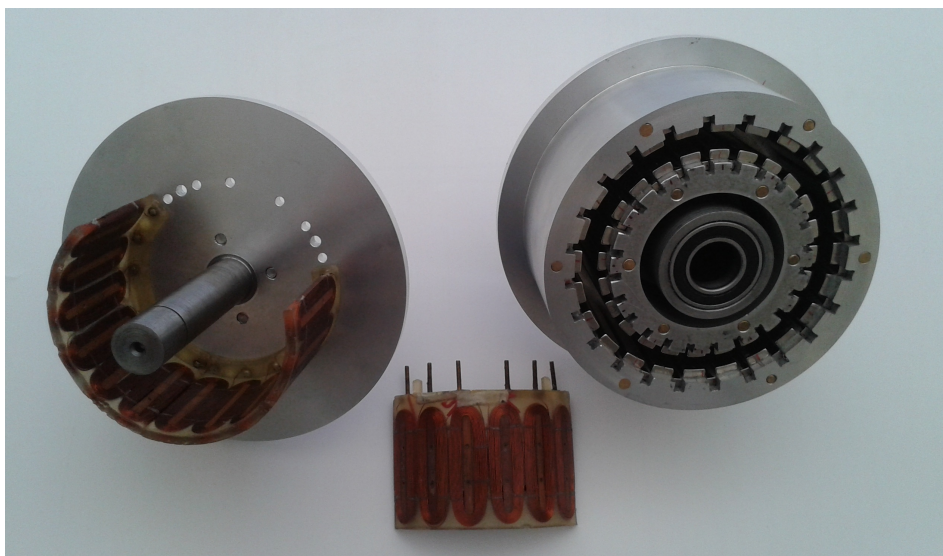


Figure 1.2: The first IDRFPM prototype with aluminium rotor.

Figure 1.3 shows test data taken from that machine. The voltage and current waveforms are sinusoidal and indicate a successful design. Comparison between the theoretical and measured motor constants deduced from Figure 1.3 C and D indicate about 11% deviation from design specification. This sufficed for a crude proof of concept and served as a benchmark for this project to improve upon.

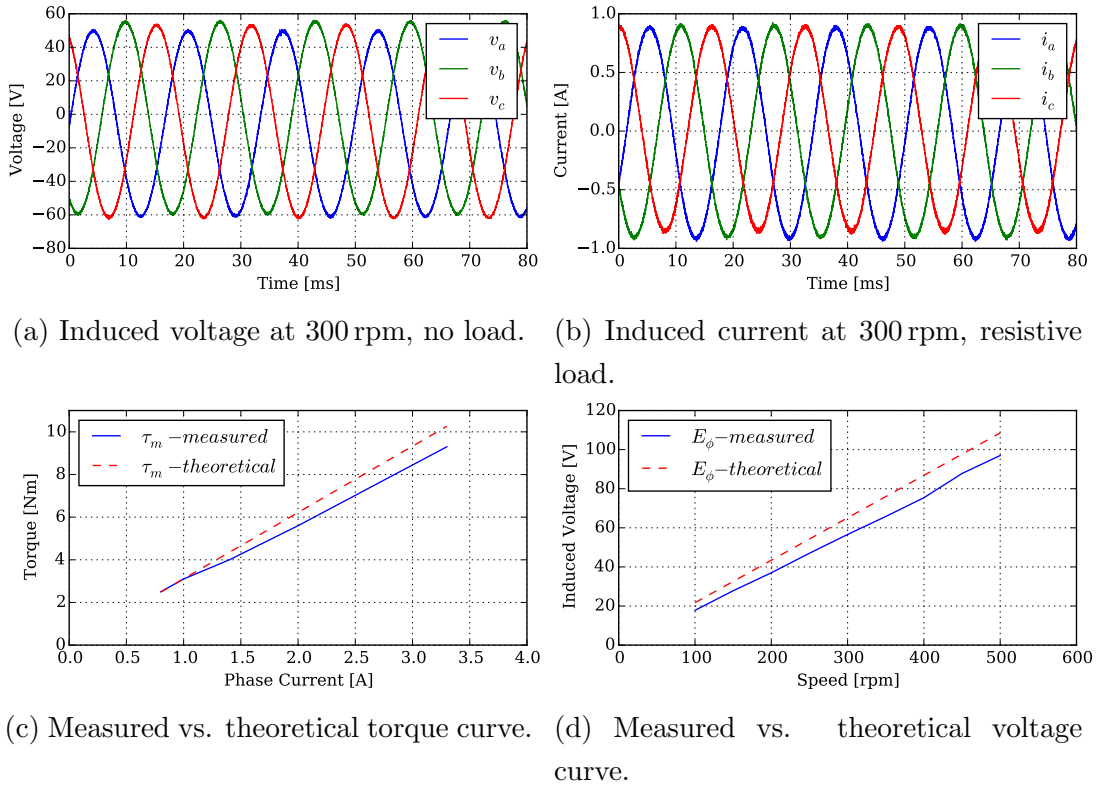


Figure 1.3: Aluminium prototype test measurements.

Test results and design process for the prototype were compiled in a paper which was accepted at ICEM 2014 in Berlin, Germany [16]. The successful result of this prototype also resulted in a sizeable Technology Innovation Agency (TIA) seed fund grant. These funds opened up new possibilities for research on the IDRFPD concept and motivated some of the ambitious design choices that will be discussed in this thesis.

## 1.2 Applications

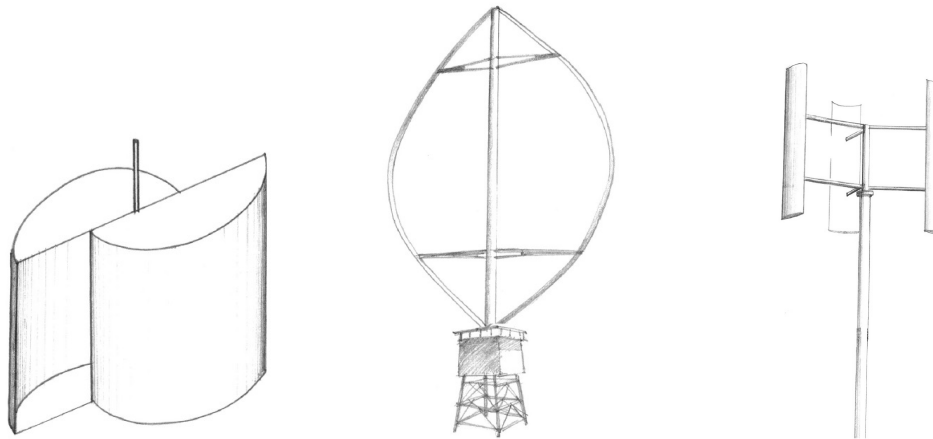
The primary advantage of the IDRFPM over its peers is the prospect of increased torque density. However, the extent of this claim would have to be verified in case studies of potential applications, taking into account the net benefit in terms of both performance and cost. It is thus necessary to choose an application which can benefit from the torque density characteristic of the IDRFPM.

### 1.2.1 Vertical Axis Wind Turbines

The RFAPM design is one of a number of machines that have been tested in horizontal axis wind turbine (HAWT) applications by members of Stellenbosch University's electric machinery research group. While HAWTs dominate the wind power market, vertical axis wind turbines (VAWT) are still considered a viable option for certain applications. VAWTs tout a simpler mechanism than HAWTs in that they do not require yaw capability to face the wind direction. The generator and gearbox components can also be mounted at the base of the structure, which is beneficial for large turbines which otherwise, as in the case of HAWTs, would be difficult to maintain and repair[14].

There are two basic types of VAWTs: Savonius and Darrieus. Savonius turbines, depicted in Figure 1.4a, are the simplest and have good starting torque but are generally the least efficient. Darrieus turbines are lift force driven and consist of aerofoil shaped blades. They offer higher efficiency but suffer from low starting torque. Early commercial applications utilized either the curved blade "egg beater" shaped or straight blade turbines shown in Figures 1.4b and c.

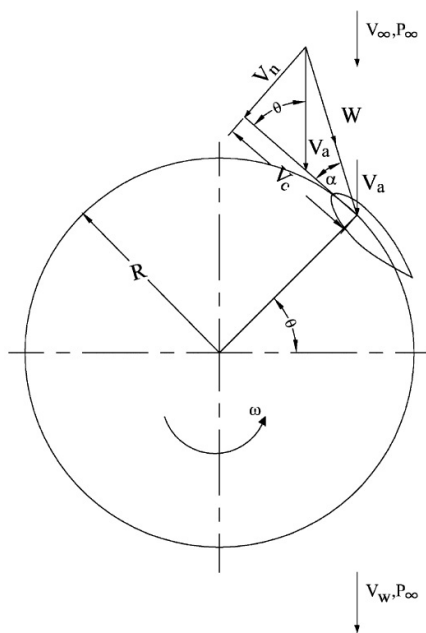
A niche for VAWTs exists in small low-power urban applications. Wind traversing the urban landscape of skyscrapers and hot parking lots is often turbulent and irregular, posing a challenge to HAWTs which must rotate on an axis perpendicular to the wind direction. This suits the VAWT configuration which can utilize wind entering at any angle. Still, for a vertical blade there will be an ideal angle of attack, or direction from which the wind must blow to achieve highest torque production, as indicated by  $\alpha$  in Figure 1.5a. A commonly incorporated solution to this problem is to use helically twisted blades such that for any wind direction, there is some point on at least one



(a) Savonius type turbine. (b) Curved blade Darrieus type turbine. (c) Straight blade Darrieus type turbine.

Figure 1.4: Basic types of vertical axis wind turbines[11].

blade that is experiencing an ideal angle of attack. Figure 1.5b shows such a turbine.



(a) Angle of attack vertical blades[14].

(b) Helically twisted blades.

Figure 1.5: Angle of attack and twisting of VAWT blades.

Despite advances in blade technology, low starting torque is still a serious drawback of using VAWTs which is not impossible to overcome but requires

complex aerofoil shape and drag design[4]. The IDRFPM could potentially aid this endeavour by reducing inertia of the system with a lighter rotor and doing away with cogging torque.

### 1.2.2 The Shell Eco Marathon

While the IDRFPM design has its roots in wind power generation, its potential as a weight-saving technology is obvious for propulsion applications. From the onset of work on the IDRFPM in 2013, mention had been made of the Shell Eco Marathon (SEM) and the desire for an entry into the competition by Stellenbosch University. SEM is a competition held in Europe, Asia and America annually which invites academic institutions to construct a vehicle which must traverse a specified distance on track within a specified time limit.

Figure 1.6 shows vehicles competing in the 2015 Asian race held in Manila, Philippines. These vehicles may use any of a number of fuel types including different grades of petrol, hydrogen or simply an electric battery. A winner is declared for each fuel category as well as an overall winner for the vehicle which completes the track while using the least amount of energy.



Figure 1.6: Shell Eco-marathon Asia 2015.

Pursuing this application would offer a relatively high-profile platform for which to develop and showcase the IDRFPM technology. A successful motor could both give the Stellenbosch team a competitive edge and motivate further TIA funding to continue research. The decision was made to construct a prototype motor for a small vehicle to be entered into the European SEM competition. Much could be learned from constructing the motor prototype



which could be applied directly to any future wind turbine prototypes. Also, the motor would ultimately be tested as a generator, potentially offering insight into its viability as a generator for VAWTs.

At the beginning of 2014, a team was formed consisting of a number of final year engineering students in addition to the author, a masters student contributing the motor. The mechanical engineering students were responsible for designing a chassis and fairing as well as a test rig which would simulate the track conditions while keeping the car stationary. The electrical and electronic engineering students were responsible for designing drive electronics and a battery management system, which were considered a part of the work being funded in part by TIA. Collaboration between the team members established design specifications for the motor which will be discussed in greater detail in Section 3.1. The team is pictured in Figure 1.7 with the chassis, its IDRFPM prototype and fairing in the background.



Figure 1.7: The first members of the Stellenbosch University Shell Eco Marathon team.



## 1.3 Research Objectives

In the simplest terms, the goal of this project is to produce a new and improved IDRFBM prototype. In doing so, the project will seek to improve torque density and reduce discrepancy between the theoretical designed and final achieved motor constant. A very important component of the prototype objective is shedding light on any manufacturing techniques or difficulties associated with the topology to guide the manufacture of future prototypes.

Given that practical implementation and prototyping are the primary focus, it was deemed beyond project scope to reassess the analytical approximation of radial flux density for the IDRFBM, instead using FEM simulation software to guide the electromagnetic design process as will be discussed in Chapter 3. By the same reasoning, full optimization was also deemed beyond the immediate scope of the project. However, a central goal of the project is to assess the interdependence of various design variables pertaining to electromagnetic design as well as any relevant mechanical considerations.

Since the application for the prototype was chosen to be a propulsion motor for a vehicle, another objective of the project is to create a functional prototype which will fulfil this function. This implies that structural analysis be performed to ensure the machine will support a worst-case load scenario during operation of the vehicle. However, as far as functionality is concerned the project does not aim to produce any of the drive electronics or control components to facilitate operation of the motor, which will be developed concurrently as part of separate projects.

Along with electromagnetic and structural mechanical design and analysis, the project wishes to incorporate thermal analysis to establish a thorough multi-physics design approach. Thermal analysis is important for any electrical machine because its rated performance is determined in by the maximum power it can safely sustain without its components reaching critical temperatures and consequently experiencing failure. As with the structural design, thermal analysis will serve as a safety net to determine whether the design proposed by the electromagnetic design will be safe in real-world operating conditions.

Once manufacture of the prototype is complete, it must be tested. Extensive tests will be performed to determine motor constants and efficiency. Basic tests will be performed to determine if overall structural and thermal

performance objectives have been reached. The primary project goals are summarized in Table 1.1. As an overarching secondary objective, this research aims to provide a detailed record of the full design and manufacture process for an IDRFPM prototype using innovative materials. This record, in turn, should serve as a guide for the design of future IDRFPM prototypes.

Table 1.1: Project activities and outcomes.

<b>Activities</b>	<b>Outcomes</b>
Electromagnetic design	-Improve performance and torque density from first prototype.
Mechanical design & manufacture	-Complete mechanical design of fully functional propulsion motor for SEM Vehicle. -Execute manufacture and assembly of prototype.
Structural analysis	-Identify critical structural weaknesses under critical load condition.
Thermal analysis	-Assess performance at critical temperature. -Assess potential heat dissipation strategy for machine.
Testing	-Compare test and theoretical data to assess success of design.

## 1.4 Thesis Overview

### Chapter 1: Introduction

Background information about the project is discussed, explaining the origins of the IDRFPM design and the work that preceded this text. A few applications are also considered and a number of research objectives identified.

### Chapter 2: Key Characteristics

A number of features make the IDRFPM a unique machine. These features are discussed in greater detail to give a thorough understanding of the principles that guide the design and analysis process documented in the rest of the text.

**Chapter 3: Electromagnetic design**

The IDRFBPM topology is heavily revised to improve performance. This chapter documents the changes made and determines expected performance figures of the final design.

**Chapter 4: Structural Design & Manufacturing**

This chapter presents the development of the layout and structural design of the frame components of the IDRFBPM prototype. Structural integrity of the design is assessed for a worst-case load condition and critical stress areas are identified. The manufacture process is also documented, noting various difficulties that came about.

**Chapter 5: Thermal Performance**

An analytical analysis is performed of the thermal characteristics of the machine to determine safe operating points under load. A thermal strategy is suggested and its effect on performance is assessed.

**Chapter 6: Testing & Results**

The IDRFBPM prototype is tested to determine whether or not the design was successful.

**Chapter 7: Conclusions & Recommendations**

An overview of observed outcomes is given. A number of recommendations are made for future design and manufacture endeavours.

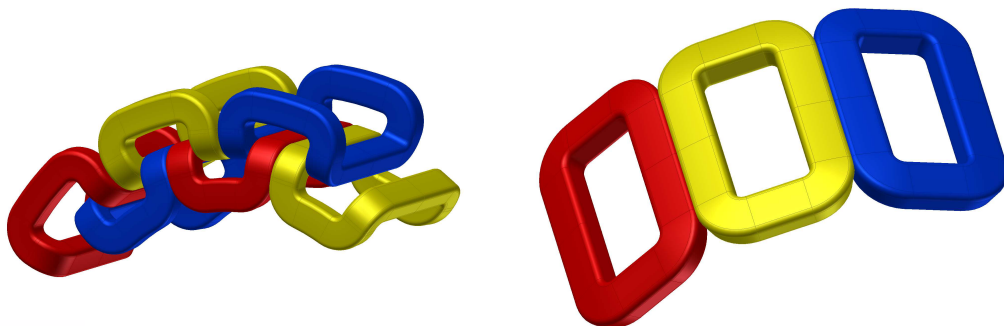
# Chapter 2

## Key Characteristics

A few key characteristics of the IDRFPM topology distinguish the machine as a desirable option for the propulsion motor application. These underlying principles essentially motivate the research presented in this text, and is important to discuss them before delving into the detailed design process.

### 2.1 Stator Windings

An important feature inherited from machines that precede the IDRFPM is its air-cored, non-overlapping stator windings. Both of these characteristics contribute significantly to efficiency. The air-cores imply that iron/core losses in the stator are eliminated. Core losses include hysteresis losses and eddy losses that would arise from transient flux densities in the iron cores. Meanwhile, the non-overlapping concentrated coils dramatically reduce end turn length compared to overlapping windings, as depicted in Figure 2.1, hence reducing  $I^2R$  losses.



(a) Overlapping coils.

(b) Non-overlapping concentrated coils .

Figure 2.1: Winding configurations[19].

This configuration was also proven to provide higher torque factor for small diameter machines with short stack or active length relative to diameter[19], which corresponds with the prototype discussed in this text.

The air-cored characteristic also eliminates cogging torque, which is the primary source of torque ripple generally experienced by iron-cored machines and occurs because of the attraction between stator iron slots and the rotor field. With cogging torque eliminated, starting torque is dramatically reduced, which is beneficial for wind power applications. A small vehicle application also benefits from zero cogging torque since the effect would otherwise have to be smoothed out by the power electronic drive system in order for the vehicle to coast more freely.

## 2.2 Ironless Rotor Topology

The most prominent characteristic of this design, and also its namesake, is its totally ironless rotor, which together with the air-cored stator windings implies a totally ironless design. The diagrams in Figures 2.2 and 2.3 illustrate the steel yoke and ironless topologies.

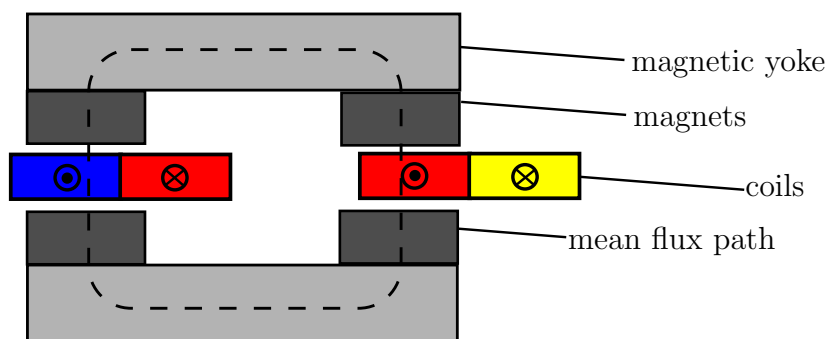


Figure 2.2: RFAPM steel yoke rotor topology.

The ironless topology replaces the steel magnetic yoke with interpole magnets which are oriented in the tangential direction to complete the flux path, indicated by the dotted lines. Figure 2.3 schematically represents the initial topology, which placed the tangential interpole magnets on the same radius that was previously occupied by steel, offset from the radius of the pole magnets. Previous work which produced the aluminium prototype concluded that this arrangement resulted in approximately 20% less torque than its steel yoke counterpart. This 20% figure represents the benchmark upon which the new

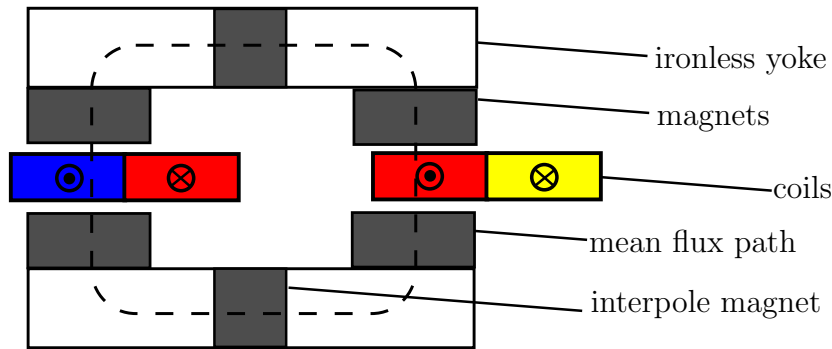


Figure 2.3: IDRFPM ironless rotor topology.

prototype had to improve. The changes brought to the design are discussed in Chapter 3.

## 2.3 Radial vs. Axial Flux

Ironless designs have come about in recent years, but most studies have focused on axial flux permanent magnet (AFPM) machines [29, 2]. In [2], an ironless axial flux machine was compared to a steel-yoke RFPM machine and named increased torque density along with the elimination of eddy losses as primary advantages. Another comparison between radial and axial flux steel-yoke machines found that the radial flux was superior because yoke thickness was constrained by electromagnetic saturation rather than mechanical strength, benefiting from the inherent structural rigidity of a cylinder and allowing less active mass [25]. The IDRFPM machine aims to benefit both from the structural integrity of a radial flux design and the efficiency of an ironless machine.

Furthermore, it has also been noted that the ratio between diameter and axial length is basically fixed for AFPMs while RFPMs can be optimized to suit the application [3]. Predecessors of the IDRFPM designed for wind power generation were also radial flux machines, further motivating the choice to design a radial flux prototype. However, the prototype that will be built for this research will still be compared with AFPMs commonly used in similar applications, such as the machine in Figure 2.4 designed for a light vehicle application[28].

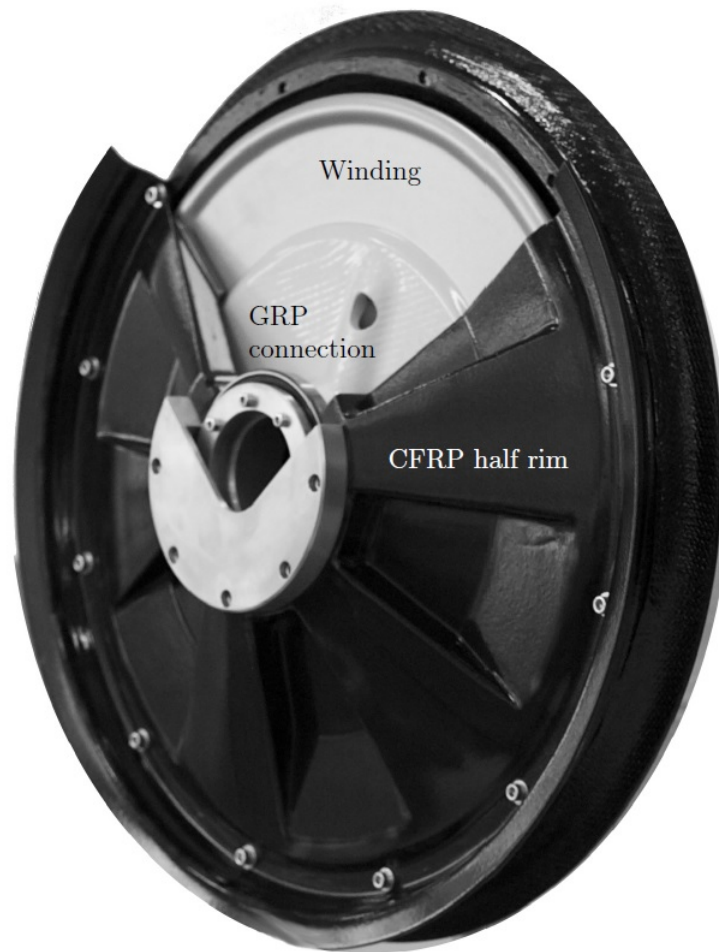


Figure 2.4: AFPM machine for a light vehicle application [28].

# Chapter 3

## Electromagnetic Design

This chapter will discuss the design process that formed the magnet topology and coil specifications for the prototype. It will also establish a number of performance parameters that also influence the mechanical design as well as theoretical efficiency. The results from this chapter will eventually be compared with test results from the finished prototype.

### 3.1 Baseline Specification

The starting point for the design process is the parameters implicated by the prototype's application as a propulsion motor for a SEM vehicle. SEM regulations stipulate a 48 V overall maximum system voltage. This limits the battery voltage and, in turn, the back-EMF voltage, which has drastic implications for the coil design that will be discussed later in this chapter.

During a collaborative design session with the mechanical students responsible for the chassis and fairing design, a standard 20" bicycle wheel was chosen as the size for the driving wheel. A maximum cruising speed of 27 km/h was derived from distance and time requirements for the SEM race. Given the wheel diameter, the design rotational speed was rounded up to 290 rpm. Preliminary sketches were drawn to determine the amount of space available in the axial direction of the machine and the space required for end turns and structural supports. From these sketches an active or stack length of 40 mm was chosen.

The required torque output is based on aerodynamic drag force, rolling resistance from the tires and slope of the track. The Stellenbosch SEM team used a publication of the Pac Car II [22], the most efficient vehicle to ever compete in the competition, to aid the vehicle design process. Pac Car II is pictured in Figure 3.1.





Figure 3.1: Pac-Car II.

The Pac Car II publication noted the following formula with which to calculate aerodynamic drag acting on a body moving through air,

$$F_D = \frac{1}{2} \cdot \rho_{atm} \cdot v^2 \cdot C_D \cdot A_f \quad (3.1)$$

where  $F_D$  is linear drag force,  $\rho_{atm}$  is the density of atmospheric air,  $v$  is linear velocity,  $C_D$  is the drag coefficient and  $A_f$  is frontal area of the body. Pac Car II had a frontal area of a mere  $0.3 \text{ m}^2$ , a drag coefficient of 0.1 and assumed an air density of  $1.2 \text{ kg/m}^3$ . The Stellenbosch SEM vehicle, pictured in Figure 3.2, features a frontal area of  $0.35 \text{ m}^2$  and a theoretically calculated drag coefficient of  $C_D = 0.11$ .



Figure 3.2: CAD model of Stellenbosch SEM vehicle.

At the cruising speed of 27kph or 7.5 m/s, this results in 1.3 N of drag force. Frictional rolling resistance is equated as follows

$$F_R = C_{rr} \cdot F_N \quad (3.2)$$

with the rolling resistance coefficient  $C_{rr}$  and normal force  $F_N$ . The Pac Car II publication noted a rolling resistance coefficient of approximately 0.002 for the Michelin tires used by competition vehicles[22] and 0.006 for standard bicycle tires. The true rolling resistance of the wheels used on the Stellenbosch SEM vehicle were experimentally determined to be 0.0065 [6]. Vehicle mass, including chassis, fairing, motor, electrical components and driver, was estimated to be 85 kg. With this vehicle mass and assuming the coefficient of a regular bicycle tyre, rolling resistance is 5.06 N. The combined forces at cruising velocity of 6.36 N translate into 1.6 Nm of torque for a 20" bicycle wheel.

Since the team planned on attending the 2015 European SEM competition in Rotterdam where the track would be almost completely flat, the torque specification was pegged at 10 Nm. However, during the year an invitation was received to a new South African SEM competition which was to be held at Kyalami race track near Johannesburg. This track features inclines which posed a potential problem and forced a revision of the torque requirement. Track elevation data was analysed by a member of the Stellenbosch SEM team and noted a maximum elevation of 6°[20]. Given the 85 kg vehicle mass, 22 Nm would be required to overcome gravitational force at this incline. Adding rolling resistance and drag gives 23.6 Nm. Maximum torque requirement was increased to 30 Nm to ensure the vehicle would be able to overcome unforeseen obstacles. The baseline specifications for electromagnetic design are summarized in Table 3.1.

Table 3.1: Machine design specifications.

<b>Peak voltage</b>	48 V	<b>Nominal speed</b>	290 rpm
<b>Nominal torque</b>	10 Nm	<b>Max. torque</b>	30 Nm
<b>Active length</b>	40mm	<b>Max. diameter</b>	500mm

## 3.2 Operating Point

The designer must determine at which operating speeds maximum torque is required and whether or not lower torque is acceptable at higher speeds. If this is the case, field weakening can be implemented to operate at a speed that would otherwise result in a back-EMF exceeding the applied inverter voltage. The technique has seen wider use thanks to the growing popularity of PM synchronous machines and the increasing efficiency they offer [13]. This is an appealing prospect for a machine meant to propel a SEM vehicle with a competition regulation of 48V maximum system voltage and a low cruising torque requirement. However, the ironless design is characterized by very small synchronous reactance. This unfortunately impedes its field weakening capability.

To understand why, one must consider the equivalent circuit and phasor diagram for a synchronous machine in Figures 3.3 and 3.4. The magnet field lies in the positive d-axis direction while back-EMF lies in the positive q-axis. Being a non-salient machine, the IDRFPM will achieve maximum torque output when the current phasor is aligned with the q-axis. By introducing a negative d-axis current, the inductance voltage drop becomes  $180^\circ$  out of phase with the back-EMF, allowing speed to increase without exceeding inverter voltage.

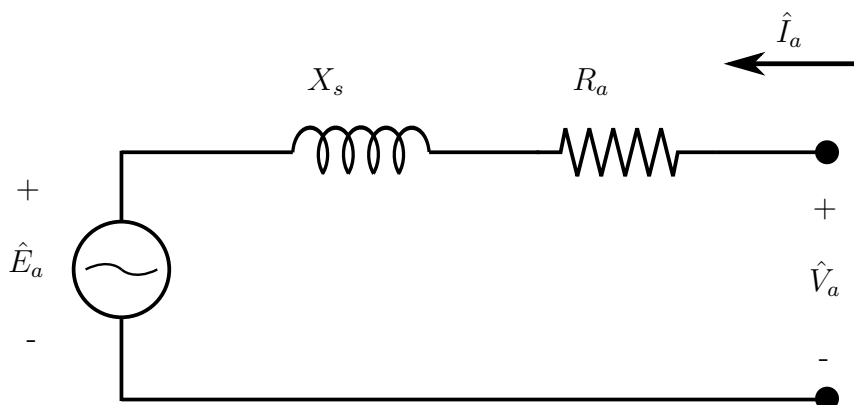


Figure 3.3: AC synchronous machine equivalent circuit.

In Appendix A, inductance for the final design specification was calculated to be  $95 \mu\text{H}$ . With the synchronous reactance equal to  $j\omega L_s I_d$  and such a

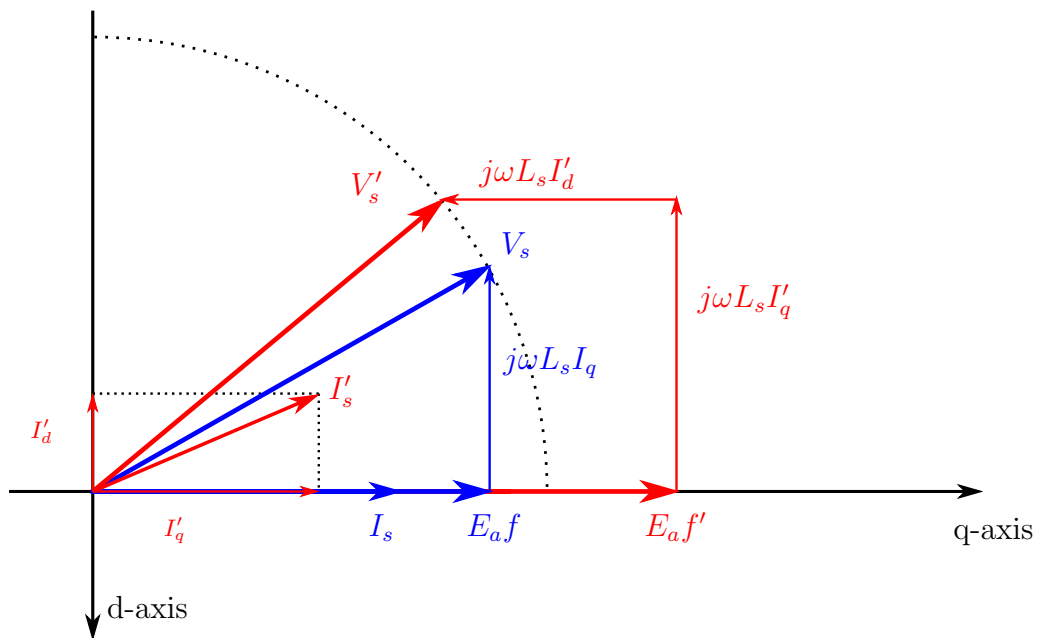


Figure 3.4: Phasor diagram for non-salient PM synchronous machine in constant torque and constant power region (*stator resistance omitted*).

low inductance values, an extremely large d-axis current would be required to weaken the field, which will result in a very small q-axis current for torque production. The large d-axis current thus translates into a large  $I_s^2 R_a$  loss making no contribution to torque, which defeats the purpose of creating an efficient machine. This means that an operating point in the constant power speed range is not a practical option for the IDRFPM.

Figure 3.5 roughly illustrates behaviour in the constant power speed range of the IDRFPM compared to a typical synchronous machine. It could have been helpful to design for a cruising velocity at point B so that the vehicle can cruise at higher velocities with low torque but still be able to produce the desired maximum torque at lower speeds. Instead the machine must be designed such that it can accommodate the desired maximum cruising velocity and maximum torque at point A, the rated operating point of the machine.

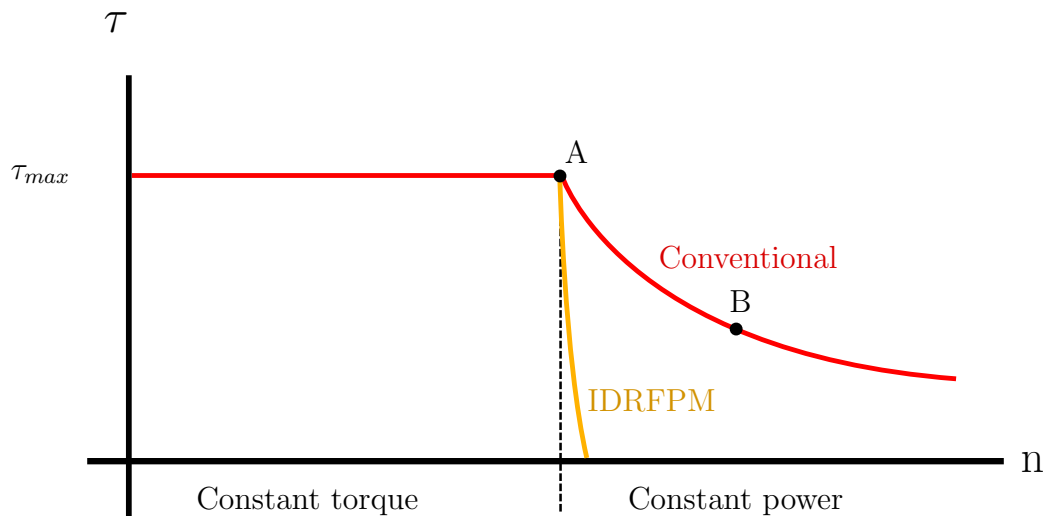


Figure 3.5: Torque-speed curve for conventional and IDRFPM machines.

### 3.3 Design Methodology

In any design situation, reliable analytical approximations are the ideal tool. Unfortunately, such approximations aren't always available to electric machine designers who must then resort to FEM software analysis. As mentioned in the introductory chapter, previous work on iron-yoke DRFAPM machines [17] produced a reliable analytical approximation for radial flux density in the air gap, but revision of the approximation for IDRFPM machines was not included in this project scope. A so called “one dimensional” (1-D) approximation of radial flux [16] attempted to fill this void. The approximation had been used successfully for steel yoke machines assuming high recoil permeability  $\mu_r$  for the iron portion of the machine and a short air gap so that fringing effects were negligible. Unfortunately the gaps between magnets in the offset magnet configuration for the initial IDRFPM design would result in more prominent fringing effects, and the 1-D approximation failed to match radial flux values calculated by FEM.

#### 3.3.1 ANSYS Maxwell<sup>®</sup> Script

The simulations were created using ANSYS Maxwell<sup>®</sup> software controlled by a Python script. While the software does offer machine templates for many standard electric machines, no such template exists for the double rotor PM

topology. Instead of drawing the machine manually, the script is used to calculate coordinates of points that draw the magnets and coils. The script used for this project was originally developed for research on steel yoke DRFAPM machines [18] and was modified to simulate the IDRFPM design.

### 3.3.2 Simulation Approach

Fortunately, 2D FEM simulations for the IDRFPM topology are simple enough that radial flux density can be approximated quickly and reliably. The original script created transient solutions to solve for torque and torque ripple. However, magnetostatic solutions are much faster and can still calculate the radial flux characteristics necessary to perform basic design. The script was changed to include an the option of performing a full transient solution or performing a magnetostatic solution that does not include the coils.

Magnetostatic solutions could then be performed in scripted loops to determine relationships between design variables, as documented in Section 3.4. Throughout this process, radial flux density is calculated for each design change. If radial flux density is known, the torque or voltage constant can be equated from a variation of the standard synchronous machine equation as

$$k_T = k_E = 2qr_n l N k_w \hat{B}_{r1} \quad (3.3)$$

with  $q$ ,  $r_n$ ,  $l$ ,  $N$  and  $k_w$  being number of coils per phase, nominal radius, active length, turns per coil and a winding factor respectively.  $\hat{B}_{r1}$  is the peak value of the fundamental component of the radial flux density distribution along the nominal radius which runs exactly halfway between the inner and outer magnets along the middle of the coils, instead of the centre of the air gap as in machines with a single air gap. Once radial flux characteristics for an ideal design were established, more time consuming transient solutions could be performed including the coils. Further parameters discussed in Section 3.6 could then be tweaked to achieve the desired performance characteristics.

## 3.4 Magnet Topology

A critical development made by this research is the revision of the magnet topology from the configuration discussed in Chapter 2. This section discusses

the major developments in magnet layout which resulted in the final rotor design specification.

### 3.4.1 Segmented quasi-Halbach Array

The ironless concept in its infancy aimed to mimic the flux path in steel-yoke machines by placing tangentially magnetized magnets where the steel yoke had previously been, as shown in Figure 3.6a.

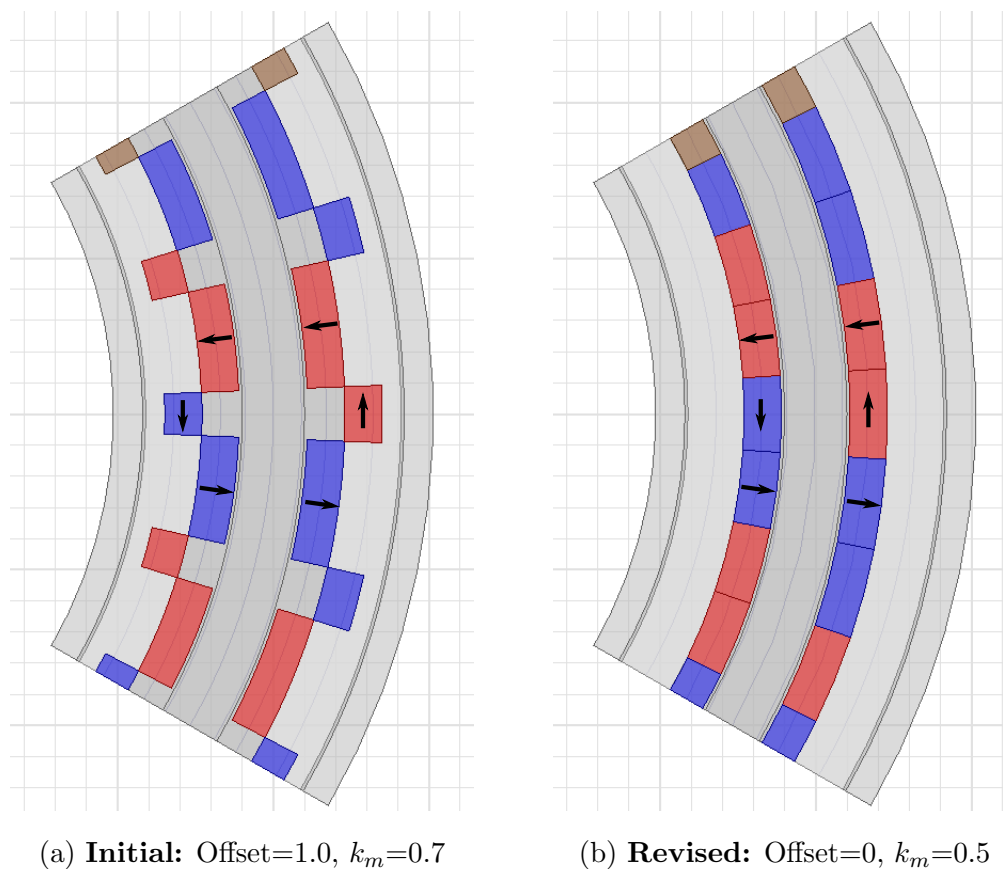


Figure 3.6: Topology development.

This idea was abandoned for the new prototype as it was suspected that the offset position of the tangential magnets was not the most effective arrangement. A set of FEM results incremented the tangential magnet offset and confirmed that the highest flux density is achieved with zero offset, or essentially a segmented quasi-Halbach arrangement. The trend is shown in Figure 3.7, where the offset value is the ratio of offset distance to thickness

of the pole magnet. Unity offset is displayed in Figure 3.6a and zero offset in 3.6b.

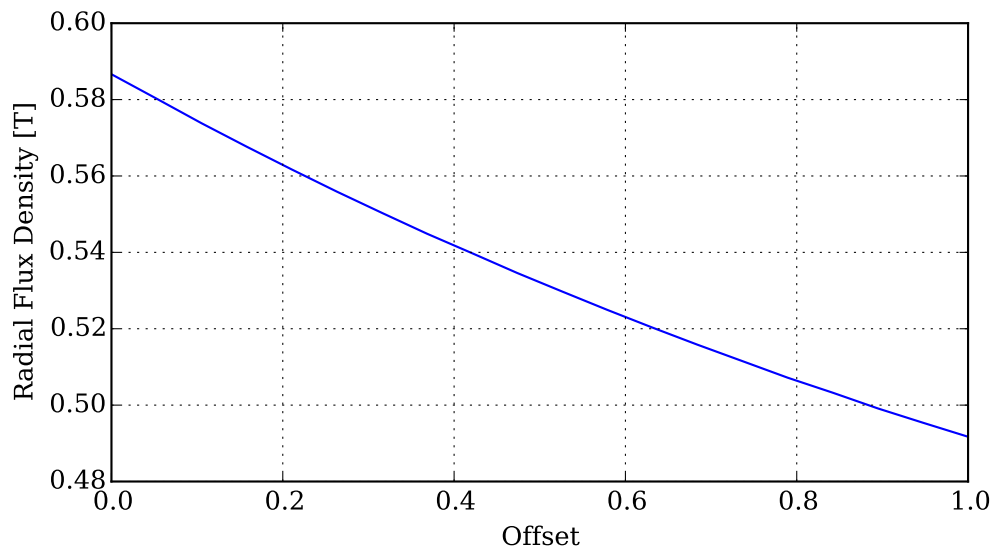


Figure 3.7: Radial flux density vs. normalized radial offset of the tangential magnets.

The concept of a segmented quasi-Halbach array has been around for some time, first described in the late 1970s by Klaus Halbach [8]. Halbach noted that when magnets were arranged in sequentially rotating magnet orientations, a focused or augmented field occurred on one side of the array while the field reduced on the other side. This phenomenon presents obvious benefits in various applications, but in particular for electric machinery where augmented magnetic fields will translate into higher torque. As such, Halbach arrays appear in various electric machinery applications in the literature [31].

### 3.4.2 Magnet Pitch

In addition to maximizing air gap flux density, the magnet topology must minimize space harmonics present in the air gap radial flux distribution. Simply put, harmonics present in this distribution can cause torque production opposing the desired direction and in turn reduce efficiency. The machine will be operated as a full AC synchronous machine, as opposed to brushless DC machines which are driven by square waveforms. As such the waveforms driving the machine will be sinusoidal, so minimizing the harmonics present in the



magnet field will result in the most effective power transfer. A standard metric for harmonic purity is percent total harmonic distribution (%THD) equated as

$$\%THD_{Br} = \frac{\sqrt{\sum_{h=2}^{\infty} \hat{B}_{r,h}^2}}{\hat{B}_{r,1}} \times 100\% \quad (3.4)$$

The %THD in the radial flux distribution can be controlled by varying magnet width and coil height. For the segmented quasi-Halbach array, the entire pole pitch is occupied by magnet material. A pole pitch ratio,  $k_m$ , was identified in [17] to indicate the ratio between magnet width and total pole pitch. In the IDRFP, this ratio indicates the ratio between pole magnet width and tangential magnet width since the two widths summate to the total pole pitch. For steel-yoke machines, an optimal  $k_m$  value of 0.7 was determined. This value was used for the first IDRFP prototype but also warranted revision. Figure 3.8 plots the peak radial flux density  $\hat{B}_r$ , fundamental component of the radial flux distribution  $\hat{B}_{r|1}$ , and the percentage total harmonic distortion %THD in the radial flux distribution. A pole pitch ratio of 0.5 corresponds with the least %THD.

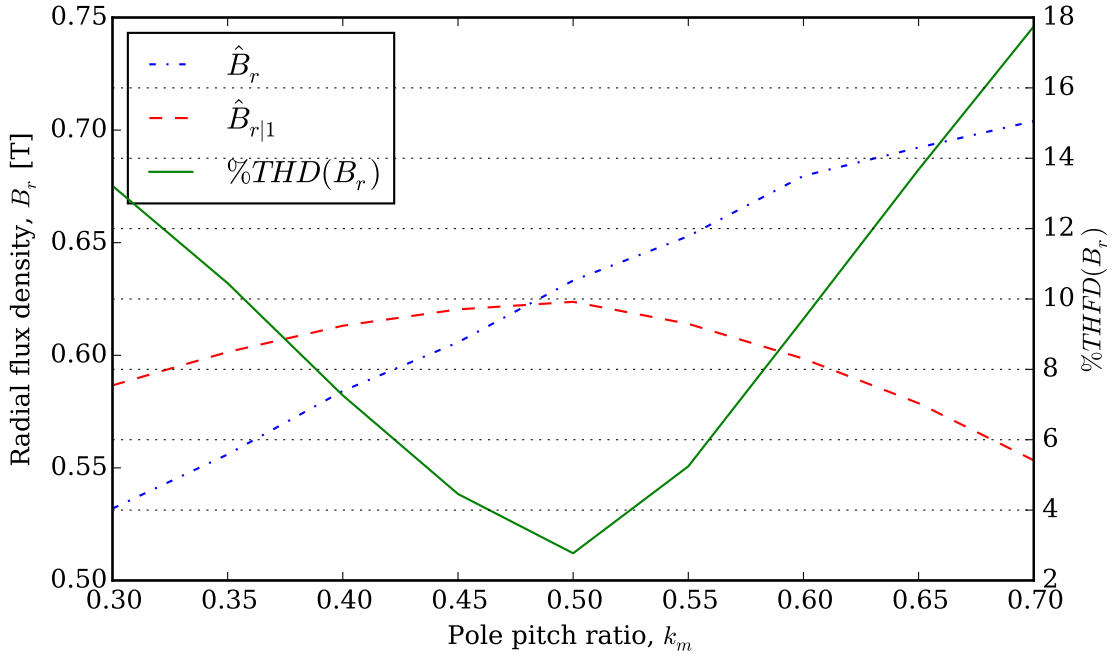


Figure 3.8: Radial flux density and %THD vs. pitch ratio.

### 3.4.3 Air Gap

In the ironless machine, the air gap constitutes the entire space between the inner and outer magnet arrays, even though the coils occupy most of this space with two air gaps<sup>1</sup> on either side. As such, the air gap height must be determined according to coil design considerations which will be discussed in Section 3.6. This portion of the discussion, however, only considers radial flux characteristics.

Even with pole pitch ratio at 0.5, it was found that %THD will be less than optimal if the air gap is too thin relative to the magnet width. With nominal radius and magnet thickness fixed, coil height was varied to determine an optimal value. Figure 3.10 plots %THD versus coil height ratio  $k_c$ . This is defined as the ratio between coil height and magnet width, depicted in Figure 3.9. Magnet width is taken as the average between width of the inner and outer magnet.

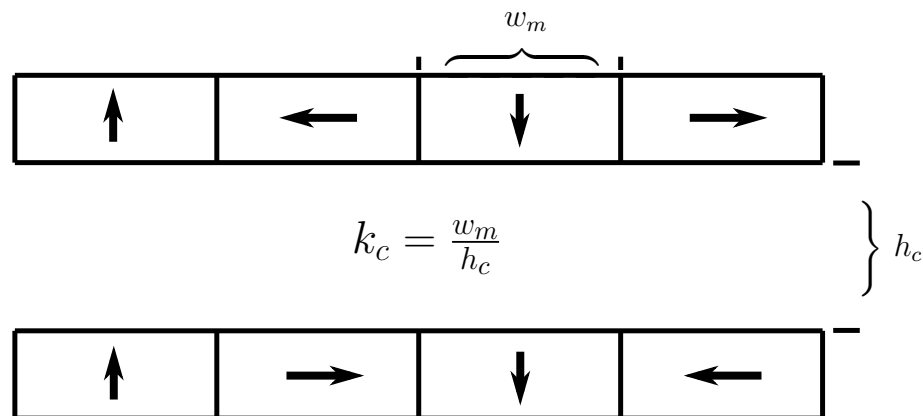


Figure 3.9: Schematic of coil height ratio  $k_c$ .

From Figure 3.10 it can be seen that %THD reduces with coil height ratio down to about 0.9, at which point changes in %THD become erratic. Increasing the air gap reduces the radial flux density while at the same time allowing more space for coils. Ultimately, coil height was adjusted to accommodate

<sup>1</sup>A thickness of 1 mm in each air gap was originally chosen because manufacturing methods for the prototype would struggle to guarantee a thinner gap. The gap was later increased to 1.5 mm to accommodate a CFRP retaining layer discussed in Chapter 4.

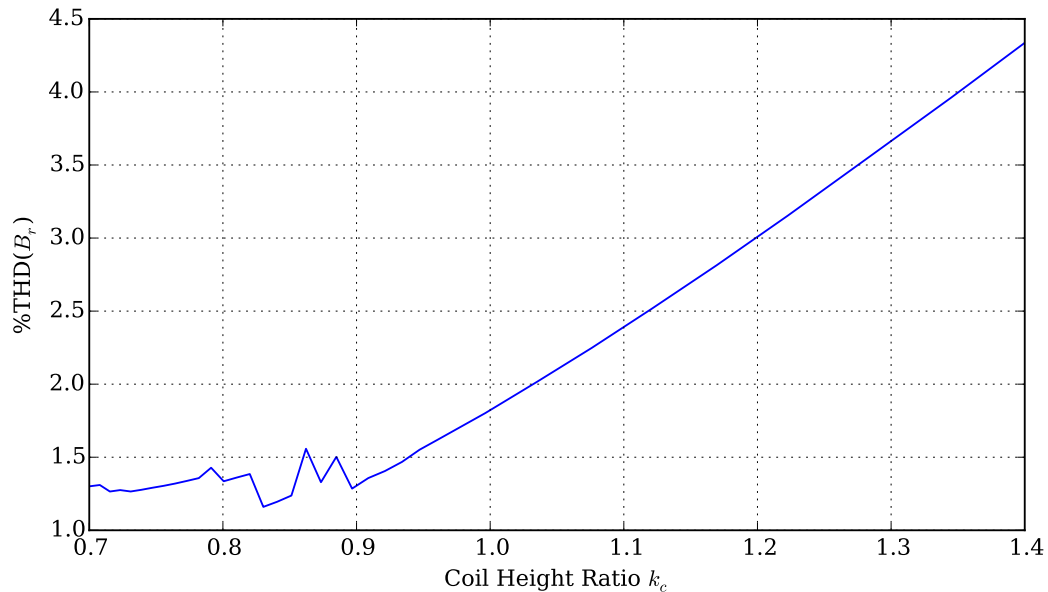


Figure 3.10: %THD vs. coil height ratio.

back-EMF limits and other practical considerations discussed in Section 3.6, resulting in a sufficiently low coil height ratio of approximately 1.5.

#### 3.4.4 Number of Poles

Another important design variable influenced by this relationship was the number of poles. Magnet width is a function of nominal radius and the number of poles which determines total pole pitch.

The machine was initially designed with 24 poles. When it was determined that the torque requirement must increase, nominal radius had to be drastically increased, which increased the magnet width and with it the %THD. The increased harmonic distortion could be remedied either by increasing the coil height or the pole count. Since the coils would have to be very thick to sufficiently reduce %THD, the number of poles was increased to 28. Poles for this machine must be a multiple of four because the coil to pole ratio is 3/4 and coils must be a multiple of three for a three phase machine. This is because the working harmonic of the coils is actually the second harmonic, and thus requires a corresponding radial flux distribution, as depicted in Figure 3.11.

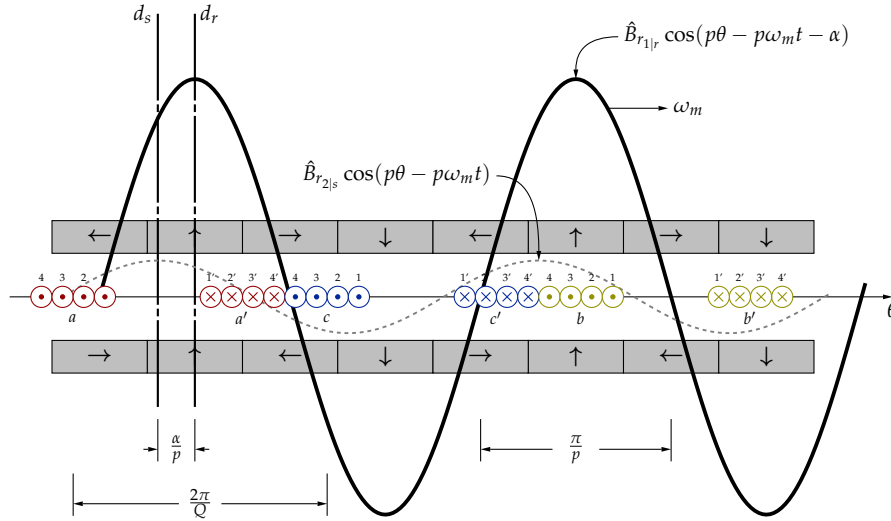


Figure 3.11: Radial flux distribution relative to coil configuration.

### 3.5 Topology Comparison

After the topology was revised, it was suggested that reintroducing a thin steel yoke into the segmented quasi-Halbach topology may be beneficial. This “hybrid” of a Halbach array with steel yoke had to be investigated to ensure that an ironless topology was in fact the most effective. In order to establish the best topology, the steel-yoke, hybrid and ironless topologies, as shown in Figure 3.12, were compared.

For either topology, a machine with a given air gap and given radial flux density would produce the same torque, assuming negligible difference in %THD. In order to ensure a fair comparison, the steel-yoke and hybrid machines would have to contain the optimal balance between steel and magnet material. This was facilitated by a python script which would draw machines starting with a thin magnet thickness, increase the yoke thickness until a “knee point” was reached (<10% torque increase per thickness increment) and then test to see if the radial flux density matched that of a given IDRFP design. If the flux density was still too low, yoke thickness would be reset to a thin value and magnet thickness would be incremented, repeating the process until radial flux density matched the given IDRFP flux density. A flow diagram of the script is shown in Figure 3.13.

Active mass, including the magnets, steel yoke, and copper coils cast in resin was used to calculate torque density. Torque output for the given coil geometry with the given radial flux density is 24 Nm at a peak phase current

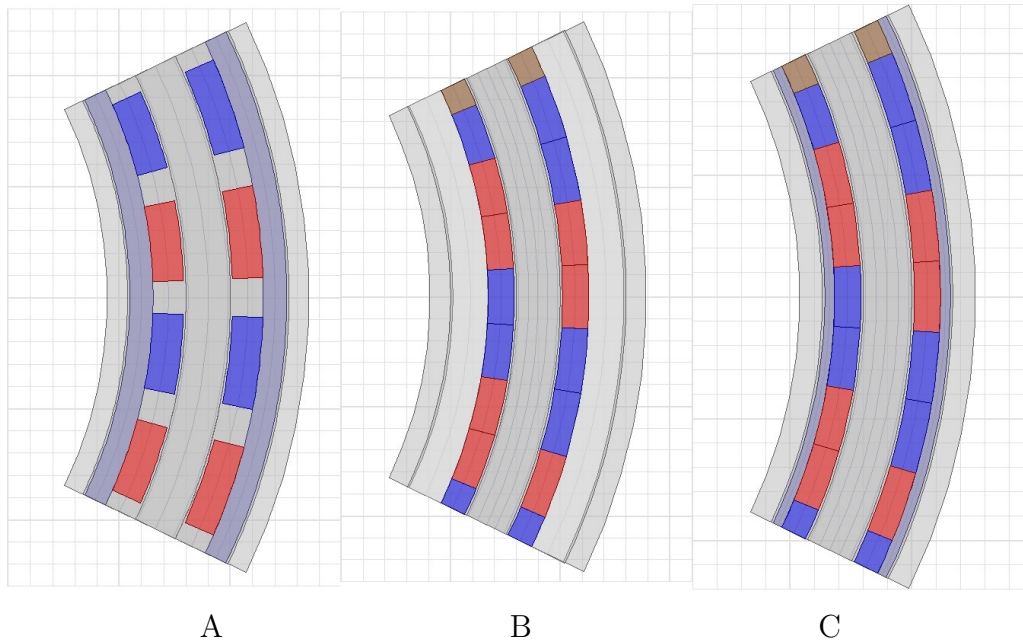


Figure 3.12: (A)Steel-yoke , (B)Ironless quasi-Halbach and (C)Hybrid topologies.

of 17 A with 22 turns per coil. Results are summarized in Table 3.2.

Table 3.2: Results of benchmark.

Topology	Magnet Mass( $kg$ )	Total Active Mass( $kg$ )	Torque Density( $\frac{Nm}{kg}$ )
Steel-yoke	2.19	6.15	3.90
Ironless	2.71	4.22	5.68
Hybrid	2.44	5.24	4.58

The total active mass necessary in the steel-yoke topology shows a clear disadvantage in terms of torque density and outweighs the reduction in magnet mass. The hybrid topology requires 10% less magnet mass than ironless but sacrifices 20% of torque density since total active mass is still higher. Torque density for active mass is highest for the ironless topology and is simpler to construct as no steel yoke with laminations is required. From a broader perspective, the argument could be made that the cost of having more magnet mass could negate the torque benefit for a mass-produced machine, but the author has acknowledged that this machine will likely seek a niche market where cost savings is less important.

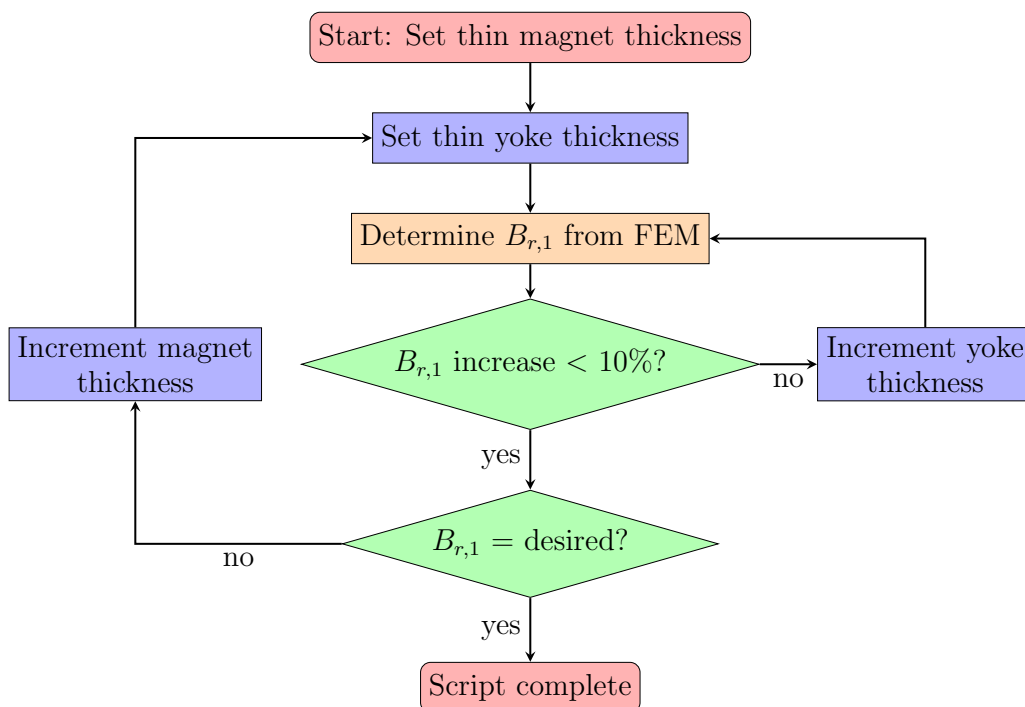


Figure 3.13: Yoke optimization script.

It is important to note that the significance of these torque densities lies in how they compare with each other. Overall torque density depends thermal behaviour of the machine at the corresponding operating point. This will be discussed in greater detail in Chapter 5 where safe operating points of the machine are investigated through thermal analysis.

## 3.6 Coil Design

Throughout this chapter, the magnet topology has been developed to ensure that radial flux density being provided most effectively and with the lowest harmonic distortion. The remaining component of electromagnetic design is the coils. The coils are a crossroads for a number of key design variables and present a considerable challenge of balancing constraints. This section will discuss the relationships between these variables and the way in which design specifications were determined.

### 3.6.1 Back-EMF Limit

In addition to inverter output, maximum back-EMF is also influenced by the way in which the windings are connected: delta or star. In the case of star connection, phase voltage is related to line voltage by

$$V_{LL} = \sqrt{3}V_{\phi} \quad (3.5)$$

which implies that, in the case of the 48 V restriction, the maximum phase voltage that can theoretically be applied is only 27.7 V. Delta connection offers higher phase voltage which is theoretically equal to line voltage but in turn requires higher current, again by a factor of  $\sqrt{3}$ . As part of the IDRFPM and SEM projects, a battery management system is concurrently being developed. Practical considerations for this system dictated that current could not be increased by the necessary factor, so the star connection was chosen. Fortunately, the space-vector-PWM (SPWM) technique used to create the AC phase voltage results in a peak value equal to 1.15 times the applied DC voltage. Taking this effect into account along with an assumed 5% voltage drop across the total equivalent series resistance, phase voltage is equal to 31.8 V. The maximum back-EMF then becomes a function of resistance and inductance along with the current angle for a given operating point, as depicted by the phasor diagram in Figure 3.14.

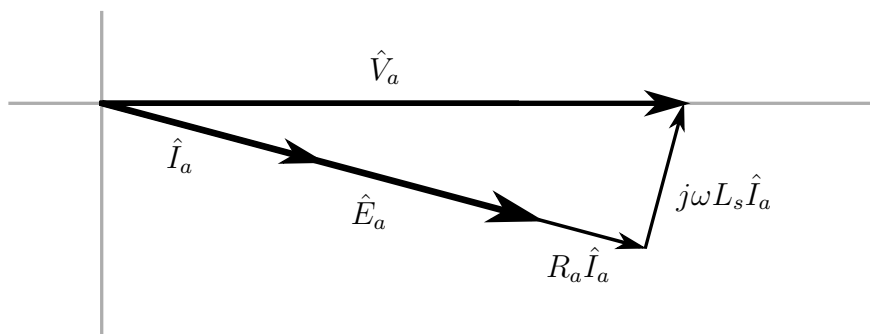


Figure 3.14: Phasor diagram of IDRFPM machine.

### 3.6.2 Basic Variable Relations

From (3.3) it can be seen that the number of coil turns is linearly proportional to the motor constants. It is thus also linearly proportional to back-EMF and torque which are equated as

$$E_a = k_E \omega_m \quad (3.6)$$

where  $\omega_m$  is the mechanical rotational speed of the rotor, and

$$\tau_m = k_T \hat{I}_s \quad (3.7)$$

where  $\hat{I}_s$  is the stator current space vector equated as

$$\hat{I}_s = \frac{3}{2} \hat{I}_a \quad (3.8)$$

where  $\hat{I}_a$  is the peak phase current. Meanwhile, the designer must bear in mind that coil turns are limited by the space available, which is also dependent on wire thickness. Thus, for a given torque requirement, voltage limit, and available coil area, high back-EMF can be overcome by reducing the number of turns and increasing current and wire thickness to maintain torque.

Wire thickness must be as high as possible to reduce RMS current density since high current density can lead to dangerously high temperatures in the machine. This necessitates thermal analysis as discussed in Chapter 5, but for the initial design current density was kept below  $6 \text{ A/mm}^2$  for cruising torque. Higher densities were allowed for peak torques intended only for short durations and not exceeding  $10 \text{ A/mm}^2$ . Choosing wire thickness is further complicated by the uncertainty of fill factor, which is the ratio between cross sectional copper area and total available coil area. It is difficult to know this ratio before physically winding test coils, but it is generally assumed to be about 0.5 and no higher than 0.6.

### 3.6.3 Coil Losses

However, thicker wires present other negative performance characteristics associated with high frequencies of current. A thick section of conductor carrying high frequency current experiences the skin effect, in which the current only penetrates a short distance from the perimeter of the conductor section and is not conducted through the centre. Since the current now occupies a smaller



area, current density effectively increases and with the resistance of the conductor. Depth of this penetration can be approximated by

$$\delta_s = \frac{1}{\sqrt{\pi f \mu_{cu} \gamma_{cu}}} \quad (3.9)$$

with frequency  $f$ , and copper permeability  $\mu_{cu}$  and conductivity  $\gamma_{cu}$ . For the range of frequencies and conductor diameters in question, skin depth was found to be far greater than conductor radius and thus a negligible effect. An effect which generally has a much greater influence is eddy losses. Generally, eddy losses only occur in iron cores of electric machines since flux is directed through these components such that minimal flux leakage cuts the coils. The ironless design employs air-cored coils which have no iron cores. This means that flux fields cut only the copper and can produce eddy loss in thick conductors. To estimate eddy losses, the following equation taken from [12] was used:

$$P_{eddy} = N Q a \left( \frac{\pi l d^4 \hat{B}_{r1r}^2 \omega_e^2}{64 \rho_{cu}} \right) \quad (3.10)$$

where  $Q$ ,  $d$ ,  $a$ ,  $\omega_e$ , and  $\rho_{cu}$  are the number of coils, wire diameter, number of parallel strands<sup>2</sup>, electrical field rotation speed in rad/s and the resistivity of copper, respectively. From (3.10) it is clear that increasing wire thickness dramatically increases eddy losses. The coils designed using the aforementioned constraints used 1.6 mm thick wires. A quick check for eddy losses indicated negligible losses due to the low rotational speed. Unfortunately, the negligible loss was calculated by mistakenly using mechanical frequency instead of electrical frequency, which are related as follows:

$$\omega_e = \frac{p}{2} \omega_m \quad (3.11)$$

The only solution for high eddy losses is thin parallel strands, or Litz wire. Stranded wires segment the conductive area and in this way provide much less area for eddy currents to form. The mechanism for eddy loss is also employed in iron cores and yokes which use steel laminations, as depicted in Figure 3.15<sup>3</sup>. Stranded wires unfortunately reduce fill factor, due to the added insulation material between each strand and also due to the twisting of the wires.

<sup>2</sup>The term normally refers to phase windings connected in parallel. In this case, where Litz wire will be incorporated and coils for each phase are connected in series, it refers to the number of conductors present in a multi-stranded wire.

<sup>3</sup>It should be noted that this figure illustrates the concept of eddy loss reduction by segmentation of a body, while the direction of flux relative to orientation of copper segments will be different in the IDRFP.

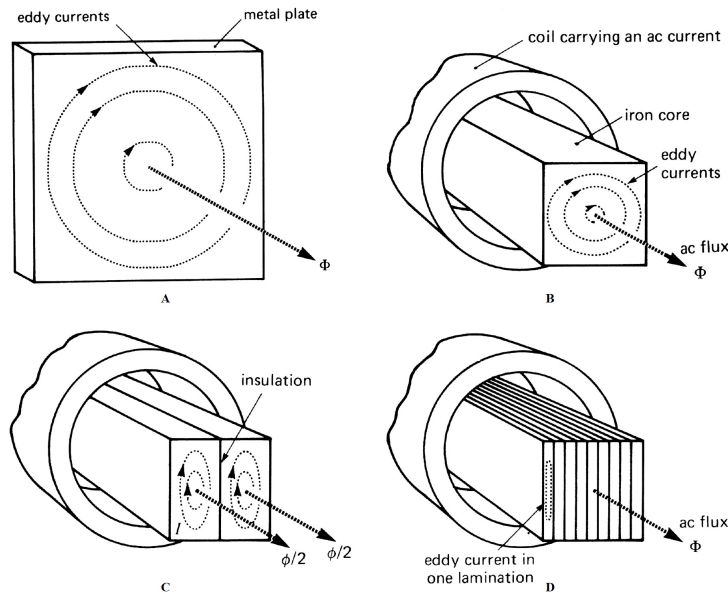


Figure 3.15: Eddy current reduction through laminations [27].

Table 3.3 gives the eddy losses for 1.6 mm and two alternatives, calculated using (3.10) at cruising speed of 300 rpm with 22 turns and peak fundamental radial flux density of 0.631 T. These results indicate that the reduction in eddy loss is enough to justify the reduction in fill factor.

Table 3.3: Eddy losses.

Coil Specification	Eddy Loss (W)
1 × 1.6 mm	27.28
11 × 0.5 mm	2.86
70 × 0.2 mm	0.47

All coil sets had already been made with 1.6 mm wire before impact of eddy losses was identified, but the significant losses left no choice but to re-cast the coils with stranded wire. The only readily available litz wire contained 70 strands of 0.2 mm thick wire. The reduced fill factor allowed only 19 turns to be fit versus 22 with the 1.6 mm round wire. While this represents a 14% torque reduction, it gives nearly 98% eddy loss reduction based on theoretical calculation. An equation taken from [25] instead of (3.10) was originally used, but was later determined by A. Joss to be incorrect. Initial estimates indicated

even higher losses than those shown in Table 3.3. Had the equation been verified, Litz wire with fewer strands may have been used. A comparison of practical test results from both sets of coils will be presented in Chapter 6.

The conductors in Litz wire are twisted or woven to distribute the length of each conductor which is exposed to the high current densities along the outer radius of a wire carrying high frequency alternating current. This ensures that conductors on the inner portions of the wire contribute to wire conductivity. The IDRFPM does not greatly benefit from this feature but does suffer from the reduction in fill factor, which dropped from 0.493 with solid 1.6 mm wire to 0.466 with stranded litz wire.

### 3.7 Final Design Specification

Specifications were established by the reasoning described throughout this chapter, which involved practical considerations. Not only did the number of coil turns change due to a change in wire, but magnet thickness was reduced in order to increase the air gap for mechanical considerations discussed in Chapter 4. Table 3.4 summarizes the final specifications of the IDRFPM as it was constructed.

Table 3.4: Final design specifications.

<b>Peak voltage</b>	48 V	<b>Nominal speed</b>	290 rpm
<b>Max current(rms)</b>	14.14 A	<b>Max current density</b>	6.4 A/mm <sup>2</sup>
<b>Nominal current(rms)</b>	6.65 A	<b>Nominal current density</b>	3.0 A/mm <sup>2</sup>
<b>Max. torque</b>	21 Nm	<b>Nominal torque</b>	10 Nm
<b>Active length</b>	40 mm	<b>Nominal radius</b>	120 mm
<b>Magnet thickness</b>	5.5 mm	<b>Coil height</b>	9mm
<b>Air gap</b>	1.5 mm	<b>Coil turns</b>	19

The maximum torque was reduced from 30 Nm to 21 Nm due to the reduction in magnet thickness and the number of coil turns. The limit is set due to the maximum current the battery system currently being designed will be able to provide. A thermal analysis in Chapter 5 will give a clearer picture of the theoretical maximum the machine could safely sustain.

### 3.8 Efficiency

It is important to assess what was achieved with the electromagnetic design by determining the expected efficiency of the machine. This is normally a very difficult task for electric machines as it is difficult to accurately predict iron losses, which are susceptible to a host of factors such as lamination thickness and material properties. Conversely, the IDRFPM contains no iron and thus will have no iron losses.

An often neglected source of losses is those that occur within the magnets themselves. However, it was shown that rotor iron losses for the DRFAPM topology would be negligible [21]. Given that in a synchronous machine, the fundamental magnetic field is rotating at the same speed as the rotor and thus no alternating flux is present in either the rotor yoke or magnets. A small amount of alternating flux is still possible depending on the control strategy. A FEM analysis of a similar axial flux machine reported very small losses [28]. Thus, losses occurring in the magnets will be considered negligible for this machine. Power flow for the IDRFPM is summarized schematically in Figure 3.16, with the only losses left to be considered being copper losses and coil eddy losses as discussed in the previous section.

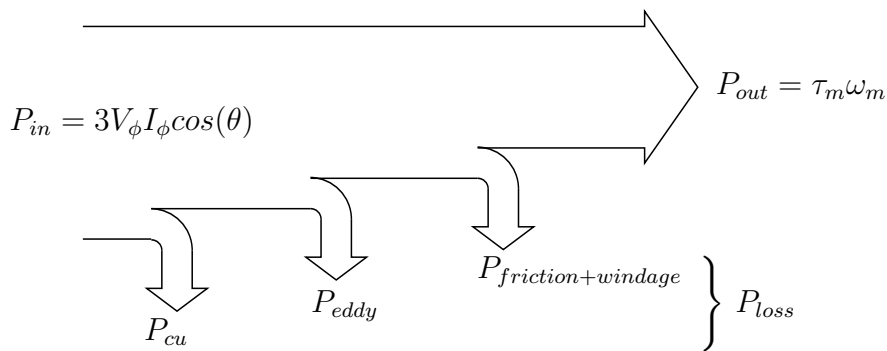


Figure 3.16: Power flow during motor operation.

Copper loss is equated by

$$P_{cu} = 3I_a R_a \quad (3.12)$$

Resistance per phase of the coils was calculated theoretically as follows

$$R_a = \frac{l_{mc} N q \rho_{cu}}{a_{cu}} \quad (3.13)$$

with  $l_{mc}$ ,  $q$  and  $a_c$  the mean coil turn length, number of coils per phase and cross sectional copper area per wire respectively. Resistivity  $\rho_{cu}$  is adjusted for an assumed coil temperature of 50°C and equated by

$$\rho_{cu} = \rho_0 \cdot (1 + \alpha_{cu} \Delta t) \quad (3.14)$$

with  $\rho_0$  the resistivity of copper at 20°C and  $\alpha_{cu}$  its thermal coefficient. This gave a phase resistance of 0.175  $\Omega$ . In the case of motor operation, output power is the product of output torque and shaft speed, which are known from the FEM simulations. Using (3.12) and (3.10), efficiency can be equated as

$$\eta = \frac{P_{out}}{P_{out} + P_{cu} + P_{eddy}} \quad (3.15)$$

Theoretical efficiency was calculated for the constant torque speed range, as displayed in Figure 3.17.

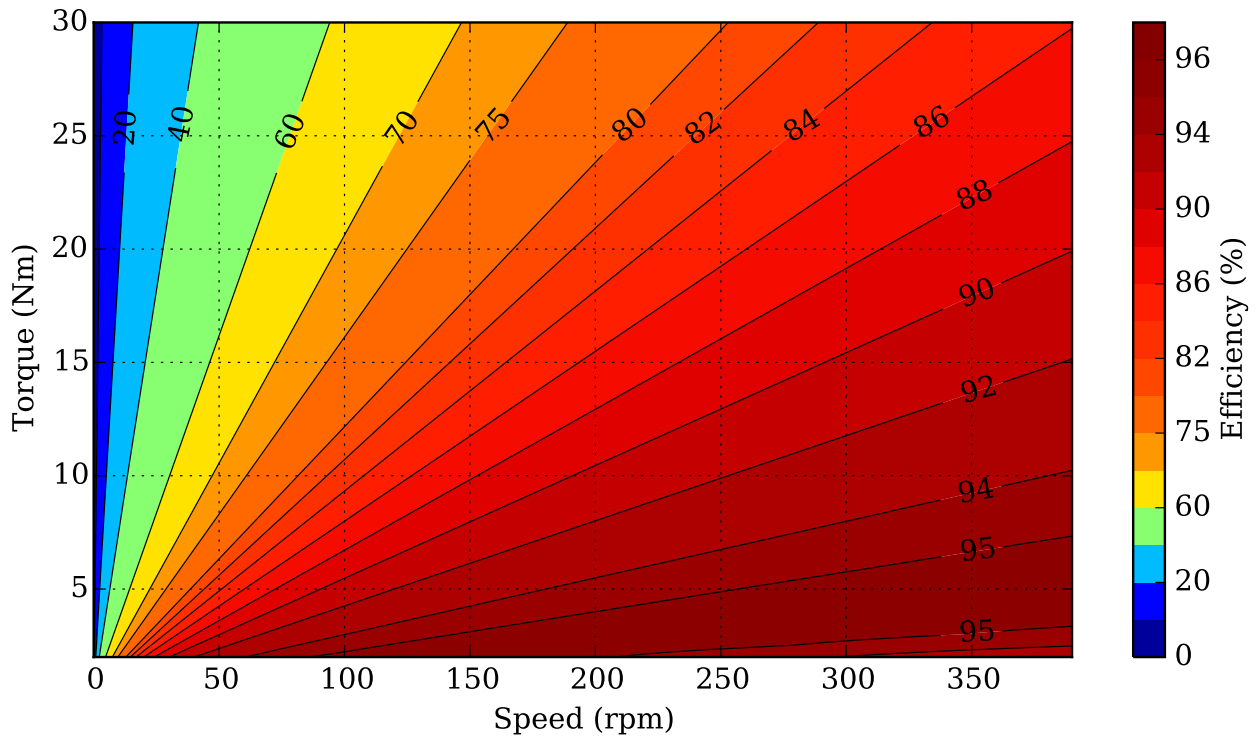


Figure 3.17: Efficiency contour.

The machine should achieve efficiency above 92% at its intended cruising point above 250 rpm and below 10 Nm. Higher torque should only be necessary for short burst, but even the maximum torque of 21 Nm should be achieved at approximately 88% efficiency at the cruising speed of 290 rpm.

This efficiency contour illustrates a key benefit of the air cored and ironless machine over conventional machines with iron yokes and cores. In the latter, losses are incurred even at no load over the entire speed range due to alternating magnetic fields passing through iron components when an alternating voltage is applied.

### 3.9 FEM Benchmark

As a precaution, solutions from the Maxwell<sup>®</sup> software were benchmarked against an alternative software to assure validity of the designs. An in-house package, SEMFEM, was used for this purpose. Development of this package incidentally used an earlier version of Maxwell as a benchmark [7]. Figure 3.18 displays results calculated by both software packages for identical machines. The results compare favourably, indicating an average discrepancy of less than 0.3 Nm.

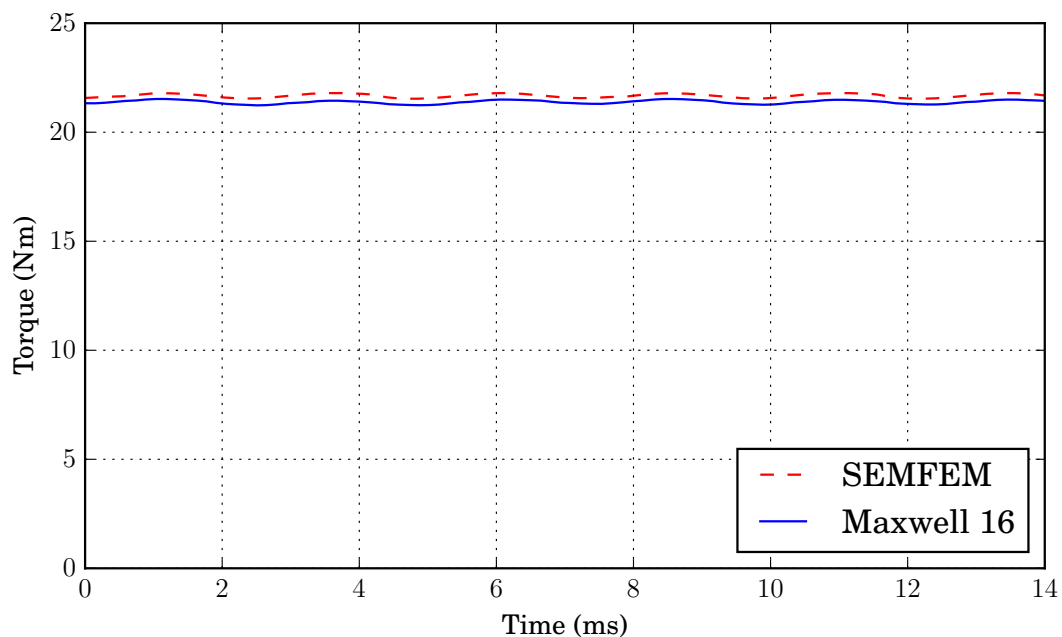


Figure 3.18: Benchmark of FEM software.



## Chapter 4

# Structural Design & Manufacturing

Design of the structural components was initiated before electromagnetic design was complete. CAD models were parametrized such that small dimensional changes could be implemented concurrently with developments in the electromagnetic design, ensuring that structural considerations were taken into account at an early stage. Eventually, when electromagnetic design met basic performance requirements, major dimensions were frozen and detail design of the structural components was completed in order to facilitate manufacture. The true challenge was to design a structure which could serve as a wheel for the SEM vehicle and maintain performance of the motor under the loads that would be experienced by the vehicle during races. This chapter will discuss the design choices and manufacturing challenges that shaped the latest IDRFPM prototype's final form.

### 4.1 Material Selection

Before discussing layout and structural design, it is important to motivate the material chosen to comprise the prototype and discuss some of its important characteristics. The material chosen would have to help exploit the potential of the IDRFPM topology to improve torque density while providing a robust structure fit to support and propel a SEM vehicle. In light of the existing aluminium prototype, the project sought a leap forward, and a more advanced material was warranted.

#### 4.1.1 Composites

At a very early stage, composite plastics were identified as a primary candidate for the structural material. More specifically carbon fibre reinforced



plastic (CFRP), which boasts incredible stiffness and strength characteristics while being much lighter than aluminium. While carbon fibre strands themselves offer around double the tensile strength of aluminium with less than 60% of the mass, the fibres must be oriented in different directions to achieve the same isotropic strength characteristics. CFRP laminates with multiple layers in different orientations are called quasi-isotropic CFRP. Taking this into account, CFRP parts generally save around 30% of mass over their aluminium counterparts. The primary downside to this advanced material is cost. High cost is not necessarily because of the material itself but, as will be discussed in Section 4.3, because of the complex mold process and consequent poor repeatability that often results in duds. Such complexity ultimately consumes the most valuable commodity of all: time.

However, one must recognize that cost would be relatively high regardless of material choice for these prototypes because of their size and uniqueness. Nothing apart from fasteners, bearings and tires could be bought off the shelf. If instead solid metal or engineering plastics were chosen, large diameter components would have to be machined from massive billets of material for every prototype. While the molds for CFRP parts also require machining of billets, they can be reused and modified with relative ease. In the event of a failure or modification, the cost of laying up a new part in the existing molds is much less than the billet and machining cost of a new part made from a solid material.

In the case of the prototypes built for this project, prepregated or "prepreg" material was used. This refers to fibre fabric delivered with resin already applied, as opposed to dry fabric being positioned and then applying resin mixed on the spot. Prepreg material offers better uniformity of the laminate throughout the part but does require curing in an autoclave. However, the vacuum packing process for an autoclave helps improve accuracy of features in more complicated pieces such as the IDRFPM prototype. When making larger pieces, dry material and a wet-layup method may be more effective. This method is commonly employed to create canoes and surfboards, and was also used for the fairing and chassis of the SEM vehicle.

### 4.1.2 Other Alternatives

Two alternatives remain, namely casting and 3D printing. Casting is a very complex and expensive process to initiate from scratch. It is best suited for mass production and generally ruled out for prototyping. 3D printing was

strongly considered, but the structural characteristics of components created by printers readily available fall short of the robustness required by the real-world load cases at hand.

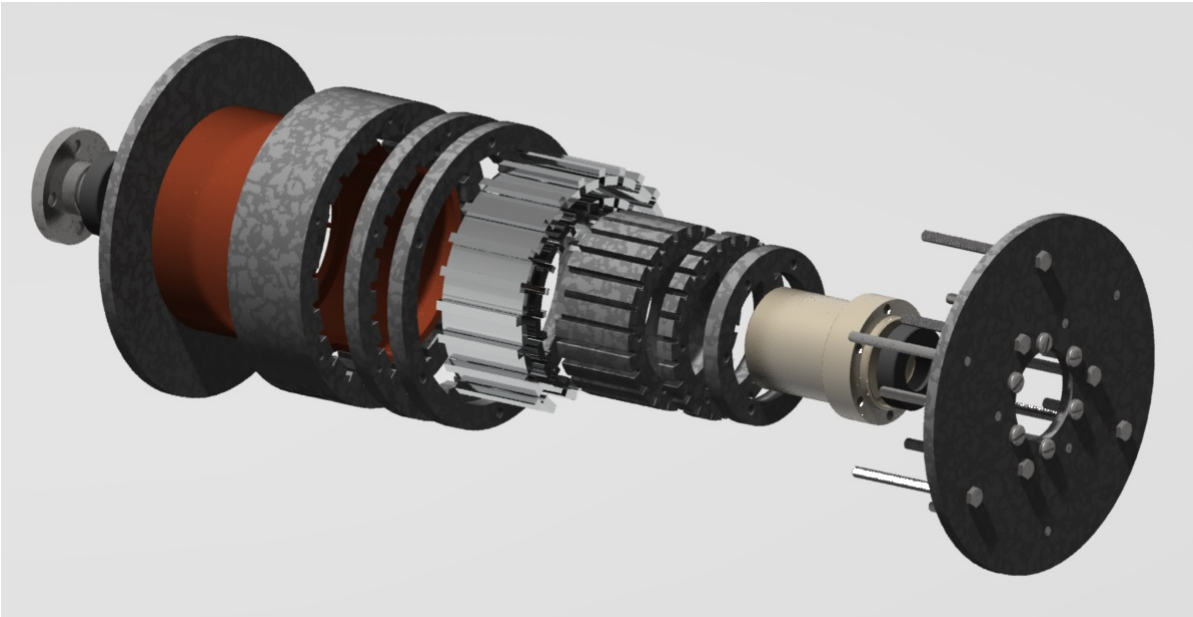
New 3D printing technology has appeared on the market very recently which can print CFRP by laying fibres within the resin matrix through the printing head [1]. While the density of fibres may not be as high, the technology allows precise placement of the fibre layout. This means that each fibre can be optimally oriented to handle a given load, as opposed to large spans of fabric arbitrarily applying fibres in one or two directions. Unfortunately, the technology was not yet available for this project.

### 4.1.3 CFRP Load Behaviour

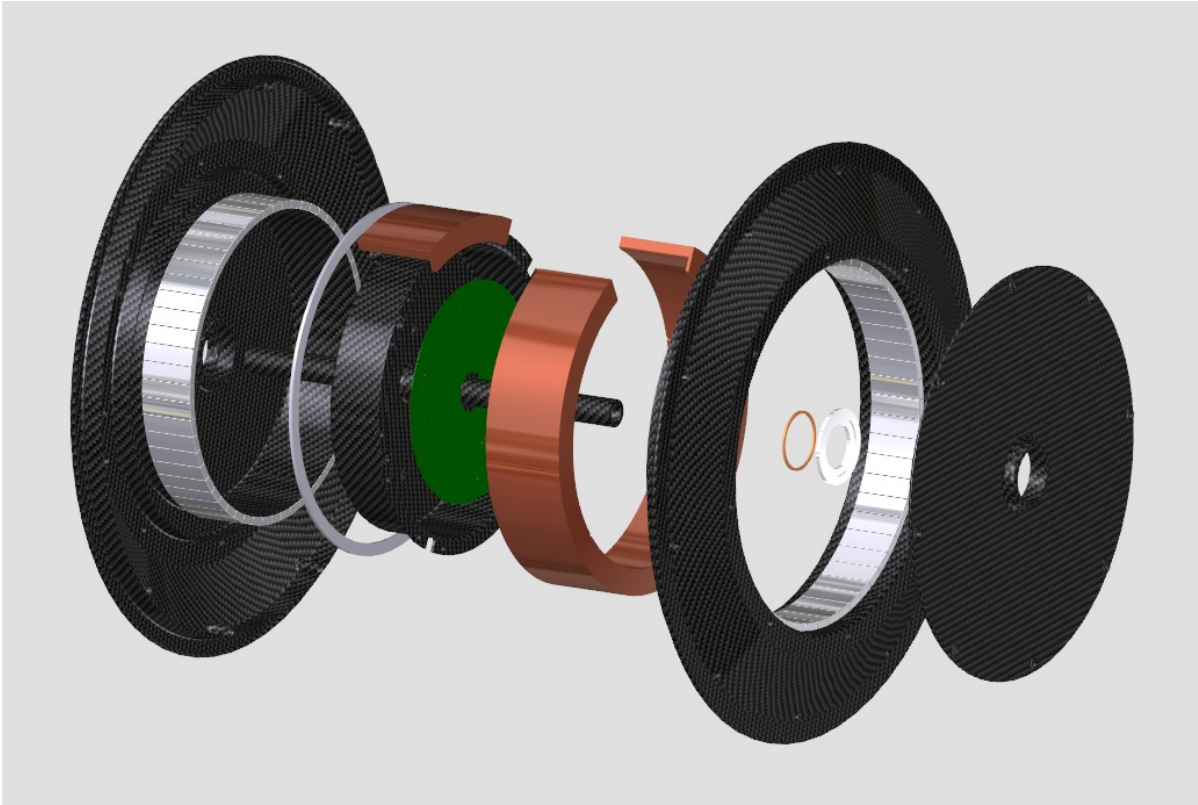
Unidirectional CFRP can handle incredible longitudinal loads, or loads in the direction of fibres. However load performance in the transverse direction, perpendicular to fibres, is mainly dependent on the matrix or resin which bonds the fibres. A compilation of results from a worldwide study of CFRP failure criteria [9] gives strength data on a prepreg material very similar to that used in the prototypes for this project. The study gives longitudinal tensile and compressive strength as 1500 and 900 MPa respectively and a transverse tensile and compressive strength of 27 and 200 MPa for unidirectional material. Failure test data is also provided for quasi-isotropic laminates including a ( $0^\circ/\pm 45^\circ/90^\circ$ ) laminate which is very similar to the laminate structure likely to be used in the prototype components. While the failure data is scattered over a range of values for different load cases, the lowest values were over 300 MPa. Shear stress failures occurred at values above 50 MPa except for load cases with combined stresses over 500 MPa.

## 4.2 General Layout

For the first aluminium prototype, very little was done to minimize structural or passive mass. The design was crude at best, serving its purpose as a proof of concept. The use of CFRP allowed a more minimalist structure that could much better serve the project goal of increasing overall torque density. Figure 4.1 shows exploded views of the aluminium machine and the first CFRP design. Figure 4.2 shows section views of the machines. The larger hollow spaces in the CFRP design illustrate the impact of the minimalist structure to which this material lends itself.

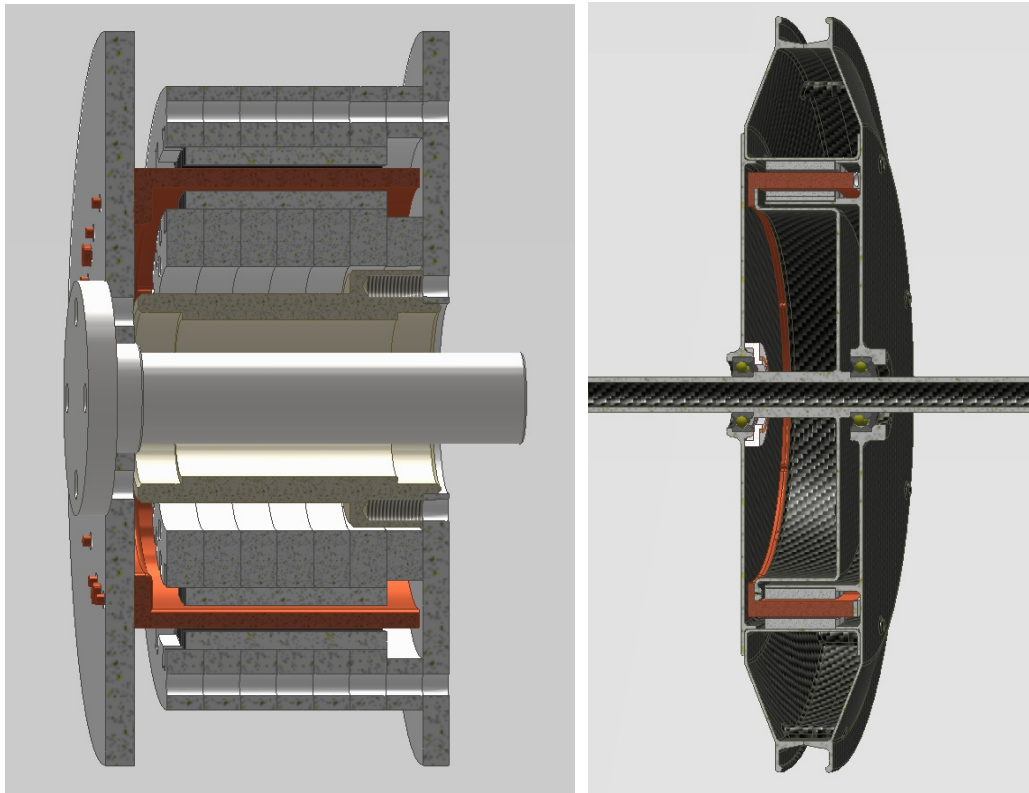


(a) Aluminium prototype.



(b) Preliminary CFRP concept.

Figure 4.1: Exploded views.



(a) Aluminium prototype.

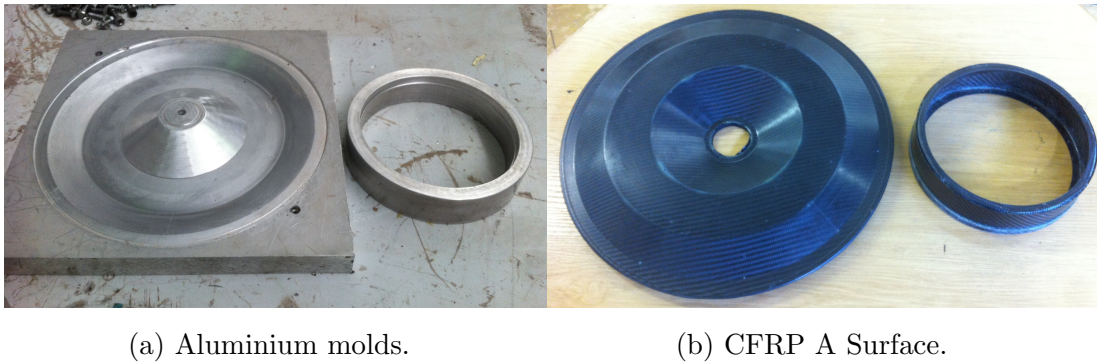
(b) Preliminary CFRP concept.

Figure 4.2: Section views.

Working with CFRP also offered the design flexibility of being able to add layers of material without changing key shapes or locating surfaces. In other words, a basic shell could be designed with designated A surfaces, or surfaces precisely defined by the mold in which the part is made. Surfaces not defined by mold shape, or B surfaces, could then be bolstered by applying extra material with resin at any time, should any critical stress areas be identified by simulations or practical experience. Figure 4.3a shows an example of the molds used to create parts of the IDRFPM and Figure 4.3b shows the A surface of the parts they create.

It should be noted that preliminary sketches considered the possibility of purchasing a standard bicycle rim and designing a structure with holes for spokes. However, it was decided that the spokes can be very difficult to align and often cause more problems than they solve. Instead the rim feature was extended out to the full diameter. The two designs are shown in Figure 4.4.

The initial design positioned two bearings on either side of the stator. The



(a) Aluminium molds.

(b) CFRP A Surface.

Figure 4.3: CFRP molds and parts.

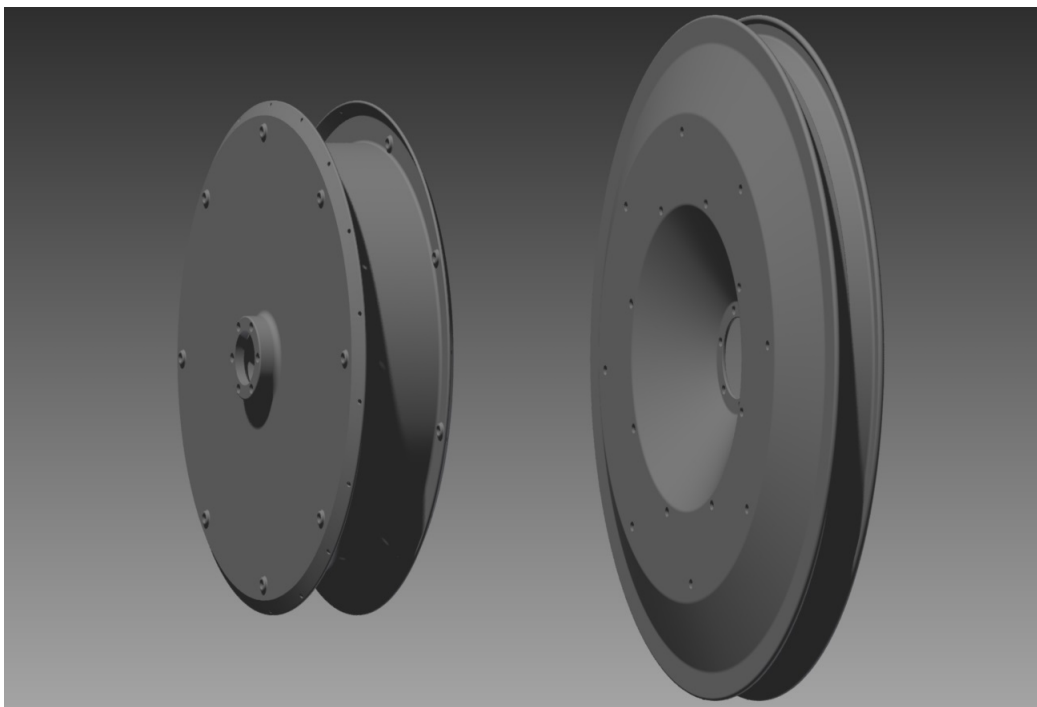


Figure 4.4: Rim configurations: Spokes (left) vs. full rim (right).

rotor structure created a closure completely containing the stator coils and stator structure. Increasing the distance between the bearings would increase the structure's capability of handling lateral forces experienced during cornering. The closed structure would also prevent debris from entering the air gap. Initially it was decided that a cavity could be left inside the stator sufficient to contain the drive electronics necessary to control the machine. This would offer a relevant design study of the potential of the IDRFPM and the kind of final product it could become. The green disc in the exploded view in Fig-



Figure 4.1b represents the printed circuit board (PCB) and where it would be positioned inside the stator “bucket”.

### 4.3 Manufacturing Difficulties

Unfortunately, severe problems arose once parts were completed and fitted due to the behaviour of CFRP during curing. The resin in the prepreg material begins to set at a relatively high temperature while the aluminium molds continue to shrink in size as they cool down. This causes warping in the parts which creates problems for important locating surfaces and bearing seats. It is possible to adjust curing and de-molding techniques to meet tolerances right out of the autoclave, but this requires many iterations which this project could not afford. Figure 4.5 shows the first set of parts. They appeared to be flawless, but closer inspection revealed upwards of 2 mm runout oscillation at the outermost rim in the axial direction. Only after a series of machining operations did the bearing seats and other locating surfaces manage to achieve acceptable runout tolerances.



Figure 4.5: First completed CFRP parts.

Considerable difficulties also arose during the magnet mounting process. This was mostly due to the static forces acting on magnets in a segmented

quasi-Halbach array, as shown in Figure 4.6. Forces on the magnets are also much higher once the inner and outer magnet arrays are brought near each other.

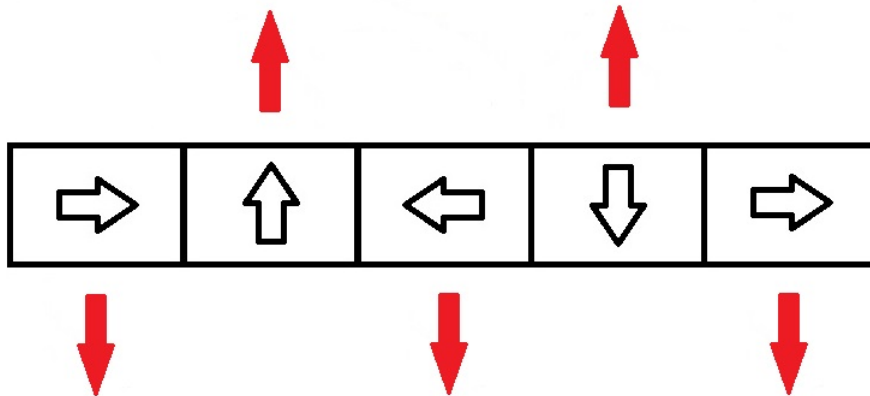


Figure 4.6: Forces on magnets in segmented quasi-Halbach array.

The original strategy was to glue magnets one by one, clamping them in place after applying them to the rotor surface. It was quickly deduced that without an accurate form of spacing, small inconsistencies would result from manually placing each magnet and ultimately result in either a gap between the last two magnets or too little space for the last magnet. The solution was to mount all of the magnets simultaneously. To this end, frames were created to constrain the magnets in place while glue or resin could be applied. They were affectionately referred to as the “cake frames”, seen in Figure 4.7, and included an open slit with protruding loops nearby in order to force the frame open or closed with a threaded rod.

At first, steel was used because it is cheap and easy to turn into the correct shape, welding on loops for the threaded rod. For the outer set of magnets, the frame worked perfectly, but the inner set proved more difficult. Whereas the outer magnets were constrained in part because of their geometry, the inner magnets pulled toward the steel frame and escaped the grasp of the glue, which necessitated the creation of a plastic rim, also seen in Figure 4.7.

This new method opened up a discussion for other manufacturing possibilities. To improve structural integrity, a layer of carbon fibre weave material was placed between the magnets and the cake frame and folded over the rim.



Figure 4.7: Magnet constraining frames.

As shown in Figure 4.8, the layer successfully constrained the magnets. Unfortunately, this layer interfered with the air gap left between the magnets and coils. If all the other components were perfectly aligned this may still have worked, but compounded alignment problems prevented this layer from being a viable solution.



Figure 4.8: Inner rim magnets with CFRP layer.

The process of fixing the magnet arrays proved to be the most difficult manufacturing challenge, ultimately requiring many painful iterations and failures before finally achieving success. The inner array of magnets were particularly difficult, at one stage being influenced by the warped and misaligned parts. Before the magnet gluing process began, the inner magnet surface had to be



machined in order to reduce a severe runout oscillation. Unfortunately, this reduced the thickness of the material to a degree that severe deformation occurred during mounting of the magnets, as shown in Figure 4.9.



Figure 4.9: CF deformation during magnet mounting.

## 4.4 Revision & Final Prototype

When the completed components were finally assembled to assess the first CFRP prototype, it was clear that collecting useful data from the machine would be very difficult due to interferences between rotating and static surfaces. It was determined that enough funds were present to create one more revised prototype, which presented an opportunity to make numerous adjustments to ensure success of the prototype. The most notable changes are those made to the overall layout, as displayed in Figure 4.10.

The bearings were rearranged to support only one side of the rotor, with the other side omitted completely. By the time the layout was revised, it had been decided that no electronics other than position sensors should be mounted inside the motor to better facilitate repairs or modifications that may be required during a race. Thus, the stator structure could be drastically altered, allowing the rotor component to form a cone protruding inward as shown in Figure 4.10B. This protrusion positions the rotor mount directly under the middle of the tire rim such that vehicle mass causes no moment about the mounting point. The CFRP rim was also altered to mount onto an aluminium hub instead of directly forming the bearing seat. This offers further control over tolerances and alignment of the machine. The conical shape of the protrusion also bolsters rigidity of the rotor to compensate for the fact that

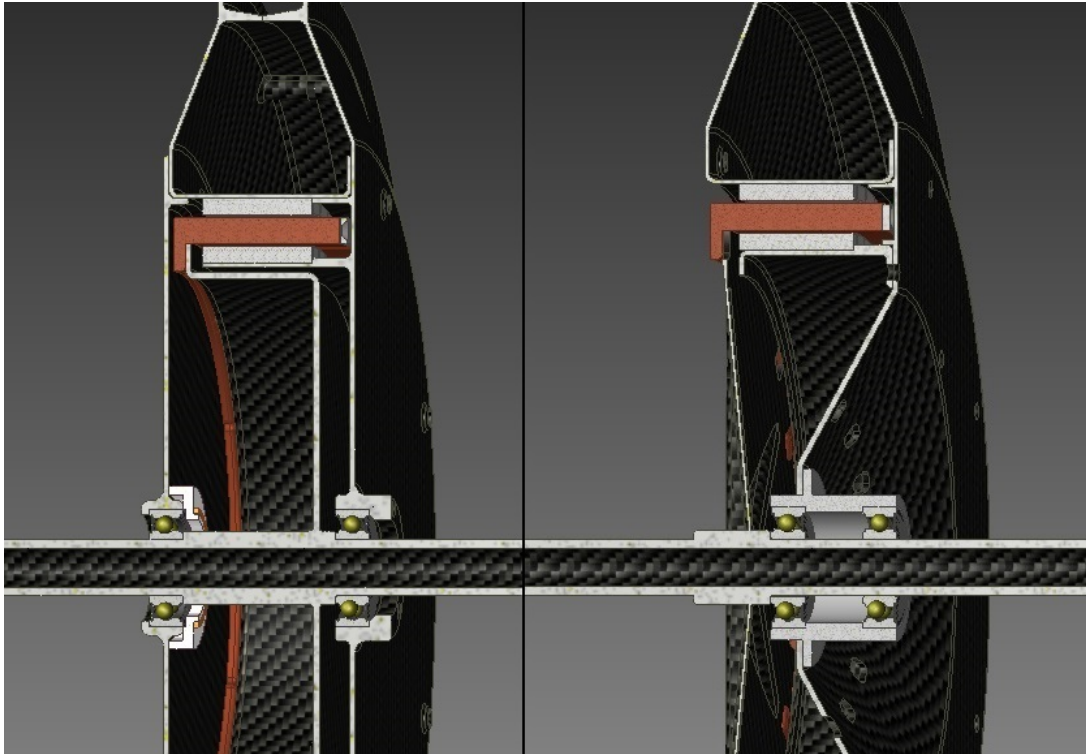


Figure 4.10: Initial (left) and revised (right) layout.

the same forces must now be supported on one side of the stator rather than two.

Another major improvement was the separation of the inner magnet rim as a separate component which mounts onto the rotor plate. The magnet gluing process greatly benefited from being able to handle the rotor surface separately. As a part of this change, the locating surface was formed by machining away bulk material instead of being formed directly by the mold. This change was also incorporated for the mounting surface of the outer magnet rim and greatly improved alignment of the parts.

Along with the changes to CFRP parts, the decision was made to sacrifice performance and reduce magnet thickness by 0.5 mm in order to provide ample space for the carbon fibre layers over the magnets. The magnets had to change because the molds could not be changed. The outer rotor mold could be machined away to increase diameter for an increase in outer air gap, but the inner mold would require material to be added to reduce diameter for an increased inner air gap.

A full assembly drawing with a parts list is included in Appendix D.

## 4.5 Structural Integrity

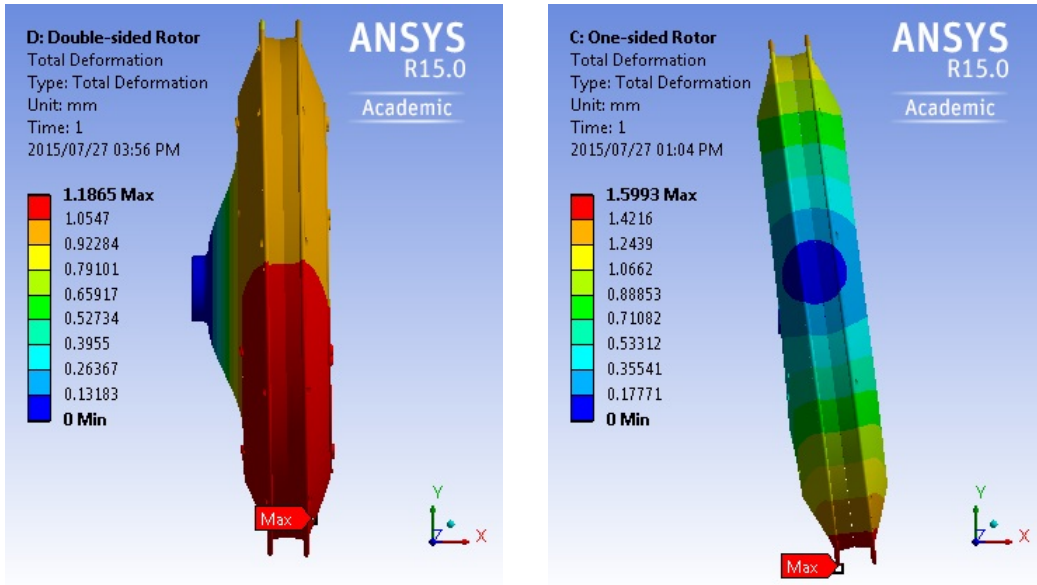
A set of simulations were created using ANSYS Mechanical FEM software in order to obtain an estimate of deformations and stresses in the structure under load conditions. Strength analysis of structures to be made of CFRP is complicated by the inherent variability of material characteristics and uniformity on the day of manufacture. While the FEM simulations are not intended to give results that will be accurately matched in practice, they help identify weak points in the design and determine the relative effect of various features and shapes. Uniform material characteristics were assigned, not taking into account layers or fibre direction. These simulations became most relevant when the layout was changed such that the rotor is only supported on one side.

### 4.5.1 Rotor Components

The most threatening load case for the rotor components is the lateral force while cornering at high speed combined with the vertical force from gravitation acting on the vehicle mass. In Section 3.1 vehicle mass is identified as approximately 85 kg. Lateral force from cornering is limited by the amount of force that will cause the vehicle to flip. This is determined in Appendix B to be approximately 280 N. For both lateral and vertical directions, the force would actually be split between the front and rear wheels. However, forces were taken as acting entirely on the rear wheel to ensure a conservative design. Figure 4.11 shows the total deformation for the original rotor design and the revised layout, approximately 1.2 mm and 1.6 mm respectively.

Deformations are exaggerated in the image to show where the largest deformations occur. In both designs the strain occur primarily where the structure plane is perpendicular to the lateral cornering force. The conical structure extending from the outer boundary of the magnets to the outer rim inherently offers better rigidity than a flat structure.

While small, the deformations shown in Figure 4.11 are not negligible and merit further investigation to determine if the structure would achieve its primary goal: maintaining the air gap inside the machine. With the added layer of material which constrains the magnets, the air gap will be less than 1.5 mm. However, the total deformation is mostly in the axial direction, which will not necessarily affect air gap. Figure 4.12 shows maximum deformation on the one-sided rotor in the Y-direction to be less than 0.3mm, which is well below



(a) Two-Sided rotor

(b) One-sided rotor.

Figure 4.11: Total deformation.

the 1.5 mm gap length. Even if the actual deformations in the machine are double what they are calculated to be here, the simulation indicates that the relative effect on the air gap is unlikely to pose a threat.

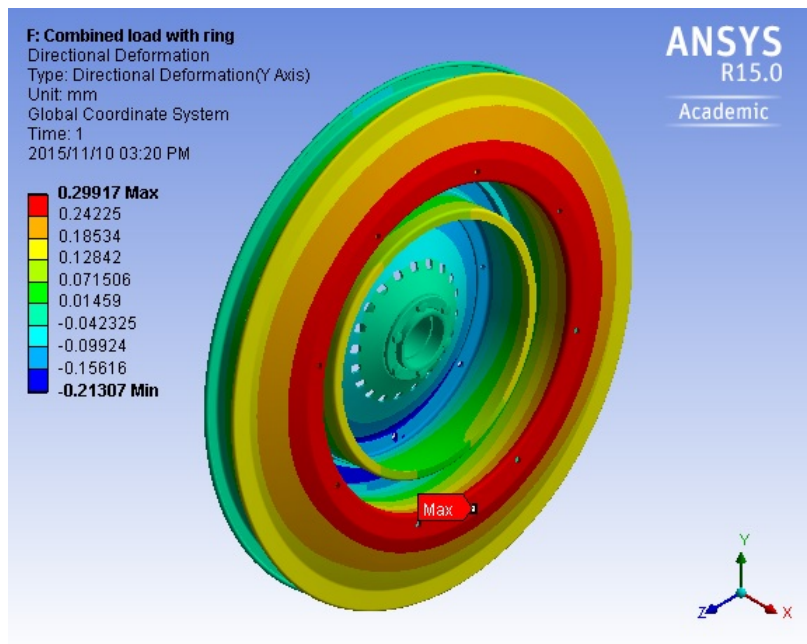
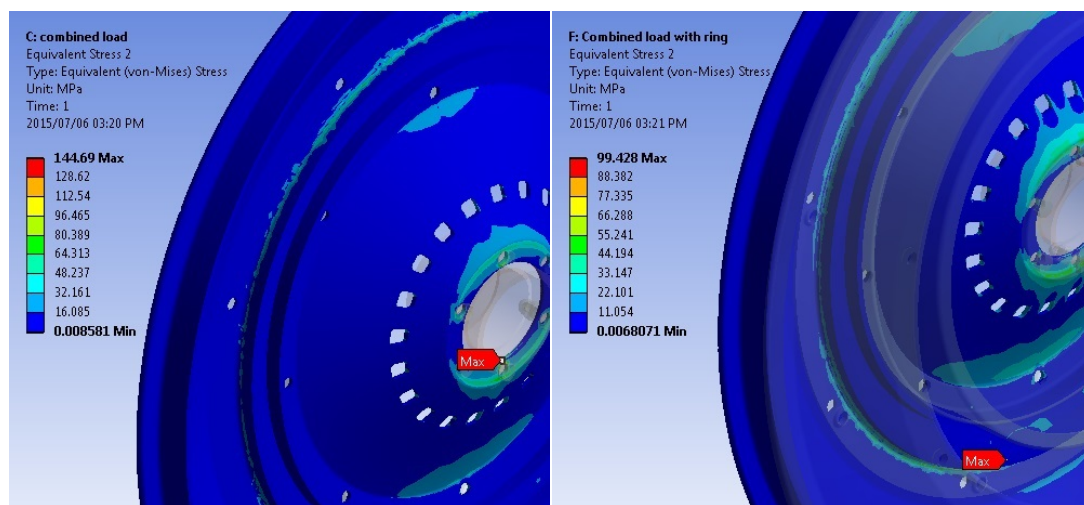


Figure 4.12: Deformation in Y direction.

Thus, the simulations gave an overall positive impression of the structural

integrity of the rotor under load. However, attention must be paid to stress concentrations. Figure 4.13a indicates that the maximum stress occurs in the main CFRP rotor component, concentrated around the bolt fastening it to the aluminium hub. This stress concentration was relieved by including another aluminium ring between the bolt and the CFRP, shown in Figure 4.14, effectively sandwiching the edge between aluminium and distributing the force. Analysis of the revised design indicates that the maximum stress is now elsewhere and has dramatically reduced, as shown in Figure 4.13b. The new maximum stress of 99.4 MPa falls well below the limits identified in section 4.1.3.



(a) Concentration around bolt.

(b) Reduced stress due to added ring.

Figure 4.13: Stress concentration analysis.

This is an example where the ability to add reinforcing material came to the fore. Material was added around the hub location area and machined to the correct tolerance in order to improve the footprint of the fit between the CFRP rotor and the ring.

Figure 4.15 displays the maximum shear stress, focused on a small point on the outside of the inner magnet rim. This maximum still falls below the limit identified for shear stress identified in section 4.1.3. The point at which the maximum occurs is also a non-critical area where failure should not have drastic effects on preservation of the air gap.



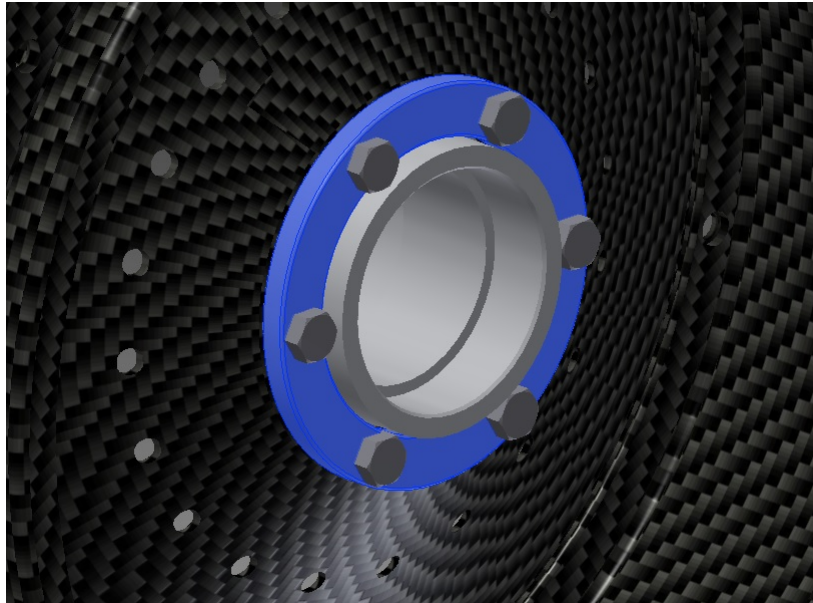


Figure 4.14: Ring on rotor mount to relieve stress concentration.

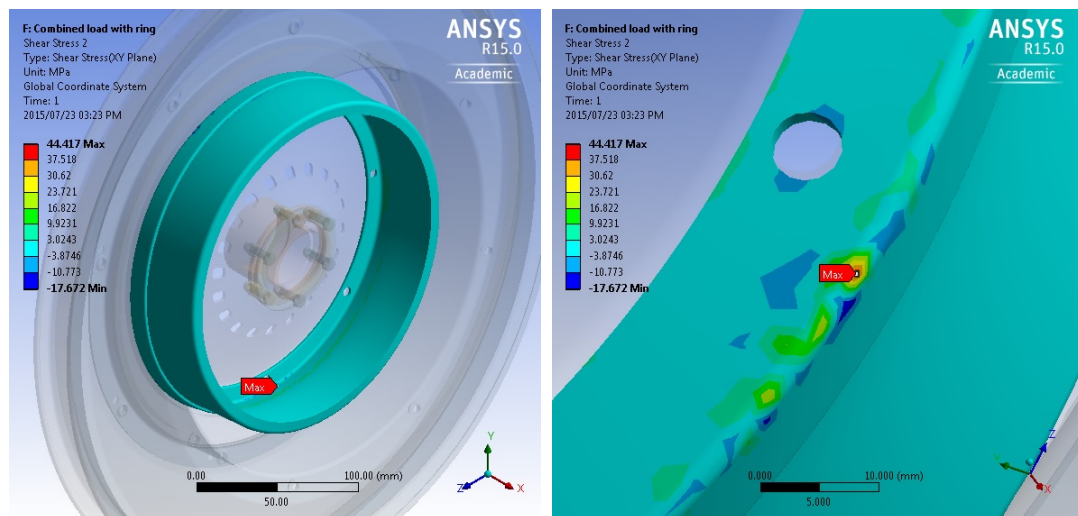


Figure 4.15: Rotor shear stress.

## 4.5.2 Stability

Before continuing with discussion of the stator, it must be noted that structural integrity and operational stability are closely related but separate characteristics. Stability of the machine during operation is dependent on the minimization of vibrations, which can result from various factors. The author recognizes the potential for even small vibrations in the machine to adversely affect performance of the vehicle it is meant to propel.

The air cored coils eliminate cogging torque, so torque ripple and the resulting vibrations should be minimal. All other vibrations in the machine will result from imbalances due to manufacturing imperfections or small misalignments. This means that reduction of vibrations is a matter of manufacturing technique rather than mechanical design, at least at this stage of prototyping. As such it is difficult to quantify and also deemed beyond the scope of this project.

### 4.5.3 Stator Components

The stator coils will only experience tangential forces and small radial forces. Assuming the stator consisted simply of a flat plate with forces applied to its outer edge acting only tangentially, the forces would all act in the in-plane direction and not pose much threat to the structure. However, any imbalance in the forces would cause a moment about the center point of the flat plate. In both the original and revised layouts, the centre of the stack length was offset from the point at which the stator structure attached to its central shaft portion. This means that any radial forces could potentially cause severe deformation if the stator structure is not strong enough.

Radial forces can generally occur because of minor imperfections in the machine construction. Perfect symmetry is difficult to facilitate in practice. If adequate precautions are not taken, this can have catastrophic effects in electric machines due to the exponential relationship between magnetic force and distance. The IDRFPM reduces risk in this regard because of its air cored stator coils, whereas iron cored stators are attracted to rotor magnets and must withstand this force. Nevertheless, the air cored stator must remain stable during operation in order to maintain the air gap. To this end, the stator plate was given ribs extending radially from the centre tapering towards the outer portion where moment will be less for a given force.

An arbitrary remote load was placed on the stator assembly in addition to a 30 Nm max torque to determine deflection, as shown in Figure 4.16A. Figure 4.16B indicates that the maximum total deflection is a mere 0.3 mm. It can also be seen that deformation is primarily in the tangential direction due to the torque moment.

Maximum stress according to this simulation is 95 MPa, shown in Figure 4.17, which is well within safe limits.

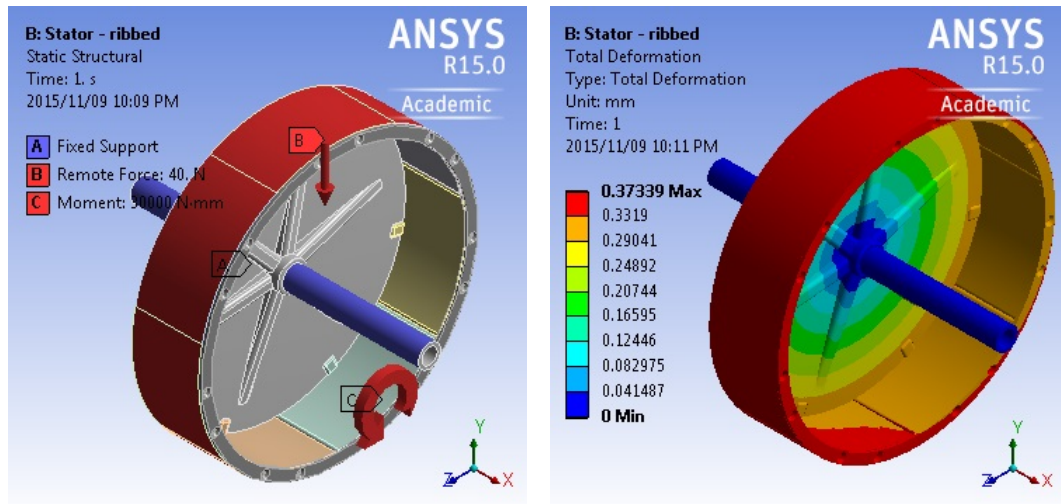


Figure 4.16: Stator load and deformation.

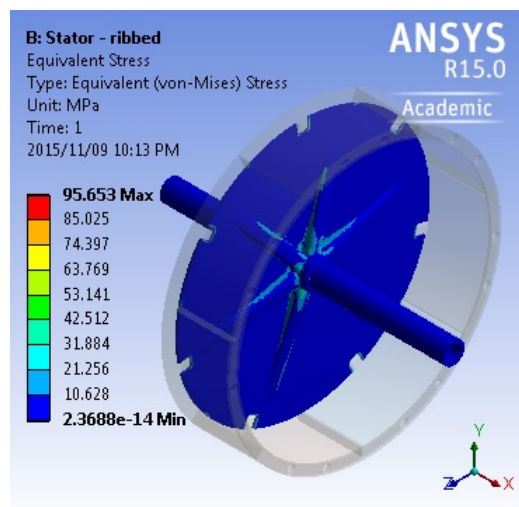


Figure 4.17: Stator stress.

## 4.6 Coil Structure

The coils are constrained by means of epoxy resin. An aluminium mold was CNC machined, shown in Figure 4.18, which would create mold pieces with three coils each and seven pieces total. The coils were wound around Tufnol<sup>®</sup> blocks and placed in the mold, after which the mold was closed, sealed and filled with epoxy resin. This process is depicted in Figure 4.19. The hardened resin can withstand temperatures equal to the maximum curing temperature. In this case the pieces were cured at 120°C, the maximum temperature the enamel on the copper wire can withstand.



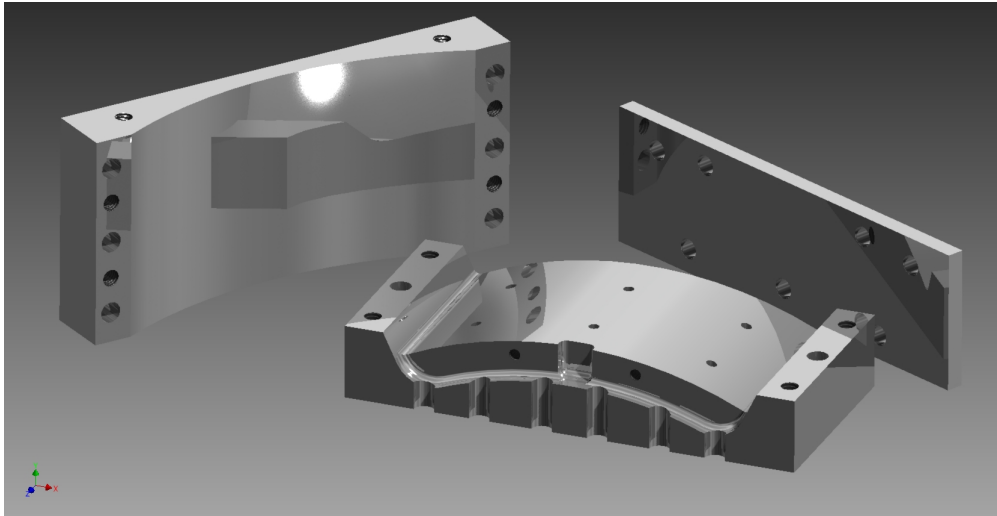
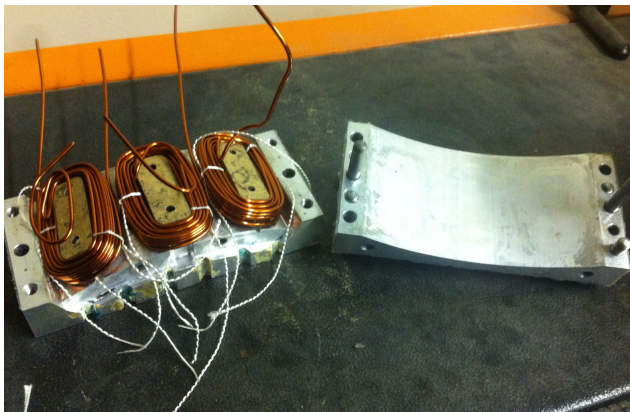
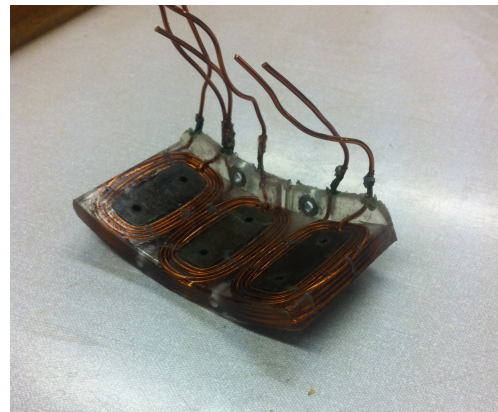


Figure 4.18: Mold design for coils.



(a) Coils ready to be cast in resin.



(b) Finished coil set.

Figure 4.19: Coil mold process.

Each mold piece had to be secured in a manner that facilitated both precise location and ease of assembly. Since the carbon fibre parts would be formed by precisely machined molds, the stator was given a notch in the profile along its outer edge that would correspond with a protrusion on each set of coils. To fasten the coils, two holes per coil set were added to the stator edge corresponding with aluminium studs that would be embedded in the coil structure, as shown in Figure 4.20.



Figure 4.20: Aluminium mounting studs for coils.

The studs were added in order to distribute the concentrated forces of the securing screw. This is a necessary step since epoxy resin is strong but relatively brittle and prone to crack under the pressure of an accidentally excessive turn of a screw. A groove was manually filed into the side of the studs to ensure that they cannot slip out of their position in the resin.

## 4.7 Rotor Hub

The revised design included an aluminium hub on which the rotor plate would be mounted. Design of the hub was fully dependent on spatial constraints and the need to keep aluminium material down to a minimum. Initial sizing of the bearings was based on the premise that a hollow shaft was needed to allow wires to pass through and reach the inside of the closed structure. For the design revision, it was decided to keep the same bearings to ensure a design, but more efficient SKF E2 low-friction bearings were obtained.

As will be discussed in Chapter 6, the prototype was tested as a generator and needed to be driven by a drive motor. Since the IDRFPM is a hub motor, it is impractical to make a coupling to connect the drive shaft from the drive motor directly to the prototype's rotor. Thus, a timing belt was used to transfer power between the rotor and a dummy shaft. As the propulsion unit of a SEM vehicle, the prototype is required include a mechanical brake mechanism. To this end, the pulley was sized such that it could be fit onto mounting holes corresponding with those of a standard bicycle disc brake, as shown in Figure 4.21.



(a) Timing belt pulley.

(b) Brake and calliper configuration.

Figure 4.21: Universal mounting holes on hub.

## 4.8 Structure Mass

According to the Inventor CAD model, mass of the entire assembly, including fasteners, is 5.64 kg. This was very closely matched by the total mass of the prototype, which weighs 6.1 kg without a disc brake, calliper and mounts. The discrepancy can be attributed to certain CRFP walls having been made thicker on the final components to ensure structural integrity. Table 4.1 summarizes a few key mass quantities.

Table 4.1: Mass of various components.

Component	Mass (kg)	% of Total
Total	6.1	100
Magnets	2.478	40.6
Coils <sup>1</sup>	1.096	18.0
Active Total	3.574	58.6
Structural Total	2.526	41.4

<sup>1</sup>It must be noted that the coil mass used to compare topologies in Chapter 3 included resin mass, whereas the resin technically constitutes structural mass. The mass indicated in this table excludes resin mass.

The structural mass accounted for only 41.4% of total mass, which is a positive result considering the structure includes the necessary frame for a bicycle tire. Had the design opted for a third-party rim and spokes, the structural components would have represented an even smaller portion of total mass. By comparison, structural mass constituted approximately 70% of total mass in the the aluminium prototype which preceded this text. Torque density will be discussed once thermal performance has been analysed in Chapter 5.



# Chapter 5

## Thermal Analysis

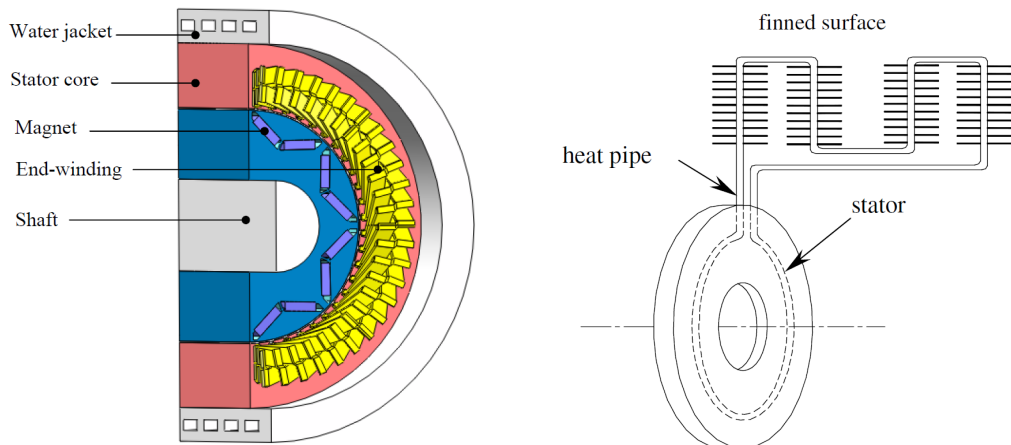
Maximum operating point of the machine is determined by the amount of current which can safely be applied to the stator coils without generating more heat than the machine can safely dissipate. The machine could theoretically dissipate at an infinite rate, but in reality its components will at some point melt or be otherwise adversely affected. It is thus important to analyse the machine's thermal behaviour in order to determine safe operating points.

### 5.1 Heat Dissipation and Cooling Mechanism

Since carbon fibres are good thermal conductors, CFRP exhibits good in-plane thermal conductivity, but through-plane thermal conductivity is much lower due to the resin matrix effectively insulating the fibres. Given also that the stator coils are cast in resin with poor thermal conductivity and that the stator structure lacks any other thermally conductive components exposed to the outside air, it can be anticipated that the machine will have poor heat dissipation without any other active or passive cooling components. As mentioned in Chapter 4, the copper and resin in which the coils were cast can withstand 120 °C. The N48 grade permanent magnets, however, risk demagnetization at temperatures above 80 °C, or 75 °C for a conservative design. It is unlikely that the temperature difference between coils and magnets will be such that the coils overheat before the magnets, so the magnets will be the ultimate focus of thermal analysis.

The hub drive configuration disallows the use of fluid jackets, shown in Figure 5.1a, which are commonly employed to cool electric machines with outer stator structures. While other fluid cooling methods such as heat pipes and fluid circulation inside the stator structure, shown in Figure 5.1b for an axial flux machine, have been suggested, these methods would depend on the availability of non-conductive pipes that are unlikely to be readily available

for this application in the near future [23]. Moreover, a liquid cooling system was deemed beyond the capacity of this phase of the IDRFPM project.



(a) Water jacket cooling[30].

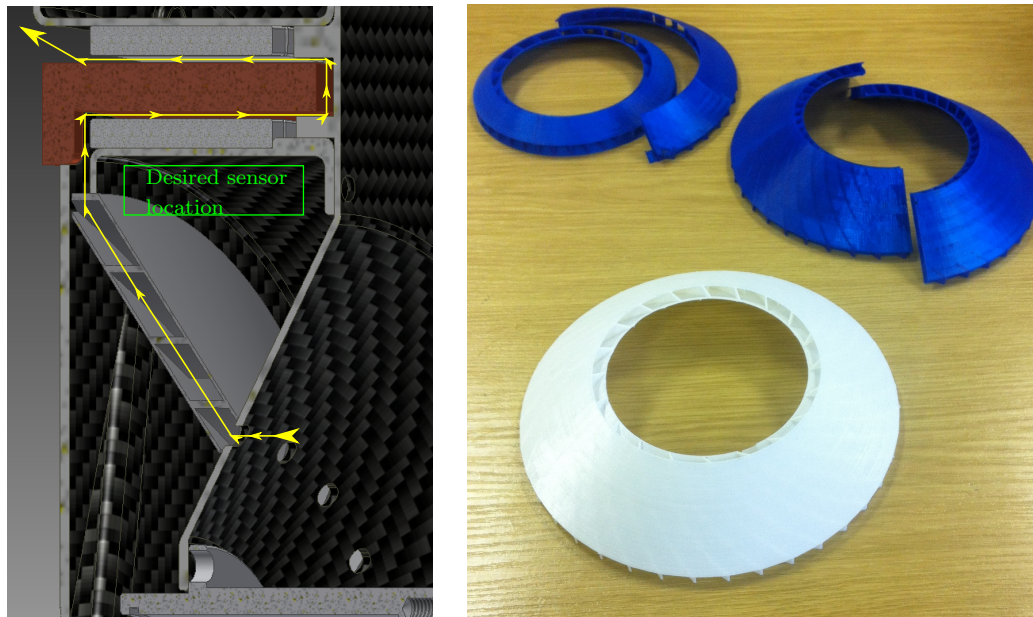
(b) Heat pipe for an axial flux stator [23].

Figure 5.1: Liquid cooling mechanisms.

A more easily feasible option is forced air convection, especially since the revised layout leaves one side of the machine open to ambient air. An active fan could be attached, much like a fan is attached to a desktop computer box to facilitate cooling. However, this would require electronics integrated with the main control electronics since the SEM vehicle is only allowed one battery to power all components. A passive fan attached to the rotor is thus a simpler solution. Figure 5.2a shows the first concept for an impeller fan to be mounted internally, pulling air through the rotor surface and pushing it outward through the air gap. This concept was printed with PLA plastic using 3D printers. Figure 5.2b shows the progression of prototypes, which were first printed in parts before a larger printer was located which could print the fan in one piece.

There were a few critical drawbacks to this design. It requires holes to be drilled into the central cone structure of the rotor, which will reduce structural integrity. The reader will note, however, that these holes were included in the designs on which structural analysis was performed in Chapter 4. The holes would also negatively influence flow in the machine, with the remaining moving rotor structure slicing flow through the holes perpendicular to the desired flow direction as motor speed increases. A more important drawback is that the placement of the fan obstructs a magnetic sensor which was being developed





(a) Impeller fan air flow path.

(b) 3D printed impeller fan prototypes.

Figure 5.2: Impeller fan concept and prototypes.

to facilitate control of the machine. This sensor would need to sit within 6 mm of the inner magnet array's inner surface.

To avoid these drawbacks, an alternative fan was designed. As shown in Figure 5.3a, the fan sits on the outside and draws air through the air gap from the exit point. Holes can be drilled toward the outer radius of the stator, which is a less critical structural support point. These holes will also remain stationary and thus promote better air flow. A central objective of this thermal analysis is to compare thermal performance with and without forced convection from a fan. In doing so it can be determined whether the machine will be able to operate safely without a fan.

## 5.2 Thermal Analysis Approach

The choice of analysis approach depends in part on the overall purpose of the analysis. In the case of this project, it will be very difficult to accurately verify thermal performance with limited access to the inside of the machine. The thermistors placed in the coil structure cannot be taken as absolutely accurate and are slightly insulated from the copper surface. As such, this analysis will struggle to calculate accurate performance figure. Similar to the



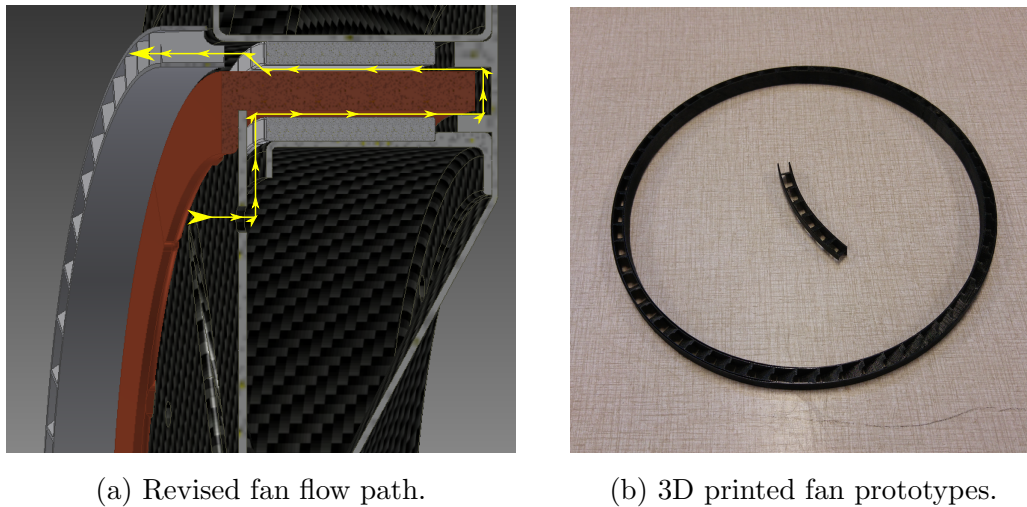


Figure 5.3: Revised fan concept and prototypes.

structural analysis in Chapter 4, this analysis will help indicate the relative effect of various components of the thermal model and of the proposed thermal strategy.

It has become a common instinct to jump towards advanced software and computational simulations due to skyrocketing processing speeds of readily available computers in the last two decades. Even the most intricate computer models will struggle to achieve clear-cut solutions, the worth of which is mostly dependent on the skill and experience of the interpreter. Meanwhile, astonishingly accurate estimates of thermal performance can be achieved from basic heat transfer theory and analysis that can be done basically by hand, and the IDFRPM features relatively simple geometries that lend themselves to such basic analysis. It was decided to forgo software simulation and create a simpler thermal model to get a basic impression of the IDFRPM's thermal performance. This choice was further motivated by the fact that the author already possessed intimate knowledge of the thermal analysis techniques presented in this chapter.

For either analysis method, a stumbling block is the flow rate of the forced convection, which must be a known predefined variable or a function of rotational speed. This would require characterization of the 3D printed fan designed from scratch, which is no simple matter. Customized equipment is required to create the necessary environment in which flow created by the fan can be accurately and reliably measured. The only alternative is CFD analysis, which is vastly more complex than the other computational analyses

performed in this text. Instead, analysis performed in this chapter will assume a range of realistic flow rates which will adequately indicate the relative effect of forced convection on overall thermal performance of the machine.

Basic thermal analysis equates heat transfer in a given system as a circuit diagram with resistances. A material with lower thermal conductivity will equate to a higher thermal resistance and vice versa. Figure 5.4b gives an approximated thermal resistance network for the corresponding section of the machine shown in Figure 5.4a.

The first step in creating a thermal model is to determine a set of assumptions about the behaviour of and interaction between various regions of the model, as will be outlined in the following subsections.

### 5.2.1 Flat Geometry and Symmetry

Thermal resistance of the wall of a hollow cylinder with outer radius  $r_o$  and inner radius  $r_i$  is defined by

$$R_{cyl} = \frac{\ln(r_o/r_i)}{2\pi Lk} \quad (5.1)$$

with  $L$  the cylinder length and  $k$  the material's thermal conductivity, whereas thermal resistance of a flat plate is

$$R_{plate} = \frac{L}{kA_s} \quad (5.2)$$

with  $A_s$  the surface area of the plate and  $L$  now designating the thickness of the flat plate in the direction of heat conduction. In the case of the active components dictating thermal behaviour in the IDRFPM, layer thickness is very small relative to radius. This suggests that each layer can be approximated as a flat plate with length equal to the circumference of that layer. Indeed, when comparing thermal resistances for a given layer using the two methods, the difference is negligible.

From Figure 5.4b it can be seen that the same resistances are present for the inner and outer magnet arrays. While geometry differs slightly beyond the magnet layers, the resistances are still very similar. To further simplify the model, the system is assumed to be symmetrical on both sides of the copper. Surface areas for resistances are taken as the surface on the nominal radius which equates to the average between surface area of corresponding inner and

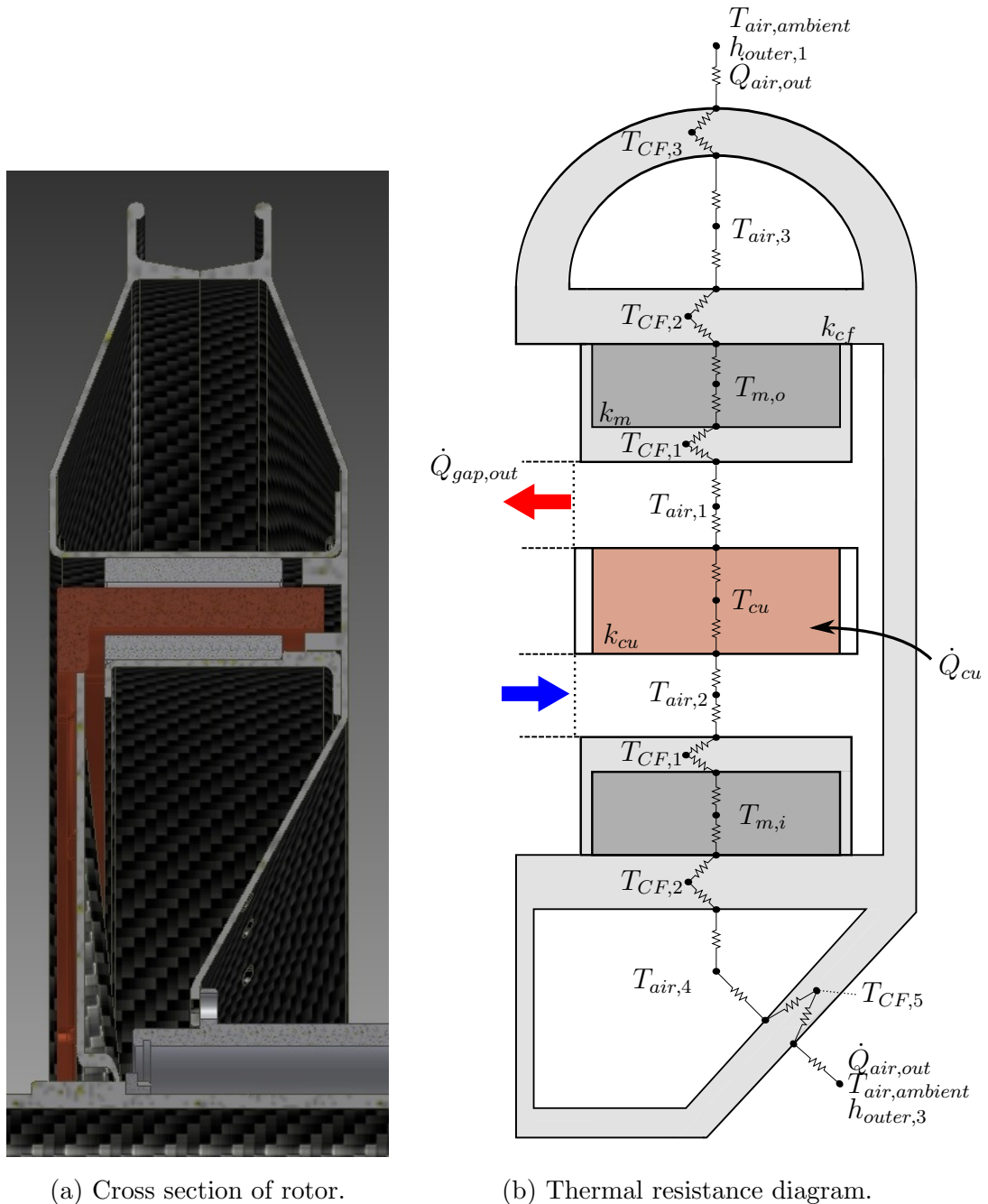


Figure 5.4: Schematic of heat dissipation in the IDRFPM prototype.

outer layers. Taking symmetry into account, the thermal resistance diagram is simplified in Figure 5.5.

The resistance diagram was also further adjusted from the original diagram. Here, only critical temperatures that will be assessed are included. The carbon fibre layer surrounding the magnets will be close enough to the temperature

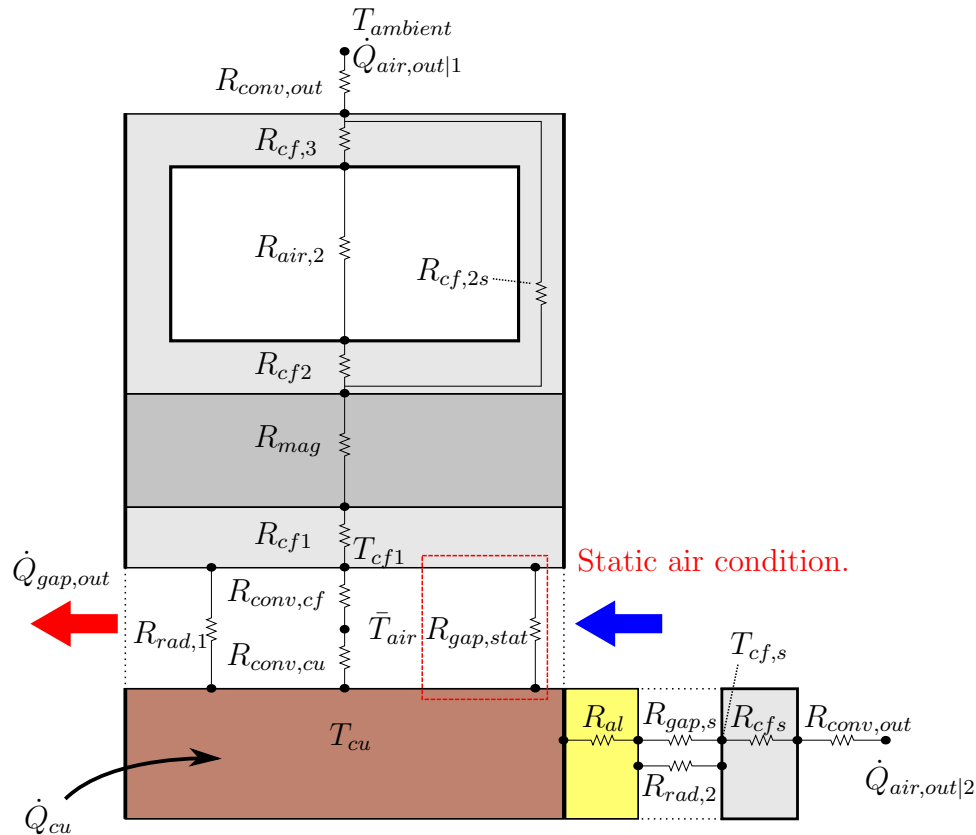


Figure 5.5: Simplified thermal diagram.

of the magnets that its surface temperature can be considered the critical temperature that must be kept below  $75^\circ\text{C}$ . Furthermore, a parallel resistance has been included above the magnet to account for conduction that will occur in the in-plane direction of the frame structure. Another resistance set has also been included for the static air case in which heat will move through the air gap only via conduction and radiation. Corresponding resistances for both the forced convection and static cases were included for the side surface of the coils facing the rotor while the side facing outward was assumed to be insulated.

### 5.2.2 Uniform Bodies and Contact Resistance

Two important assumptions pertain to small irregularities in the construction of the machine. Wall thickness varies in the CFRP structure because of the manufacturing method. In particular, the layer of material added over the magnets will have more irregularities and a few areas where layers overlap.

The magnets consist of a segmented quasi-Halbach array, and not all magnets will be precisely aligned or equally spaced. To simplify the model, the magnets and CFRP were assumed to be uniform bodies of their respective material and also of uniform thickness.

Another factor influencing heat transfer is the interaction between conductive surfaces. On a microscopic level, solid surfaces are uneven and do not make 100% contact. As depicted in Figure 5.6, this inhibits heat transfer and creates a thermal resistance. Mechanical and electrical engineers alike are accustomed to the use of thermal paste, employed to fill the microscopic gaps and improve heat transfer.

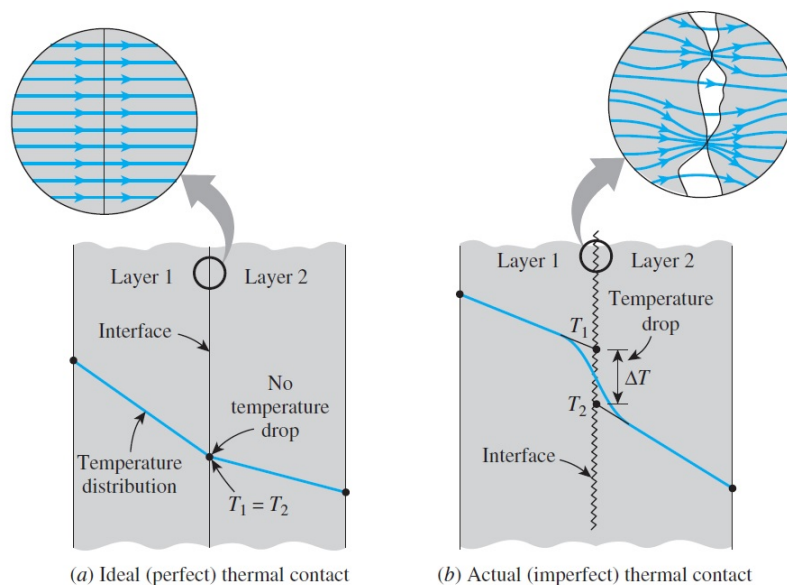


Figure 5.6: Thermal contact resistance [5].

However, since all of the surfaces of CFRP and magnet were bonded together with glue and epoxy resin, thermal contact resistance will be assumed negligible.

### 5.2.3 Coils

A number of assumptions were made to simplify analysis of thermal behaviour in the coils. Since the stranded wires were compressed in a 15 tonne press and wires will be very tightly packed, the coils will be modeled as a solid body of copper. The top and bottom surface of the coils were also pressed very

firmly against the surface of the mold, such that only a very thin film of resin permeated the cloth insulation surrounding the litz wire. This thin film was assumed to offer zero thermal resistance, but the copper surface was assigned the emissivity of resin rather than that of copper. Resin surrounding the coils and the Tufnol blocks around which the coils formed much thicker layers of insulation, which means very little heat transfer would occur through these surfaces relative to the more exposed surfaces. Thus the coils were assumed to be perfectly insulated on their sides, such that heat could only be dissipated on the top and bottom surfaces.

Another matter to consider is the copper generating heat while also conducting heat within itself. In such cases, analysis is often simplified by applying lumped system analysis, which assumes the temperature throughout a body is uniform. The criterion for application of this assumption is the Biot number, equated as

$$Bi = \frac{hL_c}{k} \quad (5.3)$$

with  $h$  the convection coefficient,  $k$  the material's thermal conductivity and  $L_c$  the characteristic length defined

$$L_c = \frac{V}{A_s} \quad (5.4)$$

or volume of the body divided by the surface area of convection. In the case of the coils, the characteristic length corresponds to half of the 9 mm coil height. Lumped system analysis can be applied if

$$Bi \leq 0.1 \quad (5.5)$$

With the thermal conductivity of copper equal to approximately 385 W/mK, the coils yield a Biot number well below 0.1 and lumped system analysis applies.

#### 5.2.4 Internal Forced Convection

Without a fan, air in the air gap will in theory not be transferred into or out of the gap. In this case, heat transfer is reduced to simple conduction through the air, which creates a formidable thermal barrier and offers a very low heat transfer rate. When even a little air is moved through the gap by forced convection, heat can be absorbed by the air and transferred out through

the path shown in Figure 5.3a, drastically increasing the heat transfer rate away from the coils. In order to calculate this heat transfer rate, a convection coefficient must be deduced.

Forced convection through an annulus between concentric tubes is a well documented internal convection scenario. The air gap with a fan forcing air in the axial direction can be equated as such an annulus. The first step is to determine whether or not the flow is laminar by calculating the Reynolds number,

$$Re = \frac{\rho_{air} V_f D_h}{\mu_{air}} \quad (5.6)$$

where  $\rho_{air}$  is the density of air in the gap,  $V_f$  the fluid velocity and  $\mu_{air}$  the dynamic viscosity, all in this case of air at an assumed mean temperature of 50°C.  $D_h$  is the hydraulic diameter, which in the case of an annulus is equal to the difference between inner and outer diameter,  $D_o - D_i$ . Flow is found to be laminar when  $Re < 2300$  for most cases, and is unlikely to be turbulent for flow in a small space such as the air gap at low flow rates. As mentioned before, flow rates will be assumed due to the lack of a characterized fan. The thermal model will be calculated for flow speeds of 0.5, 1.0 and 1.5 m/s. All of these values give a Reynolds number well below 2300.

The next step is to determine the Nusselt number, from which the convection coefficient  $h$  can be determined directly since

$$Nu = \frac{h D_h}{k} \quad (5.7)$$

From the literature [5, p.501], the Nusselt number for annuli with an inner to outer diameter ratio close to unity is given as  $Nu = 4.86$ . With  $h$  now known, convective heat transfer over a surface area  $A_s$  at can be equated by

$$\dot{Q}_{conv} = h A_s (T_s - T_{air}) \quad (5.8)$$

When analysed as part of a network of thermal resistances, convective heat transfer can also be incorporated as a thermal resistance equal to

$$R_{conv} = \frac{1}{h A_s} \quad (5.9)$$

It should also be noted that certain properties of air used to perform these calculations vary at different temperature. Values for air density used to calculate Reynolds number as well as thermal conductivity of air were taken at

50°C for initial calculations. The calculations revealed that the air would actually be at around 70°C in the steady state condition and calculations were adjusted accordingly.

### 5.2.5 Radiation

In addition to convection through air or conduction in the case of no forced convection, heat will be dissipated from the coils through radiation. The maximum rate of radiation heat a surface with given emissivity  $\varepsilon$  can expel is equated by

$$\dot{Q} = \sigma \varepsilon A_s T_s^4 \quad (5.10)$$

with  $\sigma$  being the Stefan-Boltzmann constant equal to  $5.670 \times 10^{-8} \text{ W/m}^2\text{K}^4$ . To account for the view factor and emissivities of two radiating surfaces, net radiation heat transfer from one to the other becomes

$$\dot{Q}_{12} = \frac{\sigma(T_1^4 - T_2^4)}{\frac{1-\varepsilon_1}{\varepsilon_1 A_1} + \frac{1}{F_{12} A_1} + \frac{1-\varepsilon_2}{\varepsilon_2 A_2}} \quad (5.11)$$

Since the coil wires and the carbon fibres are set in epoxy resin, it is appropriate to use a standard emissivity for epoxy surfaces for both surfaces in question. Since the surface areas are also the same, 5.11 simplifies even further. However, solving for surface temperatures is made very cumbersome by the fourth order differential. Thus, as a quick approximation an alternative method proposed in [15, p.16] defines a heat transfer coefficient  $h_r$  for radiation as

$$h_r = 4\varepsilon_1 \sigma T_m^3 \quad (5.12)$$

such that net heat radiation from one surface to another becomes simply

$$\dot{Q}_{12} = A_1 h_r (T_1 - T_2) \quad (5.13)$$

This gives less than 2% error for temperature differences in the range expected for the IDRFPM. This approximation was used for an initial calculation of temperatures for various surfaces. It could then be checked using (5.11), adjusting the coefficient used in (5.13) until radiation heat transfer matched.



## 5.3 Analysis and Results

The assumptions made throughout this chapter were used to executed a set of calculations contained in Appendix C which will be summarized here.

### 5.3.1 Static Air Condition

Calculations for the static-air with no forced convection, the heat transfer rate is not dependent on intermediate thermal balances. However, maximum possible heat transfer is dependent on the amount of heat that can be conducted away from the CF/magnet surface to ambient temperature at critical temperature. This heat transfer rate is equated as

$$\dot{Q}_{net} = \frac{T_{cfr} - T_{amb}}{R_{CF>ambient}} \quad (5.14)$$

with thermal resistance  $R_{CF>ambient}$  calculated from the simplified resistance network in Figure 5.5. Temperature of the coils is determined by applying this heat transfer rate over the thermal resistance between the CF layer and the coils.

$$T_{cu} = \dot{Q}_{net} R_{airgap} + T_{cfr} \quad (5.15)$$

Once coil temperature is known, the heat transfer from the coils through the side structure to ambient air is calculated.

$$T_{magnet} = T_{cu} - \dot{Q}_{net} R_{cu>mag} \quad (5.16)$$

with  $R_{cu>mag}$  the total thermal resistance between the copper and magnet surface. From the calculations in Appendix C, copper temperature for the static air condition is given as 83.13°C and total heat dissipation is 24.32 W. This corresponds with the expected copper losses for approximately 10 A peak current, which would give just over 10 Nm of torque. This is slightly higher than the originally designated nominal rating.

### 5.3.2 Forced Convection Condition

The forced air condition is slightly more complicated because heat transfer through the air gap is dependent on heat transfer to the air being moved through the machine. The copper surface is simultaneously transferring heat

to the air via convection and to the CF surfaces via radiation. These CF surfaces are in turn heated by the radiation and also transfer heat to the air via convection while simultaneously conducting heat to the outside ambient air. Fortunately, the unknown temperatures are easily solved by setting up a system of equations using energy balances at three points: The CF-magnet surface, the side CF surface, and the air itself. The air gap was treated as a control volume for which net heat transfer is equated as

$$\dot{Q}_{airgap} = \dot{m}c_p(T_{out} - T_{in}) \quad (5.17)$$

Noting that net heat transfer in (5.17) must be equal to the sum of convective heat transfer from all surfaces, an energy balance for the control volume can be expressed as

$$\dot{Q}_{airgap} = \dot{Q}_{conv,cu} + \dot{Q}_{conv,cfr} + \dot{Q}_{conv,cfs} \quad (5.18)$$

Where the subscripts *cfr* and *cfs* denote radial and side CF surfaces respectively. The energy balances for the two CF surfaces are equated as

$$\dot{Q}_{rad,i} = \dot{Q}_{h,cfi} + \dot{Q}_{CF>ambient,i} \quad (5.19)$$

and where each form of heat transfer can be expressed in the form

$$\dot{Q}_i = \frac{T_{i,2} - T_{i,1}}{R_i} \quad (5.20)$$

For heat transfer in the control volume, the temperature differential is defined as between the inlet and outlet temperatures. However, for convection to this control volume, the differential is between surface temperature and *mean* air temperature which is equated as

$$\bar{T}_a = \frac{T_{outlet} + T_{inlet}}{2} \quad (5.21)$$

Bearing in mind that inlet temperature is equal to the same ambient temperature used throughout these equations, outlet temperature can be expressed as

$$T_{outlet} = \bar{T}_a - T_{ambient} \quad (5.22)$$

Substituting this back into the energy balances, we now have three equations with three unknowns, namely mean air gap temperature  $\bar{T}_a$ , copper temperature  $T_{cu}$ , and side CF surface temperature  $T_{cfs}$ . With knowledge of the

thermal resistances for each form of heat transfer, the energy balances could be rearranged in system form. In Appendix C, these terms were used to populate matrices with which the unknown variables could be solved.

Once all temperatures were known, net heat transfer rate away from the coils could be equated to determine the effect of forced convection. The calculations were repeated for three different mass flow speeds. The results of the equations are summarized in Table 5.1.

Table 5.1: Calculation results for forced convection case.

Mass flow speed(m/s)	0.5	1.0	1.5
Net heat dissipation (W)	67.75	103.68	138.2
Equivalent peak coil current(A)	15.04	18.61	21.48
Equivalent torque(Nm)	16.02	19.82	22.88
$T_{cu}(\text{°C})$	91.98	100.05	107.81
$\bar{T}_a(\text{°C})$	76.34	75.31	74.32
$T_{cfs}(\text{°C})$	55.21	55.08	54.95

Even for the slowest flow speed, net heat dissipation is more than doubled. Granted these theoretical calculations may not pan out in practice, they offer more than substantial motivation to implement the strategy. The results are put into perspective by the peak coil current associated with the equivalent amount of copper loss and the torque output for this amount of current. It is worth noting that copper temperature increases with flow speed in these equations because the total heat dissipated increases. If copper temperature were kept constant instead of the critical magnet temperature, we would see the temperature of the CF/magnet surface reduce with flow speed increase.

## 5.4 Torque Density

Having determined safe operating points with thermal analysis, comment can be made about the theoretical torque density of the machine. Without any convection, the machine can safely sustain a nominal peak current of 10 A corresponding with approximately 10 Nm of torque. The maximum rated torque of 22 Nm is likely to be sustainable for short periods during acceleration, so a maximum torque density value will also be calculated. According to the CAD

model created in *Autodesk Inventor*, total mass of the machine should be 6.1kg. In Chapter 3, a comparison of topologies comparing torque per active mass. However, the active mass was calculated including the resin in which the coils were cast. To truly reflect torque density for active mass, the resin should not be included. A single coil with 19 turns of Litz wire was weighed to determine copper mass. Furthermore, magnet mass reduced from the figures in Chapter 3 because of the magnet thickness reducing to increase air gap, as discussed in Chapter 4. Torque density for the machine is summarized in Table 5.2.

Table 5.2: Summary of torque density information.

	Mass (kg)	Nominal torque density(Nm/kg)	Maximum torque density (Nm/kg)	Original max. torque density (Nm/kg)
<b>Active</b>	3.58	2.79	6.14	8.37
<b>Total</b>	6.1	1.63	3.60	4.91

These torque density figures are slightly lower than similar axial and radial flux machines in the literature [28, 10]. The CFRP prototype does achieve almost as much torque density per total mass as the radial flux machine in [10]. Optimized topology and a better thermal strategy could yet substantially improve torque density.



# Chapter 6

## Testing and Results

### 6.1 Operational Performance

#### 6.1.1 Test Setup

Performance in motor operation is affected by efficiency of the drive electronics and could reflect poorly on the machine. The power electronic drive system designed in parallel with the CFRP prototype was also not yet ready by the time testing took place. Thus, the prototype was tested in generator operation. The test setup consisted of the following components:

1. The IDRFPM machine to be tested.
2. An *SEW* four pole, 1.5 kW induction motor with a 1500 rpm rated speed on a reduction helical gearbox with 4.27 ratio. This motor was driven by a *Danfoss* variable speed control and used to turn the machine.
3. A *Lorenz DR-3000* torque sensor. The sensor captured both torque and speed, thus also capable of displaying input power.
4. Three adjustable resistance banks.
5. A *Norma 5000* power analyser, which was connected with shunts in series with the resistor banks.
6. A Tectronics<sup>®</sup> four channel oscilloscope was also kept on hand to verify measurements.
7. A multimeter was used to measure the thermistors along with a Fluke thermal imaging camera for thermal performance.

These components are displayed with their corresponding number in Figure 6.1. The test procedure began with a simple open circuit test to determine

voltage constant, followed by a resistive load test using the adjustable resistance banks to determine torque constant. During these tests, waveforms were captured in order to analyse their harmonic purity. During load testing, thermal performance was also recorded.

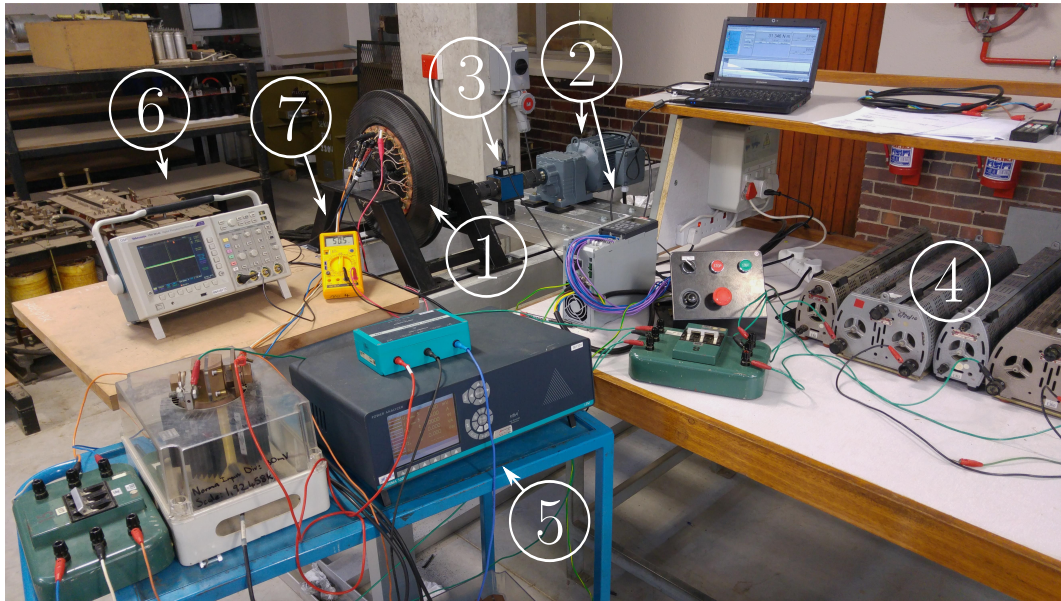


Figure 6.1: Equipment setup for testing.

As a preliminary test procedure, phase resistance and inductance was measured. Average phase resistance was  $0.165\ \Omega$ , very close to the theoretically calculated  $0.155\ \Omega$  value. Average phase inductance was  $102\ \mu\text{H}$ , corresponding very closely with the theoretically calculated value of  $95\ \mu\text{H}$ .

### 6.1.2 OC Test

Figure 6.2 gives phase induced voltage waveforms measured during the open circuit test.

The near-sinusoidal form indicated that no serious mistakes were made in assembly of the magnet arrays and that a functional prototype had been created. Voltage unbalance is visible in the measured waveforms and quantified by an IEEE standard phase voltage unbalance rate (%PVUR) of 1.388%. Harmonic analysis of the induced voltage confirms low harmonic distortion with %THD at 1.528%, as shown in Figure 6.3.

Figure 6.4a gives the voltages measured over a range of speeds while Figure 6.4b gives the voltage constant calculated for each of these points. The aver-

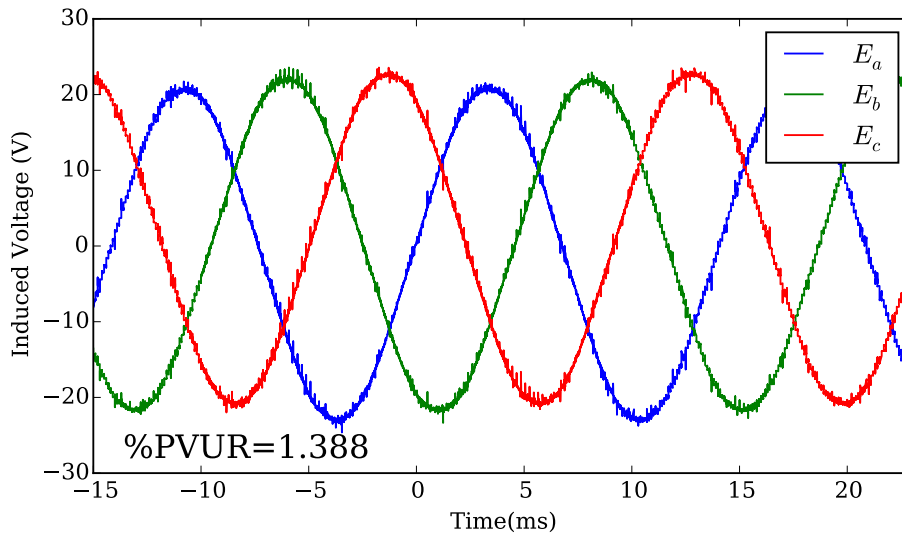


Figure 6.2: Induced voltage measured in OC test.

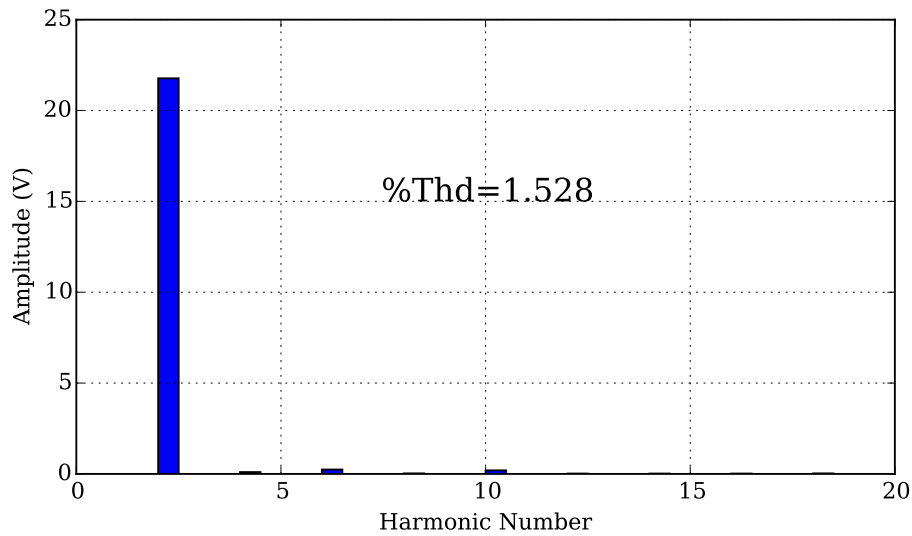
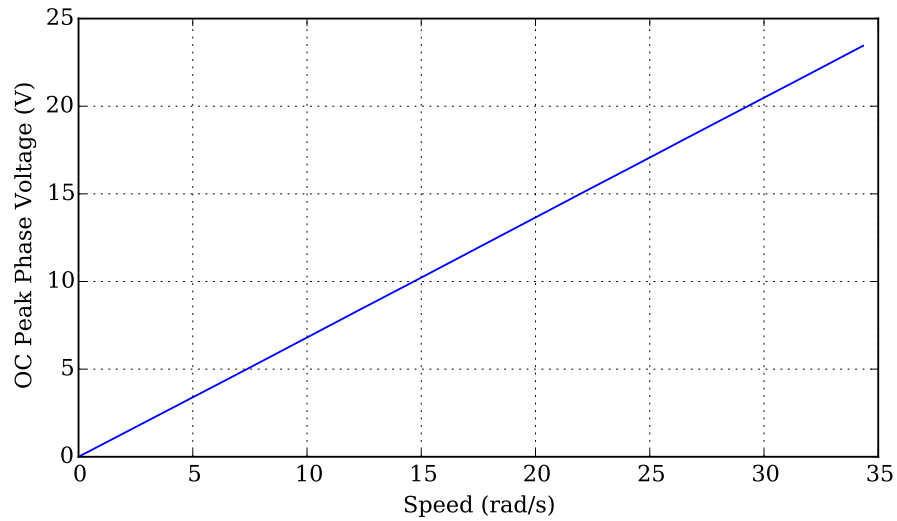


Figure 6.3: Harmonic distortion of induced voltage.

age voltage constant is 0.682, which is very close to the theoretically calculated value of 0.71. This represents less than 4% deviation from design specification, which is an improvement upon the 11% deviation seen in the aluminium prototype.

During the open circuit test, readings from the torque sensor could be used to determine losses from the eddy effect along with friction in the bearings and windage. Even at rated speed, however, these effects registered less than 1 W of power on the torque sensor reading. The ill conceived coils wound with solid 1.6 mm wire provided a rare opportunity to test the real-world effect of





(a) Voltage versus speed.

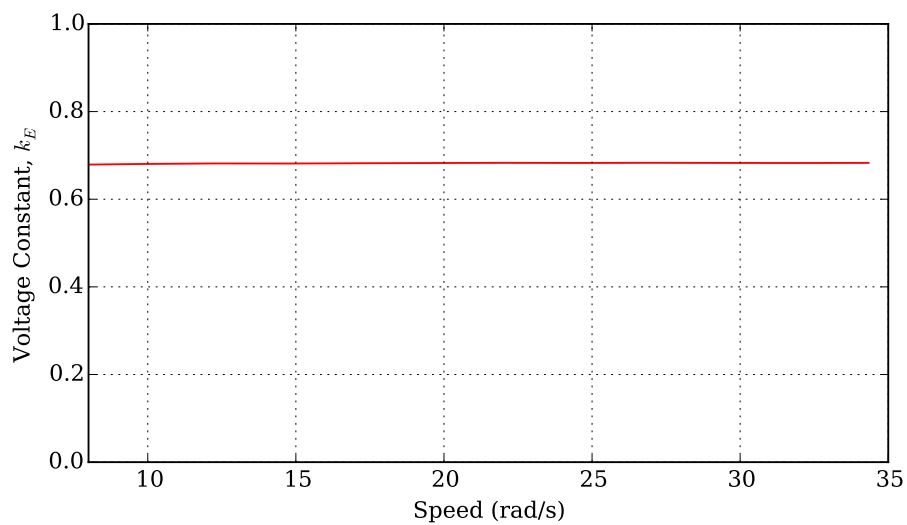
(b) Voltage constant  $k_E$  vs speed.

Figure 6.4: Results from open circuit test.

eddy losses in air cored coils. The Litz wire coils were temporarily replaced with these original coils, depicted in Figure 6.5, and power input measured in open circuit connection. The results are shown in Figure 6.6. Approximately 30 W registered at rated speed, which is far less than the theoretically calculated value, but still much more than would be deemed acceptable for a high-efficiency machine such as this project aims to build.



Figure 6.5: The 1.6 mm coils used to test eddy effects.

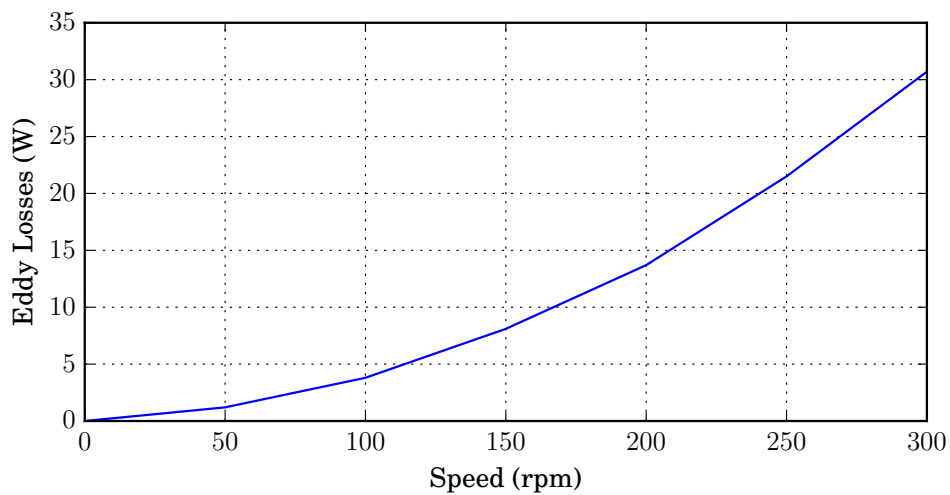


Figure 6.6: Eddy loss measurements.

### 6.1.3 Load Test

During the load test, measurements were taken at specific torque and speed points across the constant torque speed range to create an efficiency contour which could be compared with the theoretical values determined in Chapter 3. At each point, rms phase current and torque were also measured, shown in Figure 6.7. From these measurements, a torque constant could be calculated. The average from all measurements was 0.698.

When calculating efficiency, it was important to bear in mind the direction of power flow during motor operation, shown in Figure 3.16, since this is the

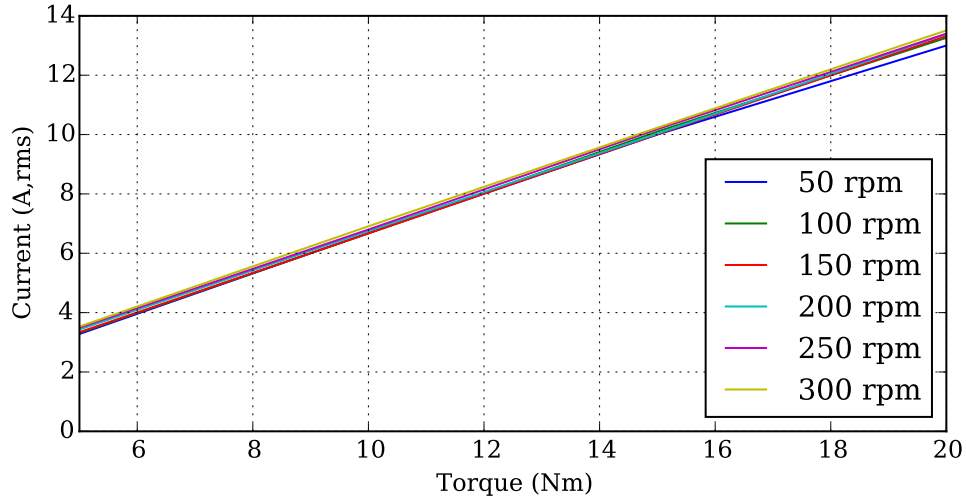


Figure 6.7: Current(rms) vs. torque measurements.

operation mode for which efficiency was calculated in Chapter 3. In keeping with (3.15), efficiency is equated as

$$\eta = \frac{P_m}{P_m + P_{loss}} \quad (6.1)$$

where  $P_m$  is the mechanical shaft power and losses are lumped together in the term  $P_{loss}$  which represents the difference between shaft power and electrical power measured by the *Norma 5000*. Efficiencies measured for a range of points in the constant torque region are plotted in Figure 6.8.

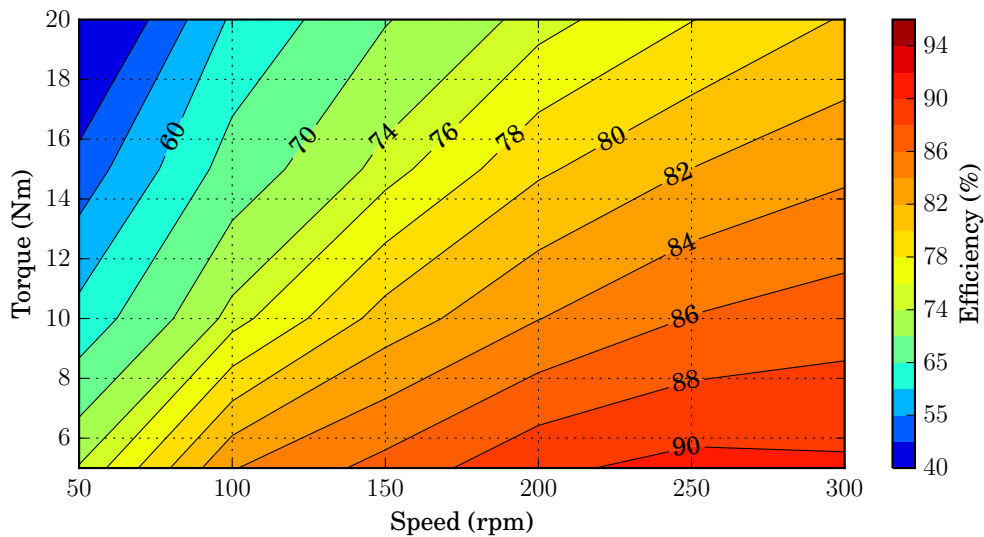


Figure 6.8: Measured efficiency from load test.

To determine whether or not these values reflect an expected result, theoretical efficiency was recalculated for the motor constant of 0.682 and measured phase resistances of  $0.165\ \Omega$  and plotted in Figure 6.9. The recalculated efficiency also accounted for the steady state temperature of approximately  $40^\circ\text{C}$  at which tests were conducted. This temperature will be discussed in greater detail in Section 6.2. The measured efficiency is noticeably lower.

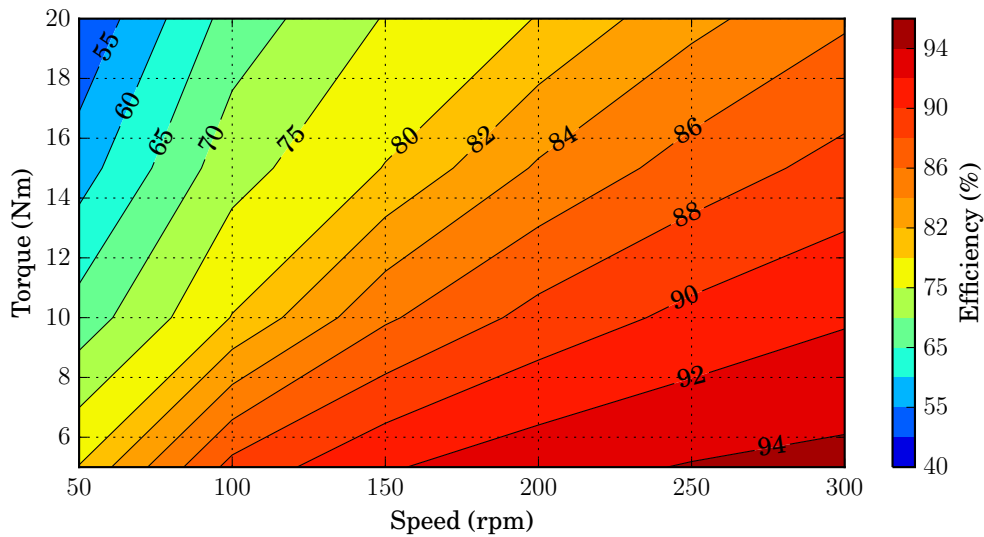


Figure 6.9: Theoretical efficiency corresponding with measured points.

Figure 6.10 shows the difference in percentage efficiency between the measured and theoretical values, all more than 4%. This plot indicates a very counter intuitive trend, suggesting a greater discrepancy at lower speed, and is ultimately not very informative.

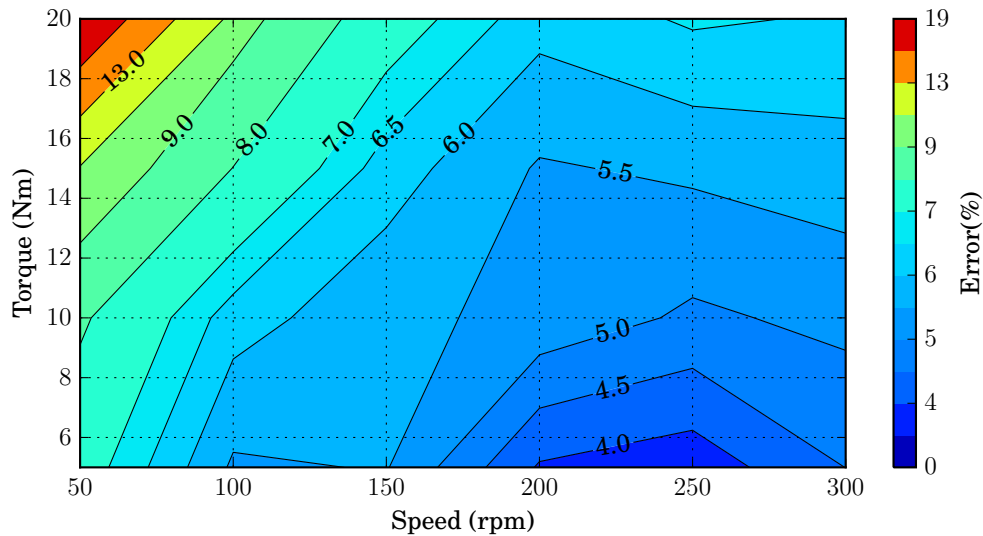


Figure 6.10: Error of measured efficiency: percentage difference.

To better understand the nature of the discrepancy, the difference in power loss for measured and theoretical values for each point was plotted in Figure 6.11. In this plot, higher loss corresponds with higher speed which is consistent with the presence of linear frictional damping in the system. Since frictional and eddy loss at rated speed for the Litz wires registered less than one watt, the only possible explanation is friction on the belt drive connecting the drive shaft to the IDRFP, shown in Figure 6.12. Another noticeable trend is the dramatic increase of losses with higher load, which suggests that the belt flexes under load and causes higher friction due to this deformation.

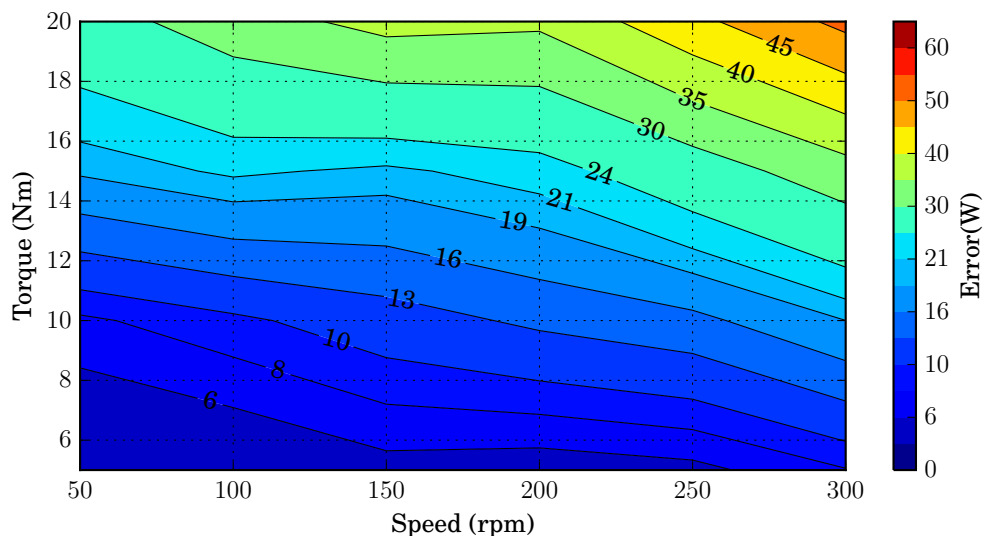


Figure 6.11: Error of measured efficiency: loss power difference.

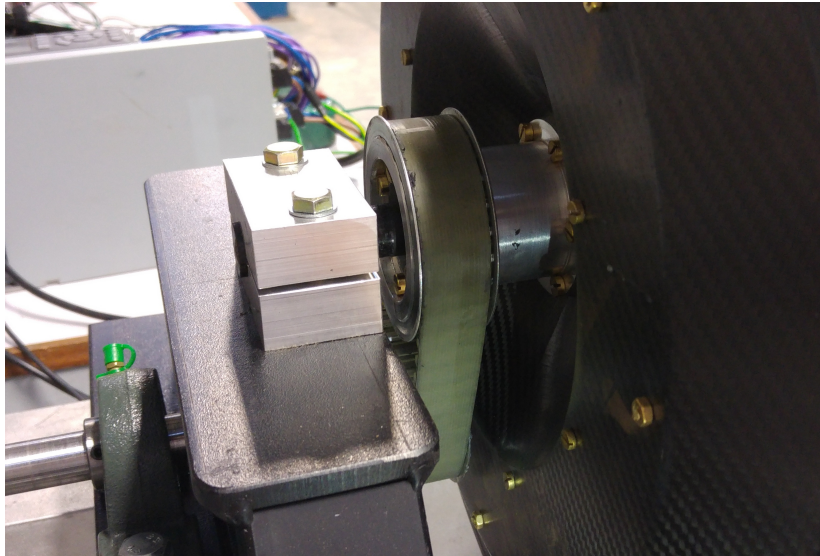


Figure 6.12: Timing belt for the drive motor.

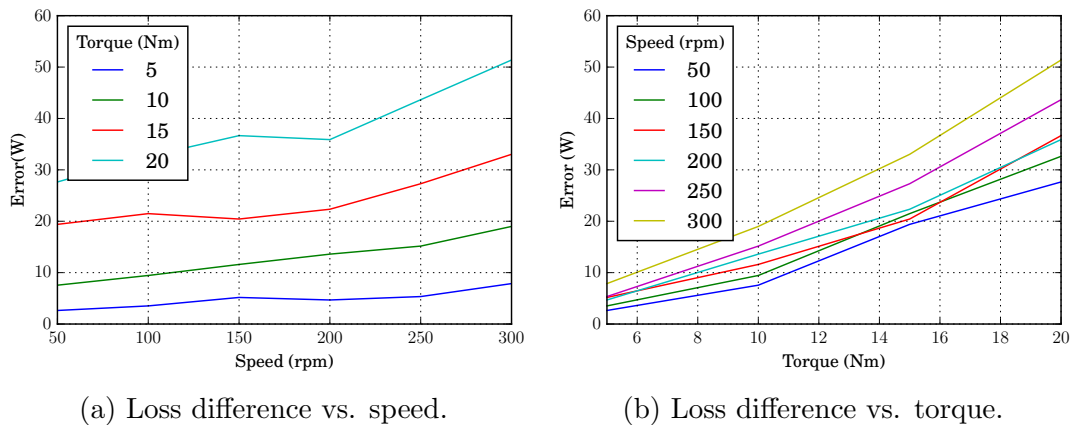


Figure 6.13: Relationships of loss to speed and torque.

The relationship is further clarified by plotting the loss difference separately versus speed and torque, as shown in Figure 6.13. These two plots indicate the discrepancy is much more dependent on torque than on speed, which supports the theory that the belt deforms under load and causes larger friction losses.

## 6.2 Thermal Performance

During load testing, temperature data was recorded using thermistors cast into the coils. These temperatures were verified using a *Fluke* thermal imaging camera.

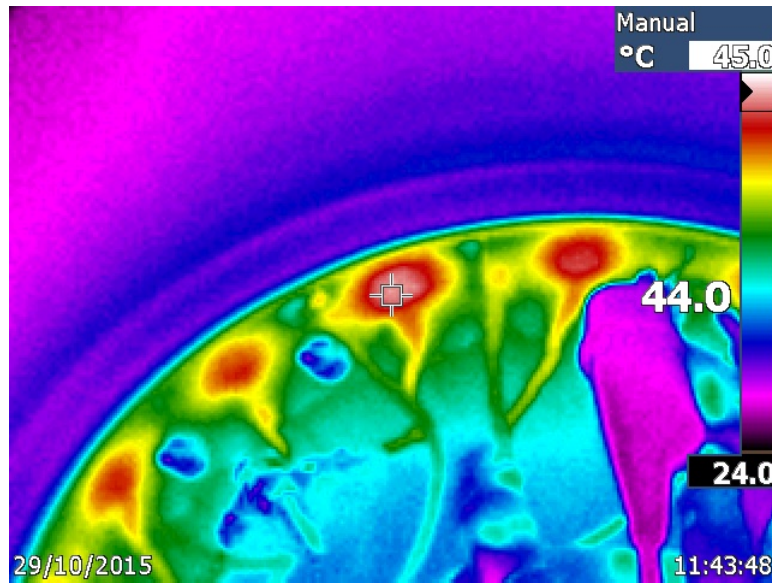


Figure 6.14: Thermal imaging measurement: steady state at  $\hat{I}_a=11$  A.

### 6.2.1 Static Air: No Fan

In Chapter 5, it was estimated that without any forced convection the maximum load the machine could safely sustain is approximately 10 A peak current, corresponding with approximately 10.6 Nm of torque. Thus, the prototype was tested under a slightly heavier load, 11 A peak. The load was sustained for an extended period of time and a steady state temperature of approximately 44°C was recorded, shown in Figure 6.14. This is substantially lower than the theoretically calculated value of over 83°C. A revision of the thermal model is discussed in Chapter 7.

### 6.2.2 Forced Convection: Fan

As a strategy to better dissipate heat, a 3D printed fan was fixed to the exterior of the prototype. As shown in Figure 6.15, the fan was fixed in makeshift fashion to test the concept. If successful, the fan would later be fixed permanently with silicone glue.

Unfortunately, the fan exhibited no distinguishable effect on steady state temperature. This result prompted a separate test with a different source of convection.





Figure 6.15: Fan fixed to prototype.

### 6.2.3 Forced Convection: Pressurized Air Supply

The fan's poor performance could have been a result of its makeshift mounting tape not offering a proper seal to facilitate better air flow. However, it could also have been an indication that the forced convection concept is flawed in general. To test this, a separate source of convective flow had to be devised. To this end, all but one of the holes drilled on the stator as inlets were covered. The last hole was provided with a pipe connected to the pressurized air supply in the workshop. This setup is pictured in Figure 6.16.

Unlike the fan, this setup had a noticeable effect, lowering steady state temperature to 41°C. Still, the effect is much smaller than anticipated. It is likely that the air gap is smaller than the design value and that a higher pressure differential between the inside and outside of the machine is required to create a sustained air flow fast enough to have significant effect on the machine temperature.

### 6.2.4 Full Load

The previous load tests had given positive results, indicating the nominal load of 10 A peak could be sustained indefinitely. However, the maximum rating is 20 A peak. This load was applied after the machine had reached steady state temperature under nominal load. After approximately five minutes, temperature measured by the thermistors and thermal imaging camera reached approximately 55°C. At this point, scraping from inside the machine occurred





Figure 6.16: Pressurized air supply setup.

and became audible. This indicated that thermal expansion, most likely in the stator structure, caused interferences between the rotor and stator. Since the temperature showed no sign of stabilizing, the test was stopped.

This result indicates that the IDRFPM can safely sustain full load but for a limited time. While interference occurred after 5 minutes, the rating will be capped at 2 minutes.

## 6.3 Structural Performance

### 6.3.1 Stator

At first, the stator plate was fixed to its shaft with Araldite glue, which is used to glue magnets and was also used as a step in the assembly process for the magnet arrays in the IDRFPM prototype. However, during load testing this bond failed. As an improvement, layers of carbon fibre were placed over the faces adjacent to the interface between the plate and shaft. These layers were fixed in a wet-layup method by first roughening the surfaces on which they would be placed, then soaking them in resin and applying them to the structure. The result is pictured in Figure 6.17.

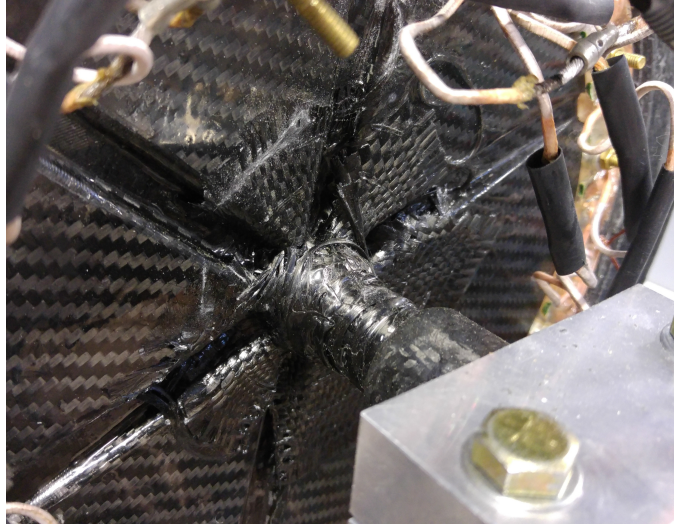


Figure 6.17: Reinforced stator shaft interface.

Even after the reinforcement, the stator showed noticeable deformation at higher loads during testing. A gauge was mounted to measure displacement in the tangential direction on the nominal radius, as shown in Figure 6.18. The gauge measured 2.15 mm of deformation, which is large compared to the 0.3 mm estimated by FEM simulations in Chapter 4.

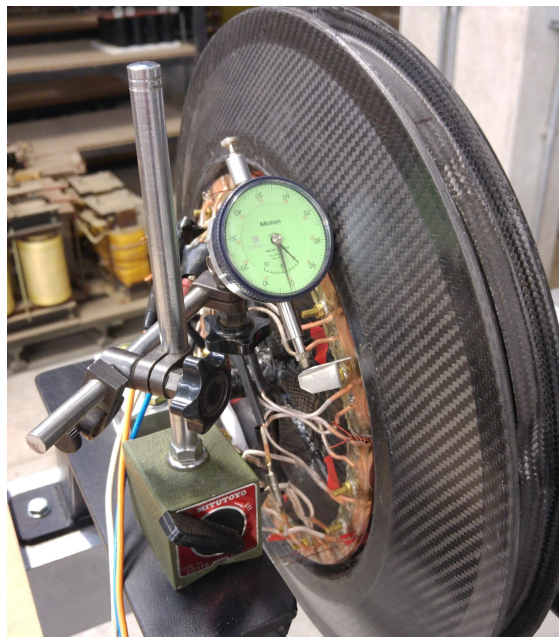


Figure 6.18: Testing deflection of the stator.

### 6.3.2 Rotor

A separate setup was used to test deflection of the rotor. The lateral force experienced during cornering of the vehicle could be simulated by positioning the rotor on its side and hanging a weight from one end, as pictured in Figure 6.19. An accurate measurement was made by placing a gauge on the shaft which held the rotor, such that deflection of the shaft itself would not be measured but only deflection of the rotor relative to the shaft.



Figure 6.19: Testing deflection of the rotor under lateral load.

As mentioned in Chapter 4, the lateral force applied in the structural FEM simulations was 280 N, corresponding with approximately 28.5 kg. It was mentioned that this force is much larger than the force the wheel would experience in reality since the force would be divided between the front and rear wheels. Given that structural testing was not intended to harm the prototype, weight was added until the measured deflection matched the simulated deflection. With approximately 15 kg hanging from its edge, the maximum displacement measured by the gauge was 1.6 mm.

Deflection is thus much higher than what the FEM results suggested. However, the motor should experience much less than the 280 Nm force used in the

FEM results. As mentioned in Appendix B, the 280 Nm force will be split between the front and rear wheels by a ratio depending on the centre of gravity once the driver is seated in the vehicle.

## 6.4 Tested Performance Summary

Key test results and measurements are summarized in Table 6.1.

Table 6.1: Summary of torque density information.

<b>Phase Resistance</b>	0.165 $\Omega$	<b>Nominal torque (7.07 <math>A_{rms}</math>)</b>	11 Nm
<b>Phase Inductance</b>	102 $\mu\text{H}$	<b>Efficiency at nom. torque &amp; speed</b>	86.7%
<b>Voltage Constant</b>	0.682	<b>Temperature at nom. torque</b>	44°C
<b>Torque Constant</b>	0.698	<b>Max torque (14.14 <math>A_{rms}</math>)</b>	21 Nm
<b>Nominal speed</b>	290 rpm	<b>Efficiency at max. torque &amp; speed</b>	79.7%
<b>Max. lateral load</b>	15 kg	<b>Max. time at max. torque</b>	2 min
<b>Poles</b>	28	<b>Coils</b>	21
<b>Structural mass</b>	6.1 kg	<b>Active mass</b>	3.57 kg



# Chapter 7

## Conclusions & Recommendations

This thesis presents the design process that created an IDRFPM prototype with predominantly CFRP frame structure. The design process included a revision of the electromagnetic topology, which succeeded in improving performance from previous designs by moving the inter-pole magnets to an in-line position creating a segmented quasi-Halbach array. The mechanical design succeeded in reducing the percentage of structural mass compared to the aluminium prototype and in turn the overall torque density. Thermal analysis was less successful, with test results indicating a vast discrepancy between measured and theoretical results. However, the methods presented in this thesis are a useful tool and were adjusted to more closely match results, as discussed later in this chapter. The prototype produced is capable of fulfilling its role as a propulsion unit for a SEM vehicle and represents a significant overall improvement over the first IDRFPM prototype. The following sections offer a number of key observations and recommendations for future IDRFPM prototypes.

### 7.1 Electromagnetic Design

Full numerical optimization of the electromagnetic design was not considered an objective of this project, however this is the next step for work on the IDRFPM. It should be noted that a number of practical and logistical aspects ultimately influenced specific design variables in the CFRP prototype. Also, there are a number of variables that were fixed to arbitrary design specifications and were not further investigated. A few variables in particular warrant attention.

### 7.1.1 Pole Count

Retrospective investigation of the IDRFBM prototype's electromagnetic specifications indicated that a 34-pole machine would have yielded an approximate 15% torque increase. Granted that the change in poles would require the coils to be redesigned also, this could still have constituted a net benefit.

### 7.1.2 Coil Turns & Fill Factor

The number of coil turns and the fill factor ultimately achieved by this machine were greatly influenced by the sudden switch to Litz wire. The wire used had to be chosen from a list of readily available wires since a custom wire required a large minimum order quantity.

### 7.1.3 Coil & Magnet Thickness

While stack length and outer diameter are generally fixed to physical limitations, inner diameter and thus nominal radius may be varied to meet an optimum between coil mass and magnet mass. This relationship was not explored in depth.

### 7.1.4 Magnet Grade

Very little attention was paid to magnet grade throughout the design of this machine. For future prototypes it will be important to take into account even stronger magnet grades and, more importantly, grades specifically developed with higher demagnetization temperatures. The CFRP prototype uses N48 magnets, while the highest grade currently available is N52. There is also a NEH grade specification available with a maximum operating temperature of 200°C. While these higher grades are likely very expensive, Stegmann [24] concluded that maximizing magnet grade minimizes machine size at marginal cost. A different thermal designation will also increase the critical temperature of the machine and improve maximum performance capability.

## 7.2 Design for Manufacture

While the finished product is fully functional and achieves adequate performance, much was learned from the manufacturing process that can create

better machines more easily in the future. A few key factors could greatly simplify manufacture of future prototypes.

### 7.2.1 Materials and Machining Operations

CFRP proved to be a very difficult material to work with. Still, the problems encountered during manufacture are likely to manifest regardless of the material used. Any components formed by a molding process must be designed with a machining step on critical surfaces preemptively included in the manufacture process. Creating a well balanced machine with minimal runout oscillations requires strategic use of lathe machining, which can be facilitated from the onset of the design process. The designer can add shoulders or surfaces specifically for the purpose of positioning a part onto a lathe, or alternatively design tool components which attach to the part allowing it to be gripped by a lathe.

Throughout the assembly process of the final prototype, machining of larger CFRP components evoked concerns over the potential of individual fibres tearing out during lathe operations and causing catastrophic failure. Ultimately the risk was taken and rewarded with successful control of tolerances on key surfaces. However, care must be taken to consult experts in the field of composites when planning machining procedures and to point out the potential for such failures to any workshop personnel that will handle the CFRP components.

### 7.2.2 Magnet Assembly

The single most time consuming manufacturing challenge was the assembly of the magnet arrays. The segmented quasi-Halbach magnet array is particularly difficult to realize in practice because of the forces driving the magnets away from each other, as discussed in Chapter 4. Layers of CFRP proved to be strong enough to constrain the magnets, but it was very difficult to keep the magnets in place long enough for the layers to be properly placed before they broke free from the glue that temporarily held them in place. This was partially due to the cumbersome gluing process which suffered from spacing of the magnets. A very small discrepancy in diameter of the surface on which the magnets were to be applied resulted in spacing discrepancies that would either cause a substantial gap between the last two magnets applied or, conversely, leave a gap too narrow for the last magnet.

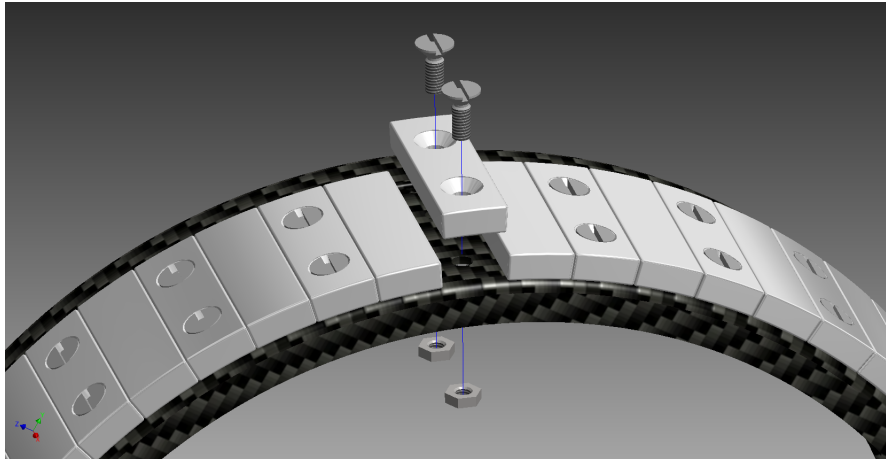


Figure 7.1: Magnets fixed with screws.

There are many possible solutions to the problem of fixing magnets in place, but the simplest by far is to place holes through the center of the magnets and drill corresponding holes in the rotor such that the magnets are fixed to the rotor with screws. As suggested in Figure 7.1, it is possible that the screws would only be necessary for every second magnet. For the inner set of magnets, the inter-pole magnets must be screwed to the rotor because they will push away from the surface while the pole magnets will be pushed toward the surface, which can be deduced from Figure 4.6. The outer set of magnets will experience a reciprocal scenario, meaning the pole magnets have to be screwed to the outer rotor instead. It is still likely that the magnets will pull out of position once the inner and outer sets are brought near each other, especially during operation. Thus it is still necessary to place a layer of CFRP over the screwed magnets.

An important prerequisite for improving magnet assembly is to refine the tolerances of the rotor frame components. As a further precaution, magnets could be made narrower to allow for spacers that could manually be adjusted to accommodate discrepancies. However, this would sacrifice magnet material and thus performance.



## 7.3 Thermal Design and Analysis

### 7.3.1 Revision of Analysis

The results from the thermal resistance diagram analysis proved to be very inaccurate. However, the author maintains that this is a viable method of analysis, simply requiring refinement of certain variables in the model. The resistance network proposed in Chapter 5 is a conservative simplification of the true scenario occurring in the machine. A number of variables were adjusted to account for some of these simplifications. Total surface area of the coils can be made larger to account for heat transfer through the resin structure, whereas the original model assumed perfect insulation on the side surfaces. Area of radial surfaces can also be increased since the original estimates did not include all side surfaces that can also dissipate heat. A term was also added for heat transfer away from the coils on the side surface exposed directly to ambient air, assuming a convection coefficient due to the rotation of the rotor in close proximity. This surface was previously also assumed to be insulated by the resin, but the thermal imaging camera indicated otherwise. A final adjustment was to lower the ambient temperature to better reflect the temperature in the lab where the machine was tested.

Temperature of the magnet surface was also reduced until total heat dissipation from the copper reflected the value dissipated by the machine during the load test at nominal operating point. The revised calculations give a copper temperature of 49°C while dissipating the amount of heat energy created by resistive loss at the nominal operating point. This is still higher than the measured value of 41°C but much closer than the original approximation of 83°C.

### 7.3.2 Cooling Strategy

What became clear from the test results is that a high pressure differential is required to create the necessary flow rate in the air gap for the desired improvement in heat dissipation. This pressure differential would most likely require too much energy to create to have a positive net effect on the overall system efficiency for a machine in this power range. Liquid cooling remains an unattractive option, if only due to the difficulty of creating a properly sealed system that still exhibits the necessary heat transfer characteristics without

utilizing conductive components affected by the moving magnetic fields present in the stator.

However, the revision of the theoretical analysis suggests that an opportunity exists in the form of the side of the coils exposed to open air. If a heat sink could be designed to come in close contact with the end windings exposed on the side, net heat transfer could significantly be increased.

## 7.4 Wind Application

Having created a functional prototype with improved performance, the IDRFP design can be applied to the wind power generation application for which it was originally intended. A factor which was not taken into consideration in this thesis was cost of materials, which must be taken into account when optimizing the topology. The topology comparison in Chapter 3 confirmed the ironless design was the lightest, but not necessarily the cheapest. It is possible that the best cost benefit lies with a hybrid design. The result of such an optimization is likely to decide the viability of the IDRFP for most applications.

The lightweight frame components created for the CFRP prototype have proven the versatility of the material and make it an attractive option for wind turbine designs as well and many turbine blade manufacturers already choose carbon fibre. Whether VAWTs or HAWTs are pursued for future prototypes will depend on the opportunities for application of the IDRFP design that arise. In either case, a suggestion has been made to create an integrated design such that the machine frame is directly integrated with the blade mounts in a single, flowing piece.

# Appendix A

## Calculation of Inductance

Inductance was calculated by first using ANSYS Maxwell<sup>®</sup> FEM software to calculate self and mutual inductions for one phase, taking into account only the coils and omitting the magnets. For this case, the relationship between inductances, flux linkages and current for each phase can be described as follows:

$$\begin{bmatrix} \lambda_a \\ \lambda_b \\ \lambda_c \end{bmatrix} = \begin{bmatrix} L_{aa} & L_{ab} & L_{ac} \\ L_{ba} & L_{bb} & L_{bc} \\ L_{ca} & L_{cb} & L_{cc} \end{bmatrix} \begin{bmatrix} i_a \\ i_b \\ i_c \end{bmatrix} \quad (\text{A.1})$$

Using inductances calculated by FEM software for the final design specification, we have

$$L_{aa} = L_{bb} = L_{cc} = 74.01\mu\text{H} \quad (\text{A.2})$$

and

$$L_{ab} = L_{ba} = L_{ac} = L_{ca} = L_{cb} = L_{bc} = -21.06\mu\text{H} \quad (\text{A.3})$$

For a single phase it follows that

$$\lambda_a = L_{aa}i_a + L_{ab}i_b + L_{ac}i_c \quad (\text{A.4})$$

and assuming a balanced three-phase system we have

$$i_a + i_b + i_c = 0 \quad (\text{A.5})$$

$$\therefore i_a = -(i_b + i_c) \quad (\text{A.6})$$

Substituting (A.3) and (A.6) into (A.4) and rewrite it as

$$\lambda_a = (L_{aa} - L_{ab})i_a \quad (\text{A.7})$$

which implies that synchronous inductance is simply the difference between self and mutual inductance. This equates to

$$L_s = L_{aa} - L_{ab} \quad (\text{A.8})$$

$$= 95.07\mu\text{H} \quad (\text{A.9})$$

The end windings are not taken into account in these equations. Calculation of end windings was shown to be a convoluted process in [26, p.77] and accurate calculation of inductances was not a critical concern for the primary project objectives. Measured inductance in Chapter 6 indicated that the above calculated value was very close to accurate.

## Appendix B

### Lateral Cornering Force

To perform structural analysis in Section 4.5, it was necessary to determine the forces acting on the machine during its most threatening load case: a turn on the race track at speed. Figure B.1 indicates the direction of the velocity  $V$  about the centre  $C$  on a radius  $R$ . This results in the lateral or centripetal force  $F_l$  acting on the centre of mass  $m$ , assumed to be between the front and rear wheels.

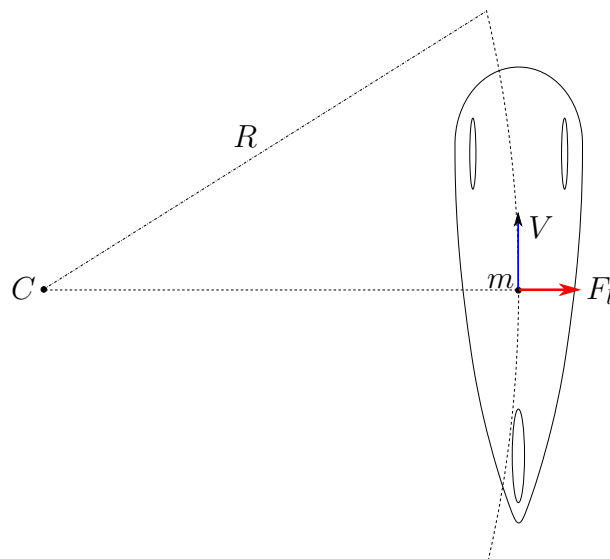


Figure B.1: Centripetal force due to cornering.

Using the symbols from Figure B.1, centripetal force for an object traveling on a circular path is equated by

$$F = m \frac{V^2}{R} \quad (\text{B.1})$$

For a vehicle mass of 85 kg, minimum turn radius of 8 m and maximum velocity of 7.5 m/s (27 kph), the centripetal force is approximately 600 N. Given that the vehicle mass itself only creates about 830 N of downward force, it is clear the car is likely to tip before achieving 600 N of centripetal force. Figure B.2 more closely examines the vehicle dimension in order to determine the tipping force.

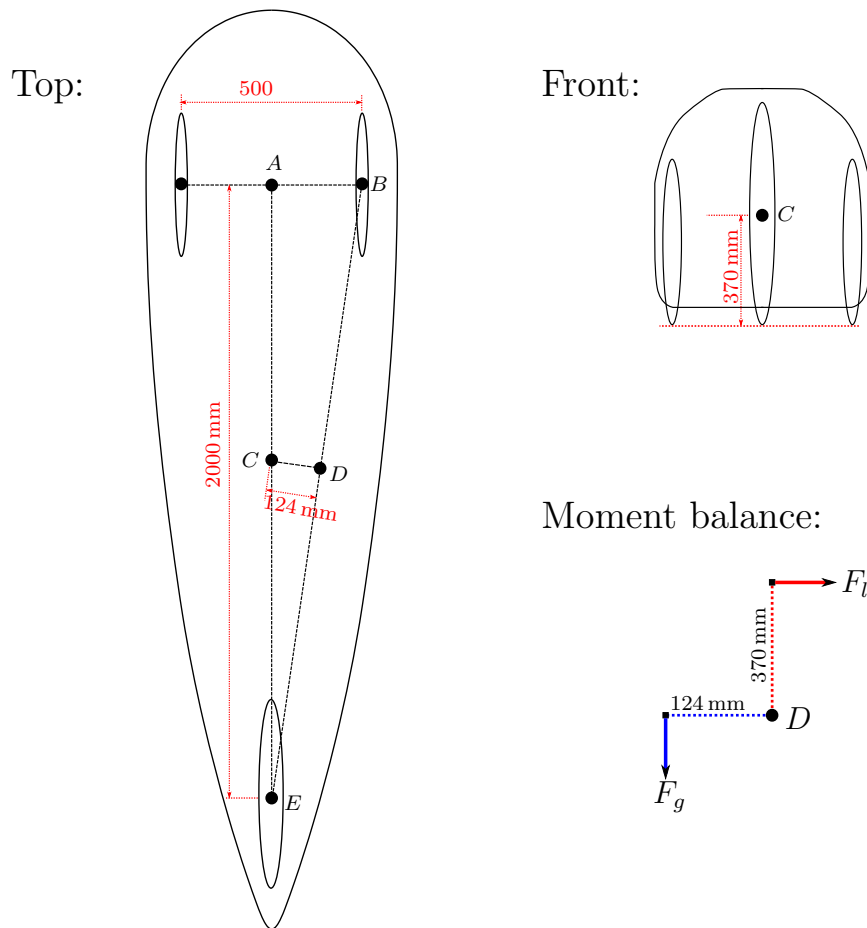


Figure B.2: Schematic of moment balance for tipping force.

With gravitational force  $F_g$  known to be 830 N and the distances indicated in Figure B.2, the moment balance about point D can be expressed as

$$830 \cdot 0.124 - F_l \cdot 0.370 = 0 \quad (\text{B.2})$$

Solving for lateral force  $F_l$  gives a value of approximately 280 N. As is noted in Section 4.5, this force is taken to be the lateral force acting solely on the

machine, even though it will be split between the front and rear wheels of the vehicle. This assumption ensures a conservative estimate since the centre of gravity used in these calculations is a geometric approximation. Determining an actual and exact centre of gravity is impossible at the time of this writing.

# Appendix C

## Thermal Calculations

### C.1 Initial Calculations



## Static air condition:

### Key dimensions:

Nominal radius:  $r := 120 \text{ mm}$

Total axial length:  $l := 80 \text{ mm}$

Area of top and bottom surfaces of copper:

$$A_{\text{cu}} := 0.00118 \cdot 21.2 \text{ m}^2 = 0.0496 \text{ m}^2$$

Side area of copper:

$$A_{\text{cuB}} := 15.7 \cdot 9 \cdot 21 \text{ mm}^2 = 0.003 \text{ m}^2$$

Mean surface area for all radial surfaces:

$$A_{\text{std}} := \pi \cdot 2 \cdot r \cdot l = 0.0603 \text{ m}^2$$

Surface areas of CF and AL for side

$$A_{\text{al}} := \pi \cdot (124.5^2 - 115.5^2) \text{ mm}^2 = 0.0068 \text{ m}^2$$

$$A_{\text{cfs}} := \pi \cdot (126^2 - 114^2) \text{ mm}^2 = 0.009 \text{ m}^2$$

### Predefined Temperatures:

$$T_{\text{CF1}} := 75.0 \text{ }^\circ\text{C} \quad T_{\text{ambient}} := 25 \text{ }^\circ\text{C}$$

We must first specify a copper temperature to calculate total heat transfer. Then, magnet CF temperature can be calculated. Copper temperature can be manually adjusted to determine the limit.

### Thermal Resistances:

Static air conduction:

$$R_{\text{gapStat}} := \frac{1 \text{ mm}}{k_{\text{air}} \cdot A_{\text{cu}}} = 0.7761 \frac{\text{K}}{\text{W}}$$

CF layer on magnets:

$$R_{\text{CF1}} := \frac{0.5 \text{ mm}}{k_{\text{cf}} \cdot A_{\text{std}}} = 0.0166 \frac{\text{K}}{\text{W}}$$

CF frame behind magnets:

$$R_{\text{CF2}} := \frac{2 \text{ mm}}{k_{\text{cf}} \cdot A_{\text{std}}} = 0.0663 \frac{\text{K}}{\text{W}}$$

### Thermal conductivities:

$$k_{\text{mag}} := 7 \frac{\text{W}}{\text{m K}}$$

$$k_{\text{air}} := 0.026 \frac{\text{W}}{\text{m K}}$$

$$k_{\text{cf}} := 0.5 \frac{\text{W}}{\text{m K}}$$

$$k_{\text{al}} := 205 \frac{\text{W}}{\text{m K}}$$

$$k_{\text{cfP}} := 6 \frac{\text{W}}{\text{m K}}$$

### Epoxy resin emissivity:

$$\varepsilon_{\text{resin}} := 0.95$$

Magnet:

$$R_{\text{mag}} := \frac{5.5 \text{ mm}}{k_{\text{mag}} \cdot A_{\text{std}}} = 0.013 \frac{\text{K}}{\text{W}}$$

In-plane resistance of frame:

$$R_{\text{CF2S}} := \frac{\ln\left(\frac{0.195}{0.1315}\right)}{2 \cdot \pi \cdot k_{\text{cfP}} \cdot 0.005 \text{ m}} = 2.0902 \frac{\text{K}}{\text{W}}$$

Air cavity between frame layers:

$$R_{\text{air2}} := \frac{30 \text{ mm}}{k_{\text{air}} \cdot A_{\text{std}}} = 19.1292 \frac{\text{K}}{\text{W}}$$

The outer and innermost frame components exposed to air are equated as carbon fibre layers twice the thickness of the other frame layers:

$$R_{\text{CF3}} := 2 \cdot R_{\text{CF2}} = 0.1326 \frac{\text{K}}{\text{W}}$$

Aluminium ring:

$$R_{\text{al}} := \frac{2.5 \text{ mm}}{k_{\text{al}} \cdot A_{\text{al}}} = 0.0018 \frac{\text{K}}{\text{W}}$$

Radiation:

$$R_{\text{rad1}} := \frac{1}{9.43 \cdot \epsilon_{\text{resin}} \cdot A_{\text{std}}} \frac{\text{m}^2 \text{K}}{\text{W}} = 1.8506 \frac{\text{K}}{\text{W}}$$

$$R_{\text{rad2}} := \frac{1}{9.43 \cdot \epsilon_{\text{resin}} \cdot A_{\text{al}}} \frac{\text{m}^2 \text{K}}{\text{W}} = 16.4498 \frac{\text{K}}{\text{W}}$$

For the static air condition we have enough information to consolidate all thermal resistances and solve for the critical temperature of the CF layer around the magnets in one step. We first determine the maximum heat transfer possible between the CF surface and ambient air.

Radial direction:

*Air cavity and in-plane:*

$$R_{\text{midEq}} := \frac{1}{\frac{1}{R_{\text{air2}}} + \frac{1}{R_{\text{CF2S}}}} = 1.8843 \frac{\text{K}}{\text{W}}$$

Total from CF to ambient:

$$R_{\text{CF\_amb}} := R_{\text{midEq}} + R_{\text{CF1}} + R_{\text{CF2}} + R_{\text{mag}} + R_{\text{convOut}} = 3.3618 \frac{\text{K}}{\text{W}}$$

$$Q'_{\text{CF\_amb}} := \frac{T_{\text{CF1}} - T_{\text{ambient}}}{R_{\text{CF\_amb}}} = 14.8731 \text{ W}$$

Side air gap conduction:

$$R_{\text{gapS}} := \frac{1 \text{ mm}}{k_{\text{air}} \cdot A_{\text{al}}} = 5.6679 \frac{\text{K}}{\text{W}}$$

Side CF frame:

$$R_{\text{cfS}} := \frac{2.5 \text{ mm}}{k_{\text{cf}} \cdot A_{\text{cfs}}} = 0.5526 \frac{\text{K}}{\text{W}}$$

External convection: We assume a typical coefficient of convection for the air moving over the outer surface as the rotor turns.

$$R_{\text{convOut}} := \frac{1}{80 \frac{\text{W}}{\text{m}^2 \text{K}} \cdot A_{\text{cfs}}} = 1.3816 \frac{\text{K}}{\text{W}}$$

With this information, we can calculate the corresponding copper temperature. First, we need to calculate the combined thermal resistance for conduction and radiation.

$$R_{\text{gapEq}} := \frac{1}{\frac{1}{R_{\text{gapStat}}} + \frac{1}{R_{\text{rad1}}}} = 0.5468 \frac{K}{W}$$

$$T_{\text{cu}} := T_{\text{CF1}} + Q'_{\text{CF\_amb}} \cdot R_{\text{gapEq}} = 83.1322 \text{ } ^\circ\text{C}$$

With this temperature, we can also calculate the heat dissipated through the side of the machine. Again, we start by calculating the equivalent resistance for this section.

*Radiation and air conduction:*

$$R_{\text{gapEqS}} := \frac{1}{\frac{1}{R_{\text{gapS}}} + \frac{1}{R_{\text{rad2}}}} = 4.2154 \frac{K}{W}$$

*Combined resistances:*

$$R_{\text{side}} := R_{\text{al}} + R_{\text{gapEqS}} + R_{\text{cfS}} + R_{\text{convOut}} = 6.1514 \frac{K}{s \cdot A^2}$$

$$Q'_{\text{side}} := \frac{T_{\text{cu}} - T_{\text{ambient}}}{R_{\text{side}}} = 9.4502 \text{ W}$$

This gives us the total heat dissipation for the critical magnet temperature for the static air case:

$$Q'_{\text{CF\_amb}} + Q'_{\text{side}} = 24.3233 \text{ W}$$

The total heat dissipation corresponds with the expected copper loss for a little more than 10A peak current, which would deliver 10.7 Nm of torque according to Maxwell simulations.

## Forced Convection Condition:

The thermal resistances calculated for the static condition remain the same. The first step in calculating critical temperatures for convection is determining the convection coefficient. A velocity is assumed for the flow of air through the air gap. The air gap is equated as an annulus between pipes. Length is equal to twice the active length of the machine to account for both air gaps, taken at a mean radius.

Assume average velocity:

$$v_{\text{avg}} := 0.5 \frac{\text{m}}{\text{s}} \quad \begin{array}{l} \text{Results included} \\ \text{for other flow rates} \\ \text{at end of calculations.} \end{array}$$

Channel area:

$$A_c := \pi \cdot (120.5^2 - 119.5^2) \text{ mm}^2 = 753.9822 \text{ mm}^2$$

Air properties @ 50°C:

$$\rho_{\text{air}} := 1.092 \frac{\text{kg}}{\text{m}^3} \quad \mu_{\text{air}} := 1.963 \cdot 10^{-5} \frac{\text{kg}}{\text{m s}}$$

Hydraulic diameter is Do-Di:

$$D_h := 2 \text{ mm}$$

$$c_{\text{pair}} := 1007 \frac{\text{J}}{\text{kg K}} \quad \text{Pr}_{\text{air}} := 0.7228$$

Stefan-Boltzmann Constant:

$$k_{\text{air70}} := 0.02881 \frac{\text{W}}{\text{m K}}$$

$$\sigma := 5.67 \cdot 10^{-8} \frac{\text{W}}{\text{m}^2 \text{ K}^4}$$

Volume and mass flowrate:

$$V' := v_{\text{avg}} \cdot A_c = 0.0004 \frac{\text{m}^3}{\text{s}}$$

$$m' := V' \cdot \rho_{\text{air}} = 0.0004 \frac{\text{kg}}{\text{s}}$$

Reynolds number:

$$\text{Re} := \frac{\rho_{\text{air}} \cdot v_{\text{avg}} \cdot D_h}{\mu_{\text{air}}} = 55.6291$$

Flow is laminar. For fully developed laminar flow in annulus, Nusselt number is:

$$\text{Nu} := 4.86$$

Thus we have convection coefficient:

$$h_{\text{airgap}} := \frac{\text{Nu} \cdot k_{\text{air70}}}{D_h} = 70.0083 \frac{\text{W}}{\text{m}^2 \text{ K}}$$

Now that we have this coefficient, we can calculate the thermal resistances for convection of the air gap regions.

$$R_{h\_cfr} := \frac{1}{h_{\text{airgap}} \cdot A_{\text{std}}} = 0.2368 \frac{\text{K}}{\text{W}}$$

$$R_{h\_cfs} := \frac{1}{h_{\text{airgap}} \cdot A_{\text{cfs}}} = 1.5787 \frac{\text{K F}}{\text{s A}^2}$$

$$R_{h\_cu} := \frac{1}{h_{\text{airgap}} \cdot (A_{\text{cu}} + A_{\text{al}})} = 0.2535 \frac{\text{K}}{\text{W}}$$

108

To simplify the notation, we define a few key resistances:

$$R_{eq_r} := R_{CF\_amb} = 3.3618 \frac{K}{W}$$

$$R_m := \frac{1}{m' \cdot c_{pair}} = 2.4122 \frac{K}{W}$$

$$R_{eq_s} := R_{cfS} + R_{convOut} = 1.9342 \frac{K}{W}$$

From energy balances for the air gap control volume, radial CF surface, and side CF surface, we have the following three equations:

- 1)  $Q'_{air} := Q'_{h\_cu} + Q'_{h\_cfr} + Q'_{h\_cfs}$
- 2)  $Q'_{rad_r} := Q'_{cond_r} + Q'_{h\_cfr}$
- 3)  $Q'_{rad_s} := Q'_{cond_s} + Q'_{h\_cfs}$

Heat transfer equations for all types of transfer can be written in the following form:

$$Q' = \frac{T_1 - T_2}{R_{12}}$$

This means we have a system of three equations which we can solve using matrices. With knowledge of the thermal resistance for each form of heat transfer, we can separate known and unknown variables and populate the matrices as follows:

$$a_{11} := \left( \frac{2}{R_m} + \frac{1}{R_{h\_cu}} + \frac{1}{R_{h\_cfr}} + \frac{1}{R_{h\_cfs}} \right) = 9.63 \frac{W}{K}$$

$$a_{12} := \left( -\frac{1}{R_{h\_cu}} \right) = -3.9447 \frac{W}{K}$$

$$a_{13} := -\frac{1}{R_{h\_cfs}} = -0.6334 \frac{W}{K}$$

$$a_{21} := \frac{1}{R_{h\_cfr}} = 4.2228 \frac{W}{K}$$

$$a_{22} := \frac{1}{R_{rad1}} = 0.5404 \frac{W}{K}$$

$$a_{23} := 0$$

$$a_{31} := \frac{1}{R_{h\_cfs}} = 0.6334 \frac{W}{K}$$

$$a_{32} := \frac{1}{R_{rad2}} = 0.0608 \frac{W}{K}$$

$$a_{33} := -\left( \frac{1}{R_{rad2}} + \frac{1}{R_{h\_cfs}} + \frac{1}{R_{eq_s}} \right) = -1.2112 \frac{W}{K}$$

$$b_1 := \left( \frac{2}{R_m} \cdot T_{ambient} + \frac{T_{CF1}}{R_{h\_cfr}} \right) = 1717.368 W$$

$$b_2 := \left( T_{CF1} \left( \frac{1}{R_{rad1}} + \frac{1}{R_{h\_cfr}} + \frac{1}{R_{eq_r}} \right) - \frac{T_{ambient}}{R_{eq_r}} \right) = 1673.169 W$$

$$b_3 := \frac{-T_{ambient}}{R_{eq_s}} = -154.1484 W$$

$$A := \begin{pmatrix} a_{11} & a_{12} & a_{13} \\ a_{21} & a_{22} & a_{23} \\ a_{31} & a_{32} & a_{33} \end{pmatrix} = \begin{pmatrix} 9.63 \frac{\text{kg m}^2}{\text{s}^3 \text{K}} & -3.9447 \frac{\text{kg m}^2}{\text{K s}^3} & -0.6334 \frac{\text{kg m}^2}{\text{K s}^3} \\ 4.2228 \frac{\text{kg m}^2}{\text{K s}^3} & 0.5404 \frac{\text{kg m}^2}{\text{K s}^3} & 0 \\ 0.6334 \frac{\text{kg m}^2}{\text{K s}^3} & 0.0608 \frac{\text{kg m}^2}{\text{K s}^3} & -1.2112 \frac{\text{kg m}^2}{\text{K s}^3} \end{pmatrix}$$

$$B := \begin{pmatrix} b_1 \\ b_2 \\ b_3 \end{pmatrix} = \begin{pmatrix} 1717.368 \frac{\text{kg m}^2}{\text{s}^3} \\ 1673.169 \frac{\text{kg m}^2}{\text{s}^3} \\ -154.1484 \frac{\text{m}^2 \text{kg}}{\text{s}^3} \end{pmatrix}$$

Defining a matrix X for the unknown variables, we can solve by multiplying the inverse of matrix A with matrix B.

Value of mass flowrate:

$$X := A^{-1} \cdot B \quad \begin{matrix} 0.5 \frac{\text{m}}{\text{s}} & 1.0 \frac{\text{m}}{\text{s}} & 1.5 \frac{\text{m}}{\text{s}} \end{matrix}$$

$$X = \begin{pmatrix} 76.3493 \\ 91.9801 \\ 55.2152 \end{pmatrix} \text{ } ^\circ\text{C} \quad \begin{matrix} T_a := X_1 = 76.3493 \text{ } ^\circ\text{C} & 75.316 \text{ } ^\circ\text{C} & 74.323 \text{ } ^\circ\text{C} \\ T_{\text{cuConv}} := X_2 = 91.9801 \text{ } ^\circ\text{C} & 100.055 \text{ } ^\circ\text{C} & 107.81 \text{ } ^\circ\text{C} \\ T_s := X_3 = 55.2152 \text{ } ^\circ\text{C} & 55.080 \text{ } ^\circ\text{C} & 54.95 \text{ } ^\circ\text{C} \end{matrix}$$

Now that we know the unknown temperatures, we can calculate the net heat transfer away from the copper as follows:

$$Q'_{\text{cu\_net}} := \begin{matrix} Q'_{\text{h\_cu}} & Q'_{\text{rad\_r}} & Q'_{\text{rad\_s}} \end{matrix} \begin{pmatrix} 0.5 \frac{\text{m}}{\text{s}} \\ 1.0 \frac{\text{m}}{\text{s}} \\ 1.5 \frac{\text{m}}{\text{s}} \end{pmatrix}$$

$$Q'_{\text{cu\_net}} := \left( \frac{T_{\text{cuConv}} - T_a}{R_{\text{h\_cu}}} \right) + \left( \frac{T_{\text{cu}} - T_{\text{CF1}}}{R_{\text{rad1}}} \right) + \left( \frac{T_{\text{cu}} - T_s}{R_{\text{rad2}}} \right) = \begin{matrix} 67.7501 \text{ W} & 103.68 \text{ W} & 138.2 \text{ W} \end{matrix}$$

Heat transfer rates for all flowrates indicate a dramatic improvement upon the static air condition. If these amounts of heat dissipation could be realized, and if all assumptions about critical temperatures manifested correctly in practice, the machine's nominal torque output could be dramatically increased.

## C.2 Revised Calculations

## Static air condition:

### Key dimensions:

Nominal radius:  $r := 120 \text{ mm}$

Total axial length:  $l := 100 \text{ mm}$

Area of top and bottom surfaces of copper:

$$A_{\text{cu}} := 0.00118 \cdot 21 \cdot 2 \cdot 1.3 \text{ m}^2 = 0.0644 \text{ m}^2$$

Side area of copper:

$$A_{\text{cuB}} := 15.7 \cdot 9 \cdot 21 \text{ mm}^2 = 0.003 \text{ m}^2$$

Mean surface area for all radial surfaces:

$$A_{\text{std}} := \pi \cdot 2 \cdot r \cdot l = 0.0754 \text{ m}^2$$

Surface areas of CF and AL for side

$$A_{\text{al}} := \pi \cdot (124.5^2 - 115.5^2) \text{ mm}^2 = 0.0068 \text{ m}^2$$

$$A_{\text{cfs}} := \pi \cdot (126^2 - 114^2) \text{ mm}^2 = 0.009 \text{ m}^2$$

### Predefined Temperatures:

$$T_{\text{CF1}} := 46.0 \text{ }^\circ\text{C} \quad T_{\text{ambient}} := 20 \text{ }^\circ\text{C}$$

We must first specify a copper temperature to calculate total heat transfer. Then, magnet CF temperature can be calculated. Copper temperature can be manually adjusted to determine the limit.

### Thermal Resistances:

Static air conduction:

$$R_{\text{gapStat}} := \frac{1 \text{ mm}}{k_{\text{air}} \cdot A_{\text{cu}}} = 0.597 \frac{\text{K}}{\text{W}}$$

CF layer on magnets:

$$R_{\text{CF1}} := \frac{0.5 \text{ mm}}{k_{\text{cf}} \cdot A_{\text{std}}} = 0.0133 \frac{\text{K}}{\text{W}}$$

CF frame behind magnets:

$$R_{\text{CF2}} := \frac{2 \text{ mm}}{k_{\text{cf}} \cdot A_{\text{std}}} = 0.0531 \frac{\text{K}}{\text{W}}$$

### Thermal conductivities:

$$k_{\text{mag}} := 7 \frac{\text{W}}{\text{m K}}$$

$$k_{\text{air}} := 0.026 \frac{\text{W}}{\text{m K}}$$

$$k_{\text{cf}} := 0.5 \frac{\text{W}}{\text{m K}}$$

$$k_{\text{al}} := 205 \frac{\text{W}}{\text{m K}}$$

$$k_{\text{cfP}} := 6 \frac{\text{W}}{\text{m K}}$$

### Epoxy resin emissivity:

$$\varepsilon_{\text{resin}} := 0.95$$

Magnet:

$$R_{\text{mag}} := \frac{5.5 \text{ mm}}{k_{\text{mag}} \cdot A_{\text{std}}} = 0.0104 \frac{\text{K}}{\text{W}}$$

In-plane resistance of frame:

$$R_{\text{CF2S}} := \frac{\ln\left(\frac{0.195}{0.1315}\right)}{2 \cdot \pi \cdot k_{\text{cfP}} \cdot 0.005 \text{ m}} = 2.0902 \frac{\text{K}}{\text{W}}$$



Air cavity between frame layers:

$$R_{\text{air2}} := \frac{30 \text{ mm}}{k_{\text{air}} \cdot A_{\text{std}}} = 15.3034 \frac{K}{W}$$

The outer and innermost frame components exposed to air are equated as carbon fibre layers twice the thickness of the other frame layers:

$$R_{\text{CF3}} := 2 \cdot R_{\text{CF2}} = 0.1061 \frac{K}{W}$$

Aluminium ring:

$$R_{\text{al}} := \frac{2.5 \text{ mm}}{k_{\text{al}} \cdot A_{\text{al}}} = 0.0018 \frac{K}{W}$$

Radiation:

$$R_{\text{rad1}} := \frac{1}{9.43 \cdot \varepsilon_{\text{resin}} \cdot A_{\text{std}}} \frac{m^2 K}{W} = 1.4805 \frac{K}{W}$$

$$R_{\text{rad2}} := \frac{1}{9.43 \cdot \varepsilon_{\text{resin}} \cdot A_{\text{al}}} \frac{m^2 K}{W} = 16.4498 \frac{K}{W}$$

For the static air condition we have enough information to consolidate all thermal resistances and solve for the critical temperature of the CF layer around the magnets in one step. We first determine the maximum heat transfer possible between the CF surface and ambient air.

Radial direction:

*Air cavity and in-plane:*

$$R_{\text{midEq}} := \frac{1}{\frac{1}{R_{\text{air2}}} + \frac{1}{R_{\text{CF2S}}}} = 1.839 \frac{K}{W}$$

Total from CF to ambient:

$$R_{\text{CF\_amb}} := R_{\text{midEq}} + R_{\text{CF1}} + R_{\text{CF2}} + R_{\text{mag}} + R_{\text{convOut}} = 3.021 \frac{K}{W}$$

$$Q'_{\text{CF\_amb}} := \frac{T_{\text{CF1}} - T_{\text{ambient}}}{R_{\text{CF\_amb}}} = 8.6064 W$$

Side air gap conduction:

$$R_{\text{gapS}} := \frac{1 \text{ mm}}{k_{\text{air}} \cdot A_{\text{al}}} = 5.6679 \frac{K}{W}$$

Side CF frame:

$$R_{\text{cfS}} := \frac{2.5 \text{ mm}}{k_{\text{cf}} \cdot A_{\text{cfs}}} = 0.5526 \frac{K}{W}$$

External convection: We assume a typical coefficient of convection for the air moving over the outer surface as the rotor turns.

$$R_{\text{convOut}} := \frac{1}{100 \frac{W}{m^2 K} \cdot A_{\text{cfs}}} = 1.1052 \frac{K}{W}$$

Revised.

With this information, we can calculate the corresponding copper temperature. First, we need to calculate the combined thermal resistance for conduction and radiation.

$$R_{\text{gapEq}} := \frac{1}{\frac{1}{R_{\text{gapStat}}} + \frac{1}{R_{\text{rad1}}}} = 0.4254 \frac{\text{K}}{\text{W}}$$

$$T_{\text{cu}} := T_{\text{CF1}} + Q'_{\text{CF\_amb}} \cdot R_{\text{gapEq}} = 49.6614 \text{ } ^\circ\text{C}$$

With this temperature, we can also calculate the heat dissipated through the side of the machine. Again, we start by calculating the equivalent resistance for this section.

*Radiation and air conduction:*

$$R_{\text{gapEqS}} := \frac{1}{\frac{1}{R_{\text{gapS}}} + \frac{1}{R_{\text{rad2}}}} = 4.2154 \frac{\text{K}}{\text{W}}$$

*Combined resistances:*

$$R_{\text{side}} := R_{\text{al}} + R_{\text{gapEqS}} + R_{\text{cfS}} + R_{\text{convOut}} = 5.8751 \frac{\text{K F}}{\text{s A}^2}$$

$$Q'_{\text{side}} := \frac{T_{\text{cu}} - T_{\text{ambient}}}{R_{\text{side}}} = 5.0487 \text{ W}$$

$$R_{\text{convSide}} := \frac{1}{80 \frac{\text{W}}{\text{m}^2 \text{K}} \cdot (A_{\text{cuB}} \cdot 1.5)} = 2.8084 \frac{\text{K}}{\text{W}}$$

$$Q'_{\text{side2}} := \frac{T_{\text{cu}} - T_{\text{ambient}}}{R_{\text{convSide}}} = 10.5617 \text{ W}$$

This gives us the total heat dissipation for the critical magnet temperature for the static air case:

$$Q'_{\text{CF\_amb}} + Q'_{\text{side}} + Q'_{\text{side2}} = 24.2168 \text{ W}$$

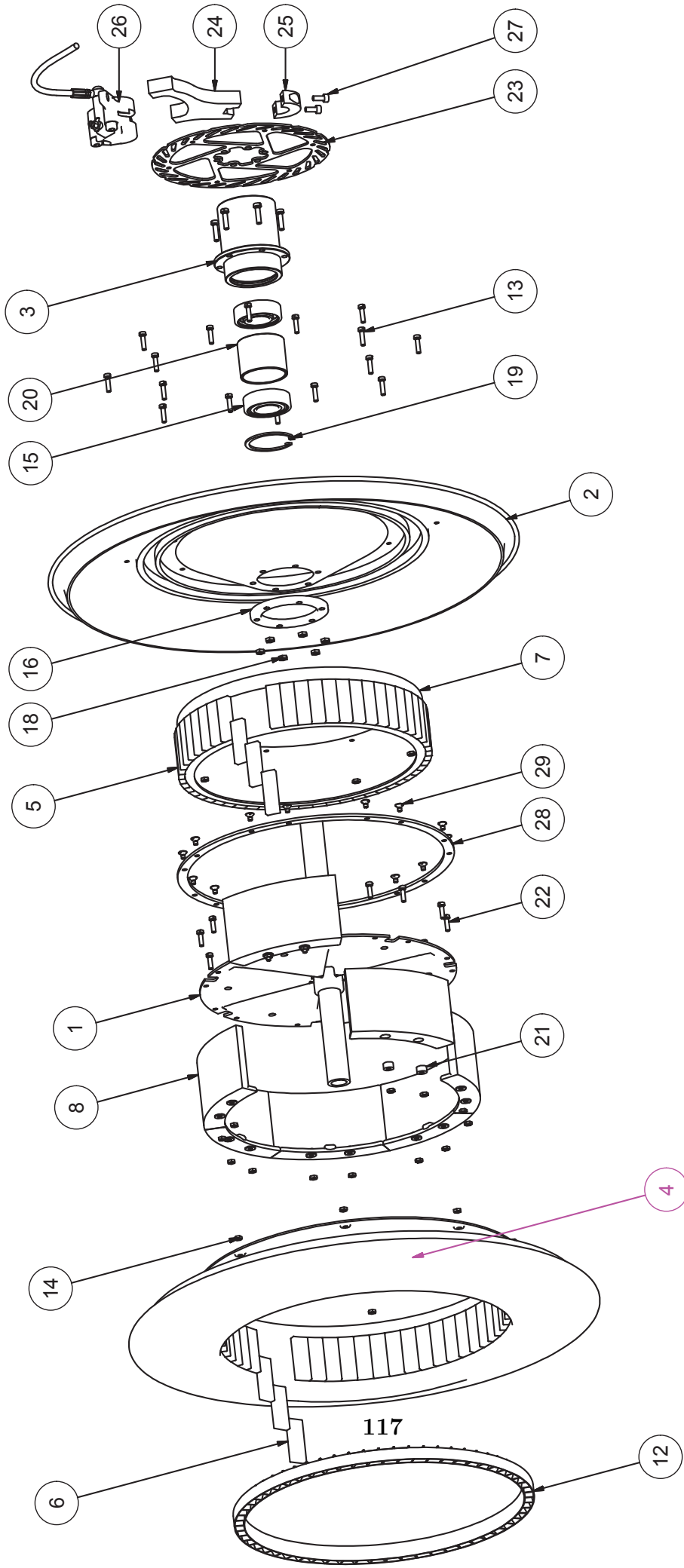
The total heat dissipation corresponds with the expected copper loss for a little more than 10A peak current, which would deliver 10.7 Nm of torque according to Maxwell simulations.

# Appendix D

## Assembly Drawing

ITEM	DESCRIPTION	QTY	MATERIAL - SPECIFICATIONS
1	Stator	1	CFRP
2	Primary Rotor Plate	1	CFRP
3	Rotor Hub	1	Aluminium
4	Secondary Rotor Plate	1	CFRP
5	Inner Magnet	56	NdFeB N48
6	Outer Magnet	56	NdFeB N48
7	Inner Magnet Rim	1	CFRP
8	Coil Set	7	0.2x70 Litz Wire; Aerontec AR600+AH2336 Epoxy Resin
12	Cooling Fan	1	PLA 3D printed plastic
13	Screw M4x12	16	Brass
14	Hexagon thin nut M4	30	Brass
15	Deep groove ball bearings	2	SKF E2 High Efficiency bearings
16	Rotor Hub Ring	1	Aluminium
17	Screws M5x20	6	Brass
18	Hexagon thin nuts	6	Brass
19	Circlip	1	Steel
20	Bearing Spacer	1	Aluminium
21	Coil Mount Stud	14	Aluminium
22	Screw M4x6	14	Brass
23	Brake Disc	1	Steel
24	Caliper Mount	1	Aluminium
25	Caliper Mount Lock	1	Aluminium
26	Brake Caliper	1	-
27	Hex. cap screw- M5	2	Brass
28	Coil Ring	1	Aluminium
29	Countersunk Screw	14	Brass

PRODUCED BY AN AUTODESK EDUCATIONAL PRODUCT



ITEM	BESKRYWING	AANTAL	MATERIAAL / SPESIFIKASIES
SKAAL OPA 3 0.27:1	TITEL: IDRFPM Carbon Fibre Prototype		
MATE IN ---			
DATUM 28/10/2015	VEL No.1	VAN 1	VELLE
			No.

**UNIVERSITEIT VAN STELLENBOSCH**

STUDENTE No. 15743373    TEKENAAR GI OOSTHUIZEN    NAGESIEN

6    5    4    3    2    1

PRODUCED BY AN AUTODESK EDUCATIONAL PRODUCT

PRODUCED BY AN AUTODESK EDUCATIONAL PRODUCT

# Bibliography

- [1] MarkForged 3D Printers, 2015.
- [2] R. Al Zaher, S. de Groot, H. Polinder, and P. Wieringa. Comparison of an axial flux and a radial flux permanent magnet motor for solar race cars. *International Conference on Electrical Machines - ICEM 2010*, pages 1–6, September 2010.
- [3] M. Aydin and T.a. Lipo. Performance comparison of dual-rotor radial-flux and axial-flux permanent-magnet BLDC machines. In *IEEE International Electric Machines and Drives Conference, 2003. IEMDC'03.*, volume 3, pages 1948–1954. IEEE, 2003.
- [4] NC Batista and R Melício. Self-start evaluation in lift-type vertical axis wind turbines: Methodology and computational tool applied to asymmetrical airfoils. . . ., *Energy and Electrical . . .*, (May), 2011.
- [5] Yunus A. Cengel and Afshin Jahanshahi Ghajar. *Heat and Mass Transfer (in SI Units)*. McGraw-Hill Education (Asia), 2014.
- [6] Felix Craz. Eco Shell Marathon Steering and Framework. 2014.
- [7] Stiaan Gerber. *A Finite Element Based Optimisation Tool for Electrical Machines*. Masters, Stellenbosch University, 2011.
- [8] K. Halbach. Design of permanent multipole magnets with oriented rare earth cobalt material. *Nuclear Instruments and Methods*, 169(1):1–10, February 1980.
- [9] Mike J. Hinton, A. S. Kaddour, and P. D. Soden. *Failure Criteria in Fibre Reinforced Polymer Composites: The World-Wide Failure Exercise*. Elsevier, 2004.
- [10] K Hwang, O Winter, Student Member, and I Suh. Performance Improvement of a 4WD Micro Electric Vehicle with In-Wheel Application of Ironless Permanent Magnet Synchronous Motors. pages 1846–1850, 2015.

- [11] M Islam, DSK Ting, and A Fartaj. Aerodynamic models for Darrieus-type straight-bladed vertical axis wind turbines. *Renewable and Sustainable Energy Reviews*, 12(4):1087–1109, May 2008.
- [12] A Joss and P J Randewijk. Design and Optimization of an Ironless Double-Rotor Radial Flux Permanent Magnet Machine. *South African Universities Power Engineering Conference - SAUPEC 2016*, 2016.
- [13] T.A. Lipo and M Aydin. Field weakening of permanent magnet machines: Design approaches. *EPE Power Electronics and Motion Control . . .*, 2004.
- [14] Gilbert M. Masters. *Renewable and Efficient Electric Power Systems*. John Wiley & Sons, Inc., Hoboken, NJ, USA, July 2004.
- [15] Anthony F. Mills. *Heat Transfer*. CRC Press, 1992.
- [16] G.I. Oosthuizen and P.J. Randewijk. Double-rotor ironless radial flux permanent magnet machine. *International Conference on Electrical Machines - ICEM 2014*, pages 496–501, September 2014.
- [17] P. J. Randewijk and M. J. Kamper. Analytical analysis of a Radial Flux Air-cored Permanent Magnet machine with a double-sided rotor and non-overlapping double-layer windings. *International Conference on Electrical Machines - ICEM 2012*, pages 1178–1184, September 2012.
- [18] Peter-Jan Randewijk. Analysis of a radial flux-air-cored permanent magnet machine with a double-sided rotor and non overlapping windings, March 2012.
- [19] P.J. Randewijk, M.J. Kamper, and R-J. Wang. Analysis and Performance Evaluation of Radial Flux Air-Cored Permanent Magnet Machines with Concentrated Coils. In *2007 7th International Conference on Power Electronics and Drive Systems*, pages 189–195. IEEE, November 2007.
- [20] C.I. Ras. The drivetrain specifications and driver interface for an electrical prototype car entry into the Shell Eco Marathon. 2014.
- [21] Francois Gerhardus Rossouw. Analysis and Design of Axial Flux Permanent Magnet Wind Generator System for Direct Battery Charging Applications by. (March), 2009.

- [22] J.J. Santin, C.H. Onder, J. Bernard, D. Isler, P. Kobler, F. Kolb, N. Weidmann, and L. Guzzella. *The World's Most Fuel Efficient Vehicle: Design and Development of Pac Car II*. vdf Hochschulverlag AG, Zurich, 2007.
- [23] S.T. Scowby, R.T. Dobson, and M.J. Kamper. Thermal modelling of an axial flux permanent magnet machine. *Applied Thermal Engineering*, 24(2-3):193–207, February 2004.
- [24] Johannes Abraham Stegmann. *Design and Analysis Aspects of Radial Flux Air-cored Permanent Magnet Wind Generator System for Direct Battery Charging Applications* by. PhD thesis, 2010.
- [25] Johannes Abraham Stegmann and Maarten J Kamper. Design Aspects of Double-Sided Rotor Radial Flux Air-Cored Permanent-Magnet Wind Generator. *IEEE Transactions on Industry Applications*, 47(2):767–778, March 2011.
- [26] Petrus Johannes Jacobus van Wyk. *Design and Evaluation of Medium Speed Geared Direct Grid-Connected Wind Generator Drive Train with Specific Focus on Slip Permanent Magnet Coupling*. Masters, Stellenbosch University, 2015.
- [27] Theodore Wildi. *Electrical Machines, Drives, and Power*. Pearson Education Inc., New Jersey, 5th edition, 2002.
- [28] Oliver Winter, Christian Kral, and Erich Schmidt. Design and loss assessment of air cored axial flux permanent magnet machines. *Electric Machines & Drives . . .*, pages 602–606, 2013.
- [29] Oliver Winter, Stephan Ucsnik, Michael Rudolph, Christian Kral, and Erich Schmidt. Ironless in-wheel hub motor design by using multi-domain finite element analyses. *International Symposium on Power Electronics Power Electronics, Electrical Drives, Automation and Motion*, pages 1474–1478, June 2012.
- [30] Bin Zhang, Ronghai Qu, Senior Member, Xinggong Fan, and Jin Wang. Thermal and Mechanical Optimization of Water Jacket of Permanent Magnet Synchronous Machines for EV Application Electromagnetic force. In *IEEE International Electric Machines and Drives Conference, 2015. IEMDC'15.*, pages 1329–1335, 2015.



- [31] Z.Q. Zhu and D. Howe. Halbach permanent magnet machines and applications: a review. *IEE Proceedings - Electric Power Applications*, 148(4):299, 2001.